Investigations on Multiscale Fractal-textured Superhydrophobic and Solar Selective Coatings

Rahul Jain

Thesis submitted to the faculty of the Virginia Polytechnic Institute and State University in partial fulfillment of the requirements for the degree of

Master of Science
In
Mechanical Engineering

Ranga Pitchumani, Chair
Jiangtao Cheng
Jonathan Boreyko

July 20, 2017
Blacksburg, Virginia

Keywords: Superhydrophobic coatings, Fractal model, Contact angle prediction, Multiscale surfaces, Anti-corrosion, Fractal coating, Copper electrodeposition coating, Coating durability tests, Solar selective coating, Zinc electrodeposition coating

Investigations on Multiscale Fractal-textured Superhydrophobic and Solar Selective Coatings

Rahul Jain

ABSTRACT

Functional coatings produced using scalable and cost-effective processes such as electrodeposition and etching lead to the creation of random roughness at multiple length scales on the surface. The first part of thesis work aims at developing a fundamental mathematical understanding of multiscale coatings by presenting a fractal model to describe wettability on such surfaces. These surfaces are described with a fractal asperity model based on the Weierstrass-Mandelbrot function. Using this description, a model is presented to evaluate the apparent contact angle in different wetting regimes. Experimental validation of the model predictions is presented on various hydrophobic and superhydrophobic surfaces generated on several materials under different processing conditions.

Superhydrophobic surfaces have myriad industrial applications, yet their practical utilization has been severely limited by their poor mechanical durability and longevity. Toward addressing this gap, the second and third parts of this thesis work present low cost, facile processes to fabricate superhydrophobic copper and zinc-based coatings via electrodeposition. Additionally, systematic studies are presented on coatings fabricated under different processing conditions to demonstrate excellent durability, mechanical and underwater stability, and corrosion resistance. The presented processes can be scaled to larger, durable coatings with controllable wettability for diverse applications.

Apart from their use as superhydrophobic surfaces, the application of multiscale coatings in photo-thermal conversion systems as solar selective coatings is explored in the final part of this thesis. The effects of scale-independent fractal parameters of the coating surfaces and heat treatment are systematically explored with respect to their optical properties of absorptance, emittance, and figure of merit (FOM).

Investigations on Multiscale Fractal-textured Superhydrophobic and Solar Selective Coatings

Rahul Jain

GENERAL AUDIENCE ABSTRACT

Coatings are extensively used through various industries and serve a range of purposes such as providing protection, changing the physical and chemical properties, decoration, and adding other new properties to the base surface. Coatings produced using scalable and cost-effective processes such as electrodeposition and etching are inherently rough and have features ranging from micro- to nano-scale, leading to their multiscale nature. The first part of thesis work aims at developing a fundamental mathematical understanding of these rough coatings by presenting a model to describe and predict the wettability on such surfaces. Wettability of a surface is its ability to maintain contact with a liquid, resulting from intermolecular interactions when the two are brought together. Wettability for a solid surface is generally quantified by the contact angle, measured through the liquid, where a liquid-vapor interface meets the solid surface. A mathematical model is presented to evaluate the apparent contact angle on such multiscale rough surfaces. Experimental validation of the model predictions is presented on various hydrophobic and superhydrophobic surfaces generated on several materials under different processing conditions.

Superhydrophobic surfaces do not get wet by water and water droplet contact angle on these surfaces exceed 150°. Such surfaces have extensive industrial applications, yet their practical utilization has been severely limited by their poor mechanical durability and longevity. Toward addressing this gap, the second and third parts of this thesis work present low cost, facile processes to fabricate superhydrophobic copper and zinc-based coatings via electrodeposition. Additionally, systematic studies are presented on coatings fabricated under different processing conditions to demonstrate excellent durability, mechanical and underwater stability, and corrosion resistance. The presented processes can be scaled to larger, durable coatings with controllable wettability for diverse applications.

Apart from their use as superhydrophobic surfaces, the application of multiscale coatings in photo-thermal conversion systems as solar selective coatings is explored in the final part of this

thesis. Solar selective coatings aim to improve photo-thermal conversion efficiency by providing a high solar absorptance and low thermal emittance. Solar selective coatings ensure that maximum incoming solar radiation is absorbed into the surface and radiative losses due to emissions at high temperatures are minimized. The effects of scale-independent mathematical parameters of the coating surfaces and heat treatment are systematically explored with respect to their optical properties of absorptance, emittance, and figure of merit (FOM).

Table of Contents

Chapter 1. Introduction 11
Chapter 2. Experimental Methods 5
2.1 Materials 5
2.2 Fabrication techniques 5
2.3 Fabrication of copper-based superhydrophobic and solar selective coatings 5
2.4 Fabrication of zinc-based superhydrophobic surfaces 6
2.5 Fabrication of aluminum-based hydrophobic surfaces 7
2.6 Morphology and wetting characterization 7
2.7 Surface profile measurement and power spectrum 8
2.8 Corrosion characterization 8
2.9 Durability characterization 9
2.10 Optical characterization 9
Chapter 3. Fractal Model for Wettability of Rough Surfaces 11
3.1. Introduction 11
3.2. Mathematical Description 14
3.3. Results and Discussion 21
3.3.1 SEM Morphology 21
3.3.2 Wetting and Fractal Properties 23
3.3.3 Model Validation 24
3.3.4 Effect of fractal dimension and asperity length scale 29
3.4. Conclusions 30
Chapter 4. Facile Fabrication of Durable Copper Based Superhydrophobic Surfaces via Electrodeposition 32
4.1. Introduction 32
4.2. Results and Discussion 35
4.2.1 SEM morphology and wetting characterization 35
4.2.2 Elemental analysis of the superhydrophobic samples 40
4.2.3 Self-cleaning property 41
4.2.4 Anti-corrosion property of the superhydrophobic surfaces 40
4.2.5 Mechanical durability of the superhydrophobic surfaces 42
4.2.6 Durability of Superhydrophobic surfaces under air exposure, water immersion and flow conditions 45

4.2.7 Rejuvenation of slippery superhydrophobic nature 42
4.3. Conclusions 49
Chapter 5. Fabrication and Characterization of Durable Zinc Based Superhydrophobic Coatings 51
5.1. Introduction 51
5.2. Results and Discussion 53
5.2.1. SEM morphology and wetting characterization 53
5.2.2. Elemental analysis of superhydrophobic samples 57
5.2.3 Anti-corrosion property of superhydrophobic surfaces 58
5.2.4 Mechanical durability of the superhydrophobic surfaces 60
5.2.5 Durability of superhydrophobic surfaces under air exposure, water immersion and flow conditions 63
5.3. Conclusions 66
Chapter 6. Fabrication and Fractal Description of Multiscale Copper Based Solar Selective Coatings 67
6.1. Introduction 67
6.2. Results and Discussion 70
6.2.1 Optical characterization 70
6.2.2 Effects of heat treatment 74
6.3. Conclusions 75
Chapter 7. Conclusion and Future Works 76
Bibliography 79

List of Figures

Figure 1. Schematic illustration of various wetting regimes: (a) Flat substrate; (b) Wenzel state where water droplet fills the roughness/grooves on the surface; and (c) Cassie-Baxter state where air is trapped within asperities. 12

Figure 2. Fast Fourier transform based power spectrum of an as-prepared copper based superhydrophobic surface, showing the fractal characteristics of the surface over a frequency range. 15

Figure 3. Schematic representation of multiscale, rough, self-affine superhydrophobic surface based on the fractal description with water droplet on top in Cassie state; θ represents the Cassie contact angle, and actual asperity dimensions are much smaller than the droplet size. 18

Figure 4. SEM images of coated surfaces at different magnifications showing the presence of asperities at multiple scales for: (a) Copper-based superhydrophobic surfaces (top row); (b) Zinc-based superhydrophobic surfaces (middle row); and (c) Aluminum-based hydrophobic surfaces (bottom row). 22

Figure 5. Variation of fractal dimension and length scale range for the prepared surfaces with the processing conditions: (a) Copper deposition at different potentials; (b) Zn/ZnO deposition at different potentials; (c) Zn/ZnO deposition at different deposition times; and (d) Aluminum-based surfaces for different etching times. 23

Figure 6. Measured Young's contact angles on flat base substrates with low surface energy treatment: (a) Copper, (b) Zinc and (c) Aluminum. 26

Figure 7. Validation of fractal model with experimental data on as-prepared hydrophobic and superhydrophobic copper based surfaces at different deposition potentials in Cassie state. 26

Figure 8. Validation of fractal model with experimental data on as-prepared superhydrophobic zinc based surfaces in Cassie state at: (a) different deposition times and (b) different deposition potentials. 27

Figure 9. Validation of fractal model with experimental data on as-prepared hydrophobic aluminum-based surfaces in Cassie state at different etching times. 28

Figure 10. Effects of fractal surface parameters on the apparent contact angle (θ) of the surface with Young's contact angle, θ_0, of 115°. 29

Figure 11. SEM morphologies and water contact angles of electrodeposited copper samples fabricated at overpotentials of (a) 0.5 V, (b) 0.7 V, (c) 0.9 V, and (d) 1.1 V, showing growth of globular shaped asperities beyond overpotential of 0.7 V; Respective representative water droplet and contact angle are displayed in the insets. 36

Figure 12. Strong superhydrophobic nature of the prepared surfaces: (a) successive snapshots of a water droplet dropped on a superhydrophobic sample; time interval between successive snapshots is 0.067 s; and (b) impinging water stream at an angle being reflected by the superhydrophobic samples..... 37

Figure 13. Dynamic contact angles with representative water droplet shapes on copper based superhydrophobic surface: (a) advancing contact angle and (b) receding contact angle. 38

Figure 14. EDS spectra for (a) unmodified deposited copper sample and (b) superhydrophobic copper sample. 39

Figure 15. Self-cleaning property of superhydrophobic copper surface (sample to the left in each frame) in comparison to bare copper substrate (sample to the right in each frame) based upon cleaning with water droplets of 10µl each: (a) initial accumulation of SiC particles on both samples and after cleaning with (b) 2 water droplets; (c) 5 water droplets; (d) 10 water droplets; (e) 30 water droplets; and (f) 55 water droplets. 40

Figure 16. Potentiodynamic polarization curves for superhydrophobic and base copper in 3.5 wt% NaCl solution. 41

Figure 17. (a) Schematic of the shear abrasion test setup and (b) variation of the contact angle and contact angle hysteresis for superhydrophobic copper surface with relative frictional energy per unit area, in comparison to several recently reported superhydrophobic coatings on different metallic substrates. 43

Figure 18. Variation of contact angle and contact angle hysteresis with impact energy per impact area for copper based superhydrophobic surfaces subject to falling sand abrasion test. Inset figure shows a schematic of the falling sand abrasion test setup. 45

Figure 19. Contact angle and contact angle hysteresis for superhydrophobic copper surfaces immersed in (a) static deionized water and (b) simulated deionized water flow equivalent to 11 kmph. The inset in (a) is the SEM micrograph of the surface after 60 days of static immersion, confirming the durability of the coating morphology. 47

Figure 20. Equivalent droplet shape and contact angle for (a) superhydrophobic copper surface after immersion in flowing water for 60 days, and (b) after coating rejuvenation in stearic acid solution..... 48

Figure 21. SEM Morphologies and water contact angles for the zinc based samples deposited at 1.3 V vs Ag/AgCl reference electrode for (a) 100 s, (b) 300 s, (c) 500 s, (d) 700 s, (e) 900 s, (f) 1100 s; Branch and needle-shaped asperities at multiple scales; Respective representative water droplet and contact angles are displayed in the insets. 54

Figure 22. SEM Morphologies and water contact angles for the zinc based samples prepared at potentials of (a) 1.1 V, (b) 1.2 V, (c) 1.4 V, and (d) 1.5 V against Ag/AgCl reference electrode;

Branched and needle-shaped asperities at multiple scales; Respective representative water droplet and contact angles are displayed in the insets. 56

Figure 23. Dynamic contact angles with representative water droplet shapes on zinc based superhydrophobic surface: (a) Advancing contact angle (θ_a) and (b) Receding contact angle (θ_r) 56

Figure 24. Successive snapshots of a water droplet dropped on a superhydrophobic sample with arrows indicating the direction of its instantaneous movement; time gap between each snapshot is 0.067 s. 57

Figure 25. EDS spectra for (a) unmodified deposited zinc sample, (b) stearic acid modified superhydrophobic zinc sample. 58

Figure 26. Potentiodynamic polarization curves for superhydrophobic and base zinc samples in 3.5 wt% NaCl solution. 59

Figure 27. (a) Schematic of shear abrasion test setup and (b) variation of the contact angle and contact angle hysteresis for superhydrophobic zinc surface with relative frictional energy per unit area, in comparison to several recently reported superhydrophobic coatings on different metallic substrates. 61

Figure 28. Variation of contact angle and contact angle hysteresis with impact energy per impact area for zinc based superhydrophobic surfaces subject to falling sand abrasion test. Inset figure shows a schematic of the falling sand abrasion test setup. 63

Figure 29. Contact angle and contact angle hysteresis for zinc based superhydrophobic surfaces immersed in (a) static deionized water and (b) simulated deionized water flow equivalent to 11 kmph. 65

Figure 30. Reflectance spectra of copper samples deposited at 1.1 V and heat treated in comparison with bare copper substrate 70

Figure 31. Variation of effective solar absorptivity for copper based deposited and heat treated samples at various deposition overpotentials ranging from 0.3 V to 1.1 V, showing the significant increase of solar absorptivity of coatings deposited at high overpotentials. 72

Figure 32. Thermal emissivity at 80^{o} C for copper based deposited and heat treated samples at various deposition overpotentials ranging from 0.3 V to 1.1 V. 72

Figure 33. Figure of merit (FOM) for copper based deposited and heat treated samples at various deposition overpotentials ranging from 0.3 V to 1.1 V 73

List of Tables

Table 1. Corrosion parameters for base copper and superhydrophobic copper in 3.5 wt% NaCl solution..... 41

Table 2. Corrosion parameters for base zinc and superhydrophobic zinc in 3.5 wt% NaCl solution 59

Chapter 1: Introduction

Coatings have myriad industrial applications and are generated by use of various processes such as chemical vapor deposition, solution-immersion, spray coating, magnetron sputtering, etching, and electrodeposition. The purposes of applying surface coatings are generally decorative, functional, or both. Decorative coatings improve the aesthetic appearance of base surface and provide a protection layer. However, functional coatings are generally aimed at the modification of physical and chemical properties of the base surface, such as, wettability, solar absorptivity, thermal emissivity, corrosion resistance, chemical resistance, strength or wear resistance. Coating materials and morphology are the primary factors that affect the coating properties and functions, which are controlled by deposition processes and parameters. Development of robust and durable superhydrophobic and solar selective coatings have been a major area of research in recent past.[1-4] Fabrication of these coatings by using cost-effective and scalable electrodeposition processes is considered as a part of this thesis work.

Superhydrophobic surfaces exhibit high water contact angles, greater than 150^{o}, and small contact angle hysteresis of less than 10^{o}.[1,5] Through studies based on naturally occurring superhydrophobic surfaces, researchers have observed that hierarchical or multiscale morphology, such as a combination of micro- and nano-structures, together with the low energy of the surface, leads to the superhydrophobic nature of a surface.[6,7] In general, two types of wetting states are observed on such surfaces namely, Wenzel state[8] and Cassie state[9]. In the Wenzel state, a water droplet fills the roughness grooves present on the surface, leading to the pinning of droplet to the surface and does not allow the surface to self-clean. On the other hand, in Cassie state the droplet does not penetrate into the surface due to the entrapment of air within the surface roughness and cavities, leading to high contact angles and very low sliding angles.[7,10]

Although extensive developments have been made in the superhydrophobic coatings fabrication processes on various materials, mathematical understanding of wettability on such engineered surfaces remain limited in scope, being mostly confined to ordered surfaces, in literature. Mathematical analysis of wettability on periodically arranged posts/ridges based geometries prepared by processes such as laser etching, plasma etching, physical and chemical vapor deposition etc. has been performed extensively by many researchers[11-15], due to the simplicity of estimating roughness and fraction of solid region in contact with water droplet for such regular arrangement of posts. However, industrial scalability of these surface geometries is

rather limited, due to the associated manufacturing time and costs. Large scale generation of superhydrophobic surfaces is more practical with randomly rough surface structures prepared through processes such as electrodeposition, spray coating, etching, etc. However, the studies so far on predicting contact angles on such randomly rough surfaces have mostly been correlatory in nature, are based on scale-dependent roughness parameters, and are limited in experimental validation to specific materials and conditions. To overcome these limitations, the first part of present thesis work presents a scale-independent self-affine fractal representation of multiscale asperity features based on the Weierstrass-Mandelbrot (W-M) function and size distribution.[16] A theoretical model is presented to predict the wettability of any multiscale rough hydrophobic and superhydrophobic surface based on its fractal parameters, which are uniquely determined by surface profile scan. Moreover, a comprehensive study of the effects of both fractal dimension and range of length scales of roughness asperity structures is presented and discussed.

Moreover, superhydrophobic surfaces are known for their vast range of applications and properties such as self-cleaning[17,18], drag reduction[19,20], improved phase change heat transfer[21,22], anti-icing[23,7], anti-corrosion[7,24]. Although significant developments have been made in the processes and materials to fabricate superhydrophobic surfaces, very few of them have shown their viability in industrial applications. This is due to their poor mechanical strength, abrasion resistance, transition from slippery Cassie to sticky Wenzel state, and durability of the superhydrophobicity and plastron layer under water immersion. Mechanical strength and durability of superhydrophobic coatings are, therefore, of considerable focus in recent studies. Many researchers have employed sandpaper based shear abrasion test to evaluate the mechanical durability of the superhydrophobic surfaces.[25-29] However, only a few have reported satisfactory mechanical durability. Furthermore, various studies have reported a steady loss in superhydrophobic nature of coatings with immersion time in water.[30,31] Though practical applications of superhydrophobic surfaces would require them to be in contact with steady as well as flowing water for significantly longer durations, studies are rather limited in performing extensive durability studies in such environments.

Among the superhydrophobic coatings on metallic substrates, copper and zinc have attracted significant interest. Copper has wide industrial applicability and is used in heat exchangers, pipelines, and electrical appliances due to its good thermal and electrical conductivity in addition to mechanical stability. Moreover, Zinc has its primary application in galvanization

industry to protect the steel structures from corrosion[32] and industrial application of zinc coating generally requires an additional hexavalent chrome coating for strength, decoration and to further prevent the corrosion. However, chrome electroplating and anodizing is one of the largest source of carcinogenic chromium emissions in the country and environmental protection agency (EPA) regulations have aimed at eliminating the use of hexavalent chromium in electrodeposition.[33] It has been reported by several researchers that the application of superhydrophobic coating enhances the anti-corrosion properties of a particular substrate and improves multiphase heat transfer.[34] Hence, application of robust and durable superhydrophobic coating may improve the corrosion resistance and provide non-wettable properties to copper and zinc substrates. Although significant developments have been made in the processes and materials to fabricate superhydrophobic surfaces on both copper and zinc substrates, however, industrial scalability of some of the reported techniques is rather limited. Due to low cost, uniform deposition irrespective of size and shape, and industrial scalability, electrodeposition is considered as one of the most effective technique for large scale generation of superhydrophobic surfaces.

The second and third parts of the thesis present facile and cost-effective processes based on electrodeposition to fabricate superhydrophobic copper and zinc coatings integral on copper and zinc substrates, and report extensive characterizations of the coatings. Comprehensive studies of the effects of applied deposition potential and deposition duration on the morphology and wettability is also presented and discussed. Furthermore, systematic studies are described to evaluate the chemical composition, growth mechanism, mechanical abrasion stability, corrosion resistance, self-cleaning effect, air-exposure durability, durability under steady water, and durability under flowing water conditions of the optimal superhydrophobic surfaces.

Improving the photothermal conversion efficiency of concentrating solar power (CSP) systems is of considerable focus in recent studies.[2-4] To achieve the desired optical properties of the surface carrying the heat transfer fluid, solar selective coatings are applied on the base metal substrates. Last part of thesis extends the development of electrodeposition based multiscale coatings into the development of solar selective coatings and their extensive mathematical characterization. Correlating fractal parameters of prepared coatings with their optical properties, this study provides a proof of concept that highly fractal, multiscale coatings fabricated via electrodeposition can significantly improve the light trapping within the coatings, leading to improved solar absorptivity and figure of merit.

The thesis is organized as follows: second chapter describes the various processes used to generate superhydrophobic and solar selective surfaces. Additionally, various characterization techniques used to estimate wettability, corrosion resistance, durability, and power spectrum of prepared surfaces are also described. Subsequently, third chapter describes the developed fractal model to estimate wettability on multiscale rough surfaces and model validation on various hydrophobic and superhydrophobic surfaces. Next two chapters discuss the generation of superhydrophobic surfaces on copper and zinc substrates with extensive characterizations such as wettability, morphology, corrosion, self-cleaning, and durability. Sixth chapter details the development of copper based solar selective coatings and obtained optical characterization results on prepared coatings.

Chapter 2. Experimental Methods

Materials and processes to fabricate hydrophobic, superhydrophobic and solar selective coatings are described in this chapter. Additionally, various surface characterizations such as morphology, wetting, surface profile, corrosion, mechanical and underwater durability, and optical characterizations, as performed as a part of thesis work, are also described in detail.

2.1 Materials

Analytical grade copper sulfate ($CuSO_4$, 99+%), sulfuric acid (H_2SO_4), acetone (99.5+%), methanol (99.8+%), zinc-acetate-dihydrate ($Zn(CH_3COO)_2.2H_2O$, 98%), potassium chloride (KCl, 99+%) and stearic acid ($CH_3(CH_2)_{16}CO_2H$, 97%) were purchased from Fisher Scientific, USA and used as received without any further purification. Furthermore, zinc sheet (99%), copper sheet (99.9%), aluminum sheet (96-98%) were purchased from McMaster Carr, USA. To prepare all the electrolyte solutions deionized water with resistivity of 18MΩ.cm was utilized.

2.2 Fabrication techniques

Hydrophobic and superhydrophobic coatings considered in this work were fabricated using two different techniques: electrodeposition and etching. Both methods are suited for large-scale fabrication of coatings at low cost, with simplicity and high degree of uniformity. Electrodeposition was employed to prepare the hydrophobic and superhydrophobic coatings based on copper and zinc. Deposition was performed at various deposition potentials and deposition times to arrive at optimum deposition conditions to develop superhydrophobic surfaces on these materials. AUTOLAB PGSTAT128N potentiostat (ECO chemie, Utrecht, The Netherlands) with a traditional three electrode system was used to perform all the electrodeposition experiments. Aluminum based hydrophobic coatings were prepared using etching in a HCl based solution.

2.3 Fabrication of copper-based superhydrophobic and solar selective coatings

Superhydrophobic surfaces on copper substrates were fabricated using the two-step electrodeposition process as described by Haghdoost and Pitchumani[35] to generate stable electrodeposition coatings. In this process, copper sheet was used as a reference electrode and platinum sheet was used as an anode. The working electrode was also a copper sheet with an exposed area of $1cm^2$. All the electrodes were rigorously cleaned with acetone, methanol and deionized water to remove any dirt and grease from the surface, and dried in air. The electrolyte

was an aqueous solution containing $CuSO_4$ (1 M) and H_2SO_4 (0.5 M). The solution was bubbled with nitrogen for 15 min before the fabrication of each sample to remove air. As a reference electrode of the same copper sheet was considered in this study, overpotential can be used to indicate the applied potential. Furthermore, electrodeposition was performed at various overpotentials ranging from 0.3 V to 1.1 V, to study the effect of applied overpotential on the wetting property of the sample. It was identified by Haghdoost and Pitchumani[35] that application of a low overpotential for a short time after the application of a high overpotential leads to a stable coating. Accordingly, in the present study, electrodeposition at overpotentials above 0.9 V was followed by deposition at 0.15 V for a duration of 10 sec. After electrodeposition, surfaces were rinsed with acetone and deionized water, and dried with nitrogen gas. As-prepared multiscale inherent coatings at this step are utilized as solar selective coatings to study the effect of multiscale and fractal nature of coatings on their optical properties such as solar absorptivity, emissivity, and figure of merit.

As a final step, the as-prepared surfaces were modified with immersion in 0.02 M methanol solution of stearic acid at room temperature for 1 hour, to generate copper-based superhydrophobic coatings inherent on copper substrate. The modified samples were then washed with methanol to remove any residual organic acid on the surface, followed by washing with deionized water and then were dried for further characterization and study.

2.4 Fabrication of zinc-based superhydrophobic surfaces

Electrodeposition of superhydrophobic zinc coating on zinc substrate was carried out with zinc sheet as anode, Ag/AgCl as reference electrode and zinc sheet with an exposed area of $1cm^2$ as working electrode. All the electrodes were cleaned with acetone, methanol, and deionized water followed by drying in air. The electrolyte was an aqueous solution containing zinc acetate (0.025 M) and KCl (1.5 M). Electrodeposition was performed at several voltages ranging from 1.1 V to 1.5 V and at various deposition times, to study the effect of voltage and deposition time on the wettability and to validate the developed mathematical model for several process parameters. After electrodeposition, the samples were rinsed with deionized water and dried in air.

The as-prepared surfaces were modified with immersion in 0.01 M methanol solution of stearic acid at room temperature for 24 hours. The modified samples were then washed with methanol to

remove any residual organic acid on the surface, followed by washing with deionized water and drying prior to their characterization and study.

2.5 Fabrication of aluminum-based hydrophobic surfaces

Aluminum substrate (2.5 cm x 1.5 cm) was cleaned with acetone, methanol, and deionized water and dried in air. The dried aluminum sample was then etched with 1M HCl solution for etching times of 5 and 10 min. The etched samples were washed rigorously with deionized water to remove any residual acid off the sample and then dried again in air.

These samples were then modified with immersion in 0.01 M methanol solution of stearic acid at room temperature for 24 hours. The modified samples were then washed with methanol to remove any residual organic acid on the surface, followed by washing with deionized water and drying to prepare samples for further characterization and study.

2.6 Morphology and wetting characterization

The surface morphologies of the deposited coatings were examined using the FEI Quanta 600 scanning electron microscope (SEM), which was operated at 10KeV for electron imaging. Furthermore, wetting properties of the prepared coatings were estimated through their static water contact angle measurement. Contact angles of water droplet on the as-prepared coatings were measured using the FTA-32 contact angle measurement setup, which consists of water droplet dispensing system, high speed adjustable camera, lens, back light, and software for automated control of these equipment and to capture the droplet images. A deionized water drop of 10 µl was used to measure the static contact angles. The droplet was placed on the sample via the automated software-controlled droplet dispensing system. Images of this water droplet were captured using a high-speed camera and saved using the software associated with FTA-32 system. Additionally, dynamic contact angles were measured using the volume changing dynamic sessile drop method. Starting with a small water droplet volume on the surface, images of the droplet were continuously recorded as the volume of the droplet was gradually increased. The maximum contact angle obtained through this process is known as advancing contact angle (θ_a). In a similar way, volume of water droplet is gradually reduced and droplet shape images are captured and to arrive at the smallest contact angle, called the receding contact angle (θ_r). The difference between advancing and receding contact angles gives the contact angle hysteresis. Images obtained through the

described setup were processed through the ImageJ software[36,37] to estimate the contact angles. For each sample corresponding to the various deposition overpotential, three contact angle measurements were performed to evaluate the experimental uncertainty associated with the measured data.

2.7 Surface profile measurement and power spectrum

A Zygo NewView 800 series 3D optical surface profiler was used to perform profilometric measurements on the prepared superhydrophobic/hydrophobic samples. The instrument uses coherence scanning interferometry to measure the surface profile and provide non-contact, highly accurate and quick measurements of the prepared surfaces. Optical surface profile measurement resolution was based on the smallest asperity size, as observed in SEM morphology. The measured profile scan data was processed through the image and surface analysis software Gwyddion[38] for profile visualization and analysis. Surface profile scans were performed at three different locations for each sample. For each sample, corresponding to a particular combination of material and processing condition, profilometric scans were performed on three replicates and the fractal parameters are presented as average and standard deviation of the obtained data.

Surface profile data obtained through above procedure was analyzed using the software Gwyddion and MATLAB to obtain its averaged Fourier transform based power spectrum. In the present analysis, radially averaged power spectrum describing energy per unit interval of the surface was used to consider the effect of asperities throughout the surface and describe the roughness power spectral density. Averaged power spectrum was normalized with respect to the scan size as well, so that power spectrum of part scan is similar to the power spectrum of entire scan. Using the obtained power spectra for the individual surfaces, their corresponding fractal parameters were obtained as described in the next section on the mathematical description of the multiscale random surfaces.

2.8 Corrosion characterization

Corrosion characteristic of as-fabricated superhydrophobic coating was investigated in 3.5 wt% NaCl solution. The electrodeposition setup, described in Section 2.2, with Ag/AgCl (3M KCl) as reference electrode, Pt sheet as anode and the sample under study as the working electrode, was employed for the present analysis. Corrosion measurements were made based on potentiodynamic

polarization plots obtained by varying the applied potential at a rate of 1mV/s. The data obtained from the potential scans were used to estimate the Tafel-slope-based corrosion parameters such as corrosion potential, corrosion current and polarization resistance.

2.9 Durability characterization

Mechanical and under-water stability of the as-prepared superhydrophobic surfaces were estimated through various abrasion and immersion tests. To estimate the mechanical robustness of the coatings, sandpaper based shear abrasion and falling sand abrasion tests were employed. As a part of shear abrasion test, samples were dragged on a 1000 grit sandpaper at a speed of 10 mm/s, under a load of 3 kPa, and the changes in wetting properties with abrasion distance were measured. The falling sand abrasion test was based on a modification of the ASTM D968 standard[39], in which the durability of the coating, in terms of sustained superhydrophobic nature, was estimated after dropping a predetermined amount of silica grains from a height on the sample inclined at 45^{o}.[40,41]

Durability of the coatings was further characterized based upon long duration exposure to air, and submersion in steady and flowing water. Samples were immersed in deionized water for up to 60 days, and changes in wettability were measured after every 5–7 days. To estimate the stability of the coatings in sustained flow conditions, the samples were immersed in a beaker in which deionized water was spun continuously using a magnetic stirrer. Changes in wetting properties of the samples were evaluated under sustained stirring at 750 RPM corresponding to a speed of about 11 kmph, for a sample held at the edge of the beaker, for up to a period of 60 days.

2.10 Optical Characterization

Figure of merit of the prepared coatings was evaluated based on their solar absorptance (α_s), emittance at 2500 nm ($\varepsilon_{2500\ nm}$), and thermal emittance at 80°C (ε_{80^oC}) as described by Ambrosini, et al.[42] Diffuse reflectance for the fabricated samples was measured in the range of 0.3–2.5 µm using Cary 5000 UV-vis-NIR spectrophotometer. PTFE diffuse reflectance standard was employed for the calibration of the spectrophotometer. Reflectance data obtained through above measurement was used to estimate the solar absorptance of the samples corresponding to the AM 1.5 solar spectra employing the method as described by katumba, et al.[43,44] Thermal emittance from fabricated solar selective coatings at 80°C (ε_{80^oC}) was measured by correlating the surface temperatures as measured using a thermocouple and an IR thermometer, when the surface was at

a temperature of 80°C. Optical measurements were also performed at three different locations for each sample. Similar to profilometric measurements, for each sample corresponding to a particular combination of material and processing condition, optical measurements were also performed on three replicates and resulting optical properties such as solar absorptivity, thermal emissivity, and figure of merit are presented as average and standard deviation of the obtained data.

Chapter 3. Fractal Model for Wettability of Rough Surfaces

This chapter presents a fractal model to describe wettability on multiscale randomly rough surfaces. Hydrophobic or superhydrophobic surfaces produced using processes such as electrodeposition and etching lead to the creation of random roughness at multiple length scales on the surface. This chapter considers the description of such surfaces with a fractal asperity model based on the Weierstrass-Mandelbrot (W-M) function, where the fractal parameters are uniquely determined from a power spectrum of the surface. Using this description, a model is presented to evaluate the apparent contact angle in the different wetting regimes. The model is predictive in that it does not use any empirical or correlatory fitting of parameters to experimental data. Experimental validation of the model predictions is presented on various hydrophobic and superhydrophobic surfaces generated on several materials under different processing conditions. The contact angle is found be strongly dependent on the range of asperity length scale and weakly dependent of the fractal dimension for a surface with stable Cassie state. Based on the fractal description, desired surface roughness characteristics for generating superhydrophobicity on a particular substrate are also derived.

3.1. Introduction

Superhydrophobic surfaces exhibit water contact angles of more than 150°, a small roll off angle and contact angle hysteresis generally less than 10°.[1,5] Their vast range of applications and properties such as self-cleaning[17,18], drag reduction[19,20], improved phase change heat transfer[21,22], anti-icing[23,7] and anti-corrosion[7,24] have significantly attracted attention of academic and industrial researchers over the past decade.

One approach to creation of hydrophobic or superhydrophobic properties on a surface involves increasing surface roughness, and roughness-induced wetting has been a major focus area in the literature. In general, two types of wetting states are observed on such surfaces namely, Wenzel state[8] and Cassie state[9]. In Wenzel state, water droplet fills the roughness grooves present on the surface, which leads to pinning of the droplet to the surface. On the other hand, in Cassie state, the droplet does not penetrate into the surface due to the entrapment of air within the surface roughness, as shown in Figure 1, and leads to very low sliding angles.[7,10] Many naturally occurring surfaces such as lotus leaves[45] and water striders[46,47] are known to have a stable Cassie state characterized by superhydrophobicity and self-cleaning property[10]. Inspired by this lotus leaf

effect, researchers have investigated the required parameters to transform a surface into being superhydrophobic. It has been observed that roughness at two or more length scales, such as a combination of micro- and nano-structures, together with low surface energy of the surface, ensures a stable Cassie state and superhydrophobicity on a substrate.[6]

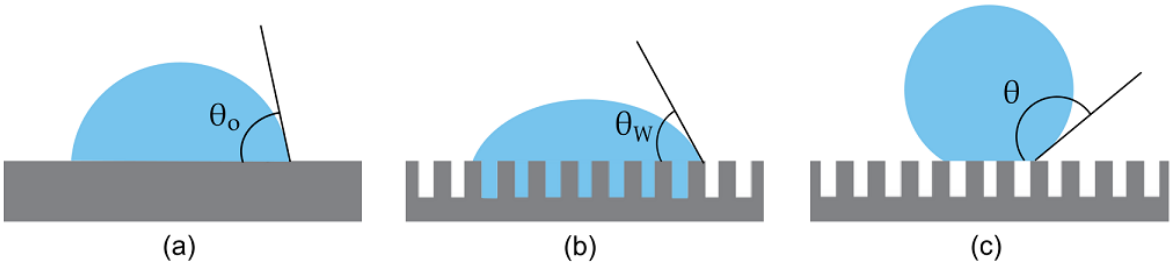

Figure 1. Schematic illustration of various wetting regimes: (a) Flat substrate; (b) Wenzel state where water droplet fills the roughness/grooves on the surface; and (c) Cassie-Baxter state where air is trapped within asperities.

Analysis of wettability on periodically arranged posts/ridges based geometries prepared by processes such as laser etching, plasma etching, physical and chemical vapor deposition etc. has been performed extensively by many researchers[11-15], due to the simplicity of estimating roughness and fraction of solid region in contact with water droplet for such regular arrangement of posts. However, industrial scalability of these surface geometries is rather limited, due to the associated manufacturing time and costs. Large scale generation of superhydrophobic surfaces is more practical with randomly rough surface structures prepared through processes such as electrodeposition, spray coating, etching, etc. Furthermore, it has been demonstrated that randomly rough surfaces may show contact angles of up to 179°.[48]

Statistical properties of multiscale random surfaces have been characterized by their power spectral density in several studies.[49-55] Based on studies on rough surfaces, it has been suggested that superhydrophobicity is related to the third moment of the power spectral density of the surface.[49,55-60] Li and Amirfazli[61] performed thermodynamic studies on 3D pillar based hierarchical superhydrophobic surfaces and suggested the importance of dual scale asperity structures to provide a stable superhydrophobic performance as well as mechanical durability. In other studies[62,63], they also developed a mathematical model to predict equilibrium contact angle and contact angle hysteresis on such hierarchical surfaces, based on 2D and 3D model surfaces with periodically arranged asperity structures. Additionally, criterion for wetting transition from

Cassie state to Wenzel state were also described. Gigli, et al.[64] developed a hierarchical dual-scale structures with micro- and nano-pillars via etching and showed the importance of such dual-scale structures in reducing wettability. Recently, Frankiewicz and Attinger[50] also proposed a model to estimate the contact angle and solid fraction of the prepared multiscale random surface by representing it by a generic model based on the superposition of square wave profiles with smaller asperities on top of larger base asperities. However, since real surfaces do not follow the assumed square wave profiles and arranged pillar based asperity structures, the determination of the square asperity dimensions and pitch is largely a matter of correlation of the experimental results to SEM images.

In all these studies, the surface topography is described by parameters such as root-mean-squared (RMS) height and slope. However, it was pointed out by Majumdar and Bhushan[51] that these parameters are not uniquely defined for a surface and depend on the scan length and resolution of the profile measuring instrument. This suggests the need for a scale-independent, fractal representation and, in turn, estimation of wettability based on those fractal parameters. Only a few researchers have considered the effect of the fractal parameters on wettability of a surface. Shibuichi, Onda et al.[52,53] developed a model to estimate the wetting on a fractal surface and validated it experimentally on waxy soft films. However, their model was not found to be consistent in the experimental study on the fractal surfaces made of silane coated core shell particles by Synytska, et al.[54] Palasantzas and De Hosson[55] theoretically studied the wetting of self-affine randomly rough surfaces; however, their study was limited in applicability to water droplets in the Wenzel state. Bottiglione, et al.[56,57] performed numerical analysis to predict the equilibrium contact angles of two dimensional drops on self-affine fractal profile in all the wetting regimes and showed that roughness over several scales improves the superhydrophobic nature of a surface. Yang, et al.[58] performed molecular dynamic simulations for liquid drops in contact with self-affine fractal surfaces and showed that contact angle for nano-droplets depends on the RMS surface roughness amplitude and is independent of the fractal dimension of the surface. Sarkar, et al.[59] performed experimental studies to understand the effect of fractal properties of a surface on wetting properties and showed that wetting in Wenzel state is influenced by the RMS height of the surface profile, in-plane roughness correlation length and roughness exponent.

It is evident from the foregoing discussion that the studies so far on predicting contact angles have mostly been correlatory in nature, are based on scale-dependent roughness parameters, and

are limited in experimental validation to specific materials and conditions. To overcome these limitations, the present work presents a scale-independent self-affine fractal representation of multiscale asperity features based on the Weierstrass-Mandelbrot (W-M) function and size distribution.[16] A theoretical model is presented to predict the wettability of any multiscale rough hydrophobic and superhydrophobic surface based on its fractal parameters, which are uniquely determined by surface profile scan. The model accounts for the effect of partial wetting and can predict the contact angles on a surface irrespective of its wetting regime. The predictive model is validated extensively for the experimentally generated hydrophobic/superhydrophobic surfaces. A good agreement is demonstrated between the experimentally measured equilibrium contact angle and the predicted contact angle on various materials such as copper, zinc, aluminum with surfaces fabricated by industrially scalable processes, electrodeposition and etching. A comprehensive study of the effects of both fractal dimension and range of length scales of roughness asperity structures is presented and discussed.

The article is organized as follows: first, a fractal description of surfaces and mathematical description of contact angles based on Cassie-Baxter and Wenzel model is presented. Subsequently, obtained results such as SEM images, wettability and fractal parameters of the fabricated coatings are discussed, followed by the discussions related to the experimental validation of the presented model.

3.2. Mathematical Description

Superhydrophobic surfaces are generated by creating hierarchical roughness features on the surfaces, followed by treatment with low surface energy materials. Through various techniques such as SEM imaging and profile scanning, it is observed that roughness asperity features range from the microscale to the nanoscale on such surfaces. Such multiscale surfaces are described using fractal mathematics in this study. An ideal fractal geometry is a complex pattern with repeating units at infinite scales. Such fractals geometries demonstrate same statistical characteristics as a whole geometry at every scale. Fractal description is used to describe and study naturally occurring objects such as coastlines, trees, and river networks etc. However, these naturally occurring objects demonstrate fractal nature only within particular length scale region. Additionally, base features scale by different amounts in different directions for naturally occurring fractals and are known as self-affine fractals. Fractal dimension of these surfaces provide

a statistical measure of complexity, quantifying how the details of a particular feature changes with the measurement scale. General Euclidean geometries have dimensions as a whole number, however, multiscale fractal geometries tend to have a non-integer as their fractal dimensions. Fractal dimensions also describe the space filling capacity of a particular pattern and inform how the multiscale fractal geometry scales differently from the space it is embedded in.

Power spectrums of fractal objects are generally employed to describe their fractal properties for naturally occurring fractals and has been considered to describe and study the coated multiscale surfaces. Power spectrum of a surface is a mathematical tool that decomposes the surface into contributions from different spatial frequencies. It provides a representation of the amplitude of a surface's roughness as a function of the spatial frequency of the roughness. Spatial frequency is the inverse of the wavelength of the roughness features. Power spectrum of a surface is estimated as a square of surface profile's Fourier spectrum.

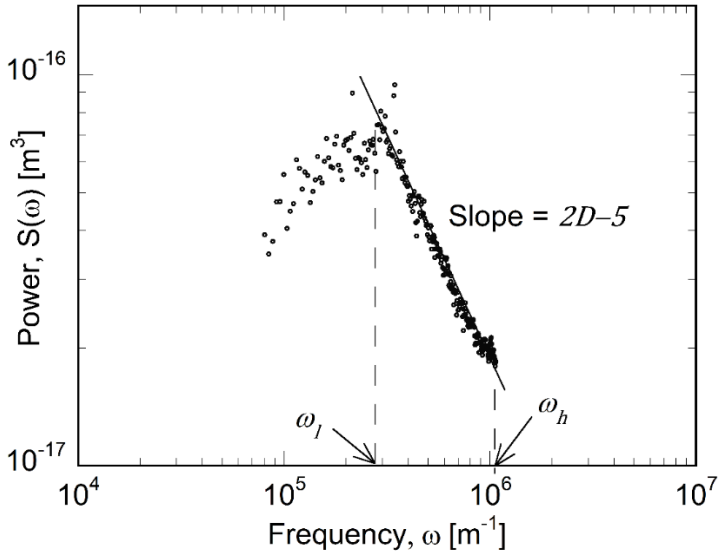

Figure 2. Fast Fourier transform based power spectrum of an as-prepared copper based superhydrophobic surface, showing the fractal characteristics of the surface over a frequency range.

An example power spectrum measured on one of the electrodeposited surfaces is shown in Figure 2. Here, x-axis represents the spatial frequency, which is inverse of asperity feature length scale and y-axis represents the power at specific spatial frequency, which is estimated as averaged squared Fourier transform of surface profile. The estimated power spectrum was based on the

optical profile measurements, as described in Section 2.7, with resolution corresponding to the smallest asperity element, observed in SEM morphology. The fabricated coatings display smallest asperities in micro-scale with frequency cut off in similar range. A more resolute measurement technique such as AFM is recommended for coatings with smallest asperities ranging to nano-scale. A power law variation of the power spectrum over the spatial frequency range $\omega_l < \omega < \omega_h$ is evident in Figure 2, which demonstrates the self-similar nature of the surface namely that upon appropriate magnification, a smaller portion of the surface profile will be statistically similar to a larger section of the profile. Such profiles can be appropriately described by fractal parameters.

The fractal description used here is based on the Weierstrass-Mandelbrot (W-M) function and size distribution[65], wherein a surface profile is expressed as a summation of an infinite series of sines and cosines with different amplitudes and frequencies, which correspond to the height and length of multiscale asperity features, respectively. The Weierstrass-Mandelbrot (W-M) function has been extensively used in analytical representation of multiscale featured surfaces in different applications.[16,65] As described by Yang and Pitchumani[65], the concept of a scale-independent slope is ill-defined for these non-differentiable surfaces, as progressively increasing roughness features are observed at progressively decreasing length scales; however, these surfaces can still be considered continuous as length scales are above atomic levels. The W-M function is a self-similar, non-differentiable and continuous function that captures all the inherent characteristics of fractal surfaces as described above. Electrodeposited and etched multiscale surfaces can, therefore, be described as:

$$z(x) = G^{D-1} \sum_{n=n_1}^{\infty} \frac{\cos(2\pi\gamma^n x)}{\gamma^{(2-D)n}} \qquad (1)$$

where, *D* is the fractal dimension, *G* is a mathematical scaling constant, γ^n is a frequency mode corresponding to the horizontal dimension, *L*, of roughness feature as γ^n = 1/*L*, and γ^{n_1} corresponds to the cut-off frequency, which relates to the maximum asperity length scale of the surface. Fractal dimension, D quantifies the complexity of surface as a ratio of change in feature detail to the change in magnification scale. Unlike conventional topological dimensions, fractal dimension may have non-integer values, indicating that a fractal set fills its space differently from an ordinary geometrical set. For instance, a surface with fractal dimension of 2.1 fills space similar to an ordinary surface. However, a fractal surface with a fractal dimension close to 3, fills space

nearly like a volume. The parameter γ determines the relative phase differences between the spectral modes. Since the phases in a real electrodeposited or etched surface are random, simulation of such surfaces requires that the phases of the frequency modes do no coincide with one other at any point and appear random. A value of $\gamma = 1.5$ represents such non-coincident random phase as well as high spectral density characteristics of the surfaces [16,66]. This value ensures that the powers of γ, which form the frequency spectrum, are not multiples of basic frequency, unlike a Fourier series, where the discrete frequencies increase in arithmetic progression and are multiples of a basic frequency, leading to a periodic appearance.[66]

Based on the Fourier transform[16,65], the power spectrum, $S(\omega)$, of the W-M function may be obtained as:

$$S(\omega) = \frac{G^{2(D-1)}}{2\ln\gamma}\frac{1}{\omega^{5-2D}} \tag{2}$$

where ω is the spatial frequency. The power law variation of power spectrum with frequency indicates the fractal nature of the surface. It can be seen from Figure 2 that the power law variation holds within a frequency range (ω_l, ω_h) that is characteristic for each surface, as also previously reported by Yang and Pitchumani[65] and Majumdar and Bhushan[16]. The high frequency (ω_h) limit of the range corresponds to the length of the smallest asperity (L_{min}) on the surface under study and the low frequency limit (ω_l) corresponds to the largest repeating unit or the largest asperity length scale (L_{max}) present on the surface, such that $L_{min} = \frac{1}{\omega_h}$, $and\ L_{max} = \frac{1}{\omega_l}$. The length scales ranging from L_{min} to L_{max} may be considered as one repeating unit representing the whole surface, with several asperities in between the above length scales.

In the present description, fractal parameters such as the fractal dimension, D, the scaling constant, G, and the length scale range can be estimated through analysis of a Fourier transform based power spectrum of a scan of the roughness profile on a surface. The slope of a log-log plot of the power spectrum in the characteristic frequency range can be compared to the slope $2D - 5$ of a log-log plot of the power spectrum of the W-M function as given by eq. (2) to estimate the fractal dimension, D. Similarly, the scaling constant, G, can be estimated by comparing the *y*-intercept on a log-log plot of the power spectrum of the surface to the *y*-intercept of a log-log plot of the power spectrum of the W-M function. Thus, the parameters of any random surface, D, G,

L_{max}, and L_{min}, required to represent the surface with a W-M function based fractal model are determined uniquely through surface measurements.

The multiscale asperities in this work are modeled as three-dimensional prismatic asperities of square cross section with varying heights and lengths, stacked as represented in Figure 3. The model considers that the smaller asperities are progressively stacked on top of larger base asperities. The topmost asperity element in such a representation is the asperity with minimum length and height, which are represented as L_{min} and $h(L_{min})$, respectively. Similarly, the base asperity element in such representation is the asperity with maximum length and height, denoted as L_{max} and $h(L_{max})$, respectively. In addition, Figure 3 also illustrates a representative water droplet in Cassie state placed on the asperity structure. In the Cassie state, the water droplet is in contact with only topmost or the smallest level of asperities and air is trapped in the cavities between the asperities, which leads to superhydrophobic nature of such surfaces.

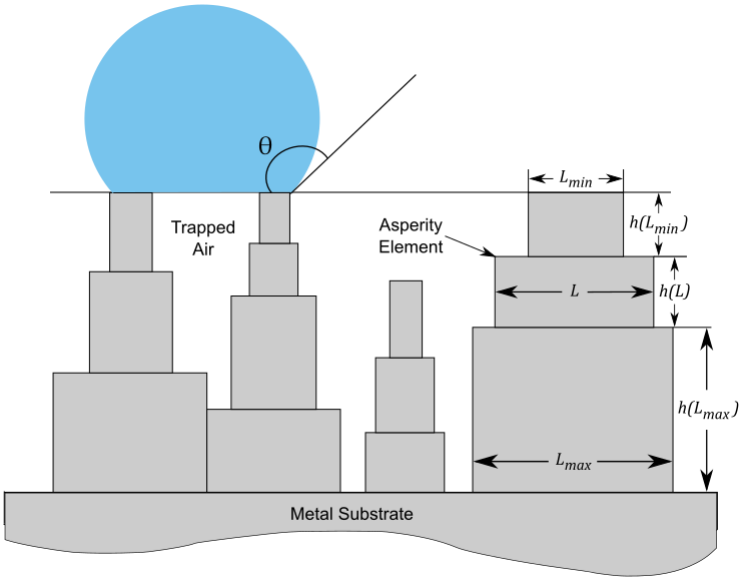

Figure 3. Schematic representation of multiscale, rough, self-affine superhydrophobic surface based on the fractal description with water droplet on top in Cassie state; θ represents the Cassie contact angle, and actual asperity dimensions are much smaller than the droplet size.

The heights and lengths of the asperities can be related to the fractal parameters, D, and G, following the methodology in ref.[65]. The cross-sectional area of asperities is given by $a = L^2$, while the height of any asperity with frequency mode $\gamma^n = 1/L$ can be obtained from eq. (3) and expressed as a power law,

$$\frac{h(a)}{G} = \left(\frac{L}{G}\right)^{2-D} = a^{1-\frac{D}{2}} G^{D-2} \tag{3}$$

where $h(a)$ is the height distribution of any asperity with a cross section area a or L^2.

The size distribution of the multiscale asperities can be expressed by the scaling relation that the number of asperities with area larger than a, $N(A \geq a)$, scales as a fractal with respect to the area a, as[16,65]:

$$N(A \geq a) = \left(\frac{a}{a_{max}}\right)^{-D/2} \tag{4}$$

where a_{max} is the area corresponding to the largest asperity (L_{max}):

$$a_{max} = L_{max}^2 \tag{5}$$

The size distribution, eq. (4), indicates that the number of smaller asperities increases as the value of D increases in the range from 1 to 2. A number density function, $n(a)$, defined as the number of asperities of areas between a and $a + da$, can be estimated from as follows, realizing that the number decreases with increasing area:

$$n(a) = -\frac{dN}{da} = \frac{D}{2a}\left(\frac{a_{max}}{a}\right)^{D/2} \tag{6}$$

The equilibrium contact angle of a surface can be estimated based on the application of the Wenzel or Cassie-Baxter equations, depending upon the applicable wetting state for the surface. As described by Lafuma and Quere[10], the Cassie state is a stable state for a rough surface coated with a low surface energy material that leads to enhanced hydrophobicity of the substrate. On the other hand, the Wenzel model describes the complete wetting of a rough surface (Figure 1b), and the contact angle on a rough surface with stable Wenzel regime may be obtained as:

$$cos\,\theta_w = \; r\,cos\,\theta_0 \tag{7}$$

where θ_w is the stable equilibrium contact angle for a droplet in Wenzel state, r is the roughness ratio of the surface, estimated as the ratio of the overall area of a rough surface to the apparent area, and θ_0 is the Young's contact angle based on an ideal flat surface.

The surface area of any asperity (a_{s_1}), with a cross section area a, can be estimated as:

$$a_{s_1} = a + 4 \cdot h(a) \cdot \mathrm{L} \;\; = \;\; a + 4 \cdot h(a) \cdot a^{\frac{1}{2}} \tag{8}$$

Extending the above representation to an asperity network consisting of two asperities with cross section areas, a_1 and a_2, stacked progressively as in the considered representation, the total surface area (a_{s_2}) can be obtained as:

$$a_{s_2} = (a_2 + a_1 - a_1) + \sum_{n=1}^{2} 4 \cdot h(a_n) \cdot a_{\mathrm{n}}^{\frac{1}{2}} \;\; = \; a_2 + \sum_{n=1}^{2} 4 \cdot h(a_n) \cdot a_{\mathrm{n}}^{\frac{1}{2}} \qquad (9)$$

Therefore, for the considered asperity network as shown in Figure 3, with progressively stacked asperities and cross section areas ranging continuously from a_{min} to a_{max} , the overall surface area (a_s) can be estimated as:

$$a_s = a_{max} + 4 \cdot \int_{a_{min}}^{a_{max}} a^{\frac{1}{2}} \cdot h(a) \cdot n(a) da \qquad (10)$$

The roughness ratio, r, as required to determine the Wenzel contact angle (θ_w) in eq. (7), can then be estimated as the ratio of overall surface area of the asperity network to the area of largest asperity as:

$$r = \frac{a_s}{a_{max}} \;\; = 1 + \frac{4 \cdot \int_{a_{min}}^{a_{max}} a^{\frac{1}{2}} \cdot h(a) \cdot n(a) da}{a_{max}} \qquad (11)$$

where a_{max} and a_{min} are areas of largest and smallest asperities, respectively. Using this roughness and Young's contact angle (θ_0) on a flat substrate (Figure 1a), the Wenzel model contact angle can be estimated.

The Cassie-Baxter model considers trapping of air within the asperities (Figure 1c) and the contact angle is expressed as:

$$cos\,\theta = \;\; r'\phi \, cos\,\theta_0 - 1 + \phi \qquad (12)$$

where θ is the equilibrium contact angle for a droplet in stable Cassie state, ϕ is the fraction of solid region wet by the liquid and r' is the roughness ratio of the wet surface area. Inclusion of r' in eq. (12) enables the consideration of other real partial wetting scenarios where the droplet may wet a 3-dimensional area in places where it makes contact with the surface not only the top-most solid fraction. For a completely stable Cassie state, r' may be taken to be 1 and the corresponding fraction of wetted region (ϕ) can be estimated by considering the wetting of only topmost levels of asperity structure.

Considering the asperities to be randomly distributed throughout the surface, as shown in Figure 3, the area at the topmost level (a_{top}) that is wet by a water droplet can be considered to be equivalent to the area of an averaged asperity element as:

$$a_{top} = \frac{a_{total}}{N} = \frac{\int_{a_{min}}^{a_{max}} a \cdot n(a)\, da}{\int_{a_{min}}^{a_{max}} n(a)\, da} \tag{13}$$

where a_{total} is the total cross sectional area of all the asperities, with areas ranging from a_{min} to a_{max}. The corresponding fraction of wetted region, ϕ, can then be estimated as the ratio of wetted average asperity area to the largest base asperity area:

$$\phi = \frac{a_{top}}{a_{max}} = \frac{\int_{a_{min}}^{a_{max}} a \cdot n(a)\, da}{a_{max} \int_{a_{min}}^{a_{max}} n(a)\, da} \tag{14}$$

Using the fraction of wetted region (ϕ) from the above equation, considering the topmost area (a_{top}) to be flat such that r' = 1, and with the information about the Young's contact angle (θ_0), the equilibrium contact angle for a surface with stable Cassie state can be estimated from eq. (12).

Furthermore, the presented model can be applied to cases of mixed wetting states by considering complete wetting of a certain level of asperities, with wetting along their heights as well. For such a case, r', can be computed as a ratio of the surface area of smallest asperity to its cross sectional area:

$$r' = \frac{a_{min} + 4 \cdot L_{min} \cdot h(L_{min})}{a_{min}} = 1 + \frac{4 \cdot h(L_{min})}{L_{min}} \tag{15}$$

It follows from the above discussion that any multiscale rough surface can be represented by the fractal description based on the W-M equation and the equilibrium contact angle can be readily estimated using the same fractal description. Note that the parameters for the evaluation of the contact angles in each of the wetted states are all obtained directly from a surface profile scan without any empirical adjustment. The model is applied to several real surfaces as discussed in the following section.

3.3. Results and Discussion

3.3.1 SEM Morphology

Several coated samples based on different substrate materials and processes were prepared as discussed in Section 2. Hydrophobic/superhydrophobic surfaces were generated through

electrodeposition at various potentials on copper and zinc substrates, and through etching on aluminum substrates. Scanning electron micrographs of the samples demonstrated hierarchical morphology, with asperities at multiple scales on the as-prepared hydrophobic and superhydrophobic surfaces, as shown in Figure 4. In each of Figures 4a–4c, SEM images at increasing magnifications reveal asperity elements with progressively smaller asperity elements

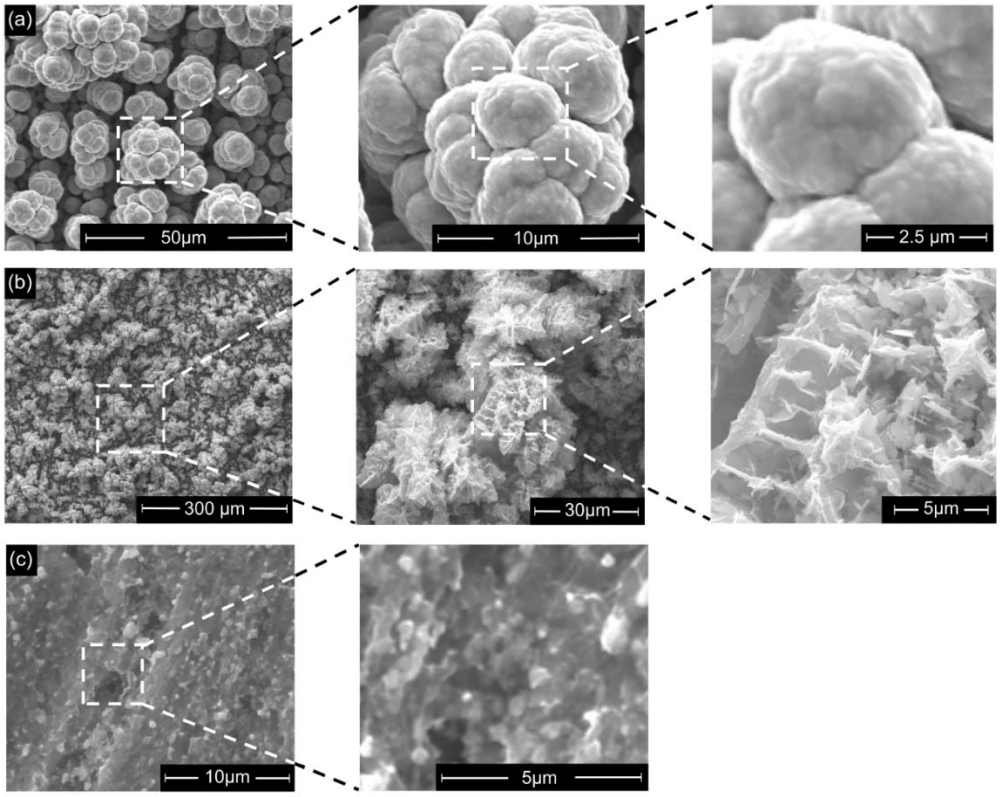

Figure 4. SEM images of coated surfaces at different magnifications showing the presence of asperities at multiple scales for: (a) Copper-based superhydrophobic surfaces (top row); (b) Zinc-based superhydrophobic surfaces (middle row); and (c) Aluminum-based hydrophobic surfaces (bottom row).

situated on top of larger base asperities. Figure 4a demonstrates cauliflower-shaped multiscale fractal morphology on copper-based superhydrophobic coatings deposited at overpotentials exceeding 0.9 V. Figure 4b represents the obtained multiscale random branched and needle-shaped morphology on superhydrophobic zinc sample prepared at –1.4V relative to an Ag/AgCl reference electrode. Branched distribution of asperity elements is observed at a smaller resolution; however, with further increase of resolution, micro-nano scaled needle shaped asperities are seen to be

present on larger branched asperity structures. Furthermore, Figure 4c exhibits globular and needle shaped asperity elements for the aluminum-based hydrophobic surface prepared via etching.

The inherent presence of progressively smaller scale asperity elements on top of larger base asperities as seen in the micrographs in Figure 4 implies the fractal nature of the various prepared coatings. The observed asperity distribution also validates the multiscale geometric representation (Figure 3) considered in the mathematical model, as discussed in Section 3. With the qualitative confirmation of the fractal nature of the asperity elements, further results are presented in the following sections to quantitatively assess the mathematical model and its predictions in the discussion that follows.

3.3.2 Wetting and Fractal Properties

For the prepared copper coatings, a gradual increase in contact angle from 125°–162° was observed with increase in overpotential, with superhydrophobic characteristics being evident for the deposits fabricated at overpotentials greater than 0.9V.

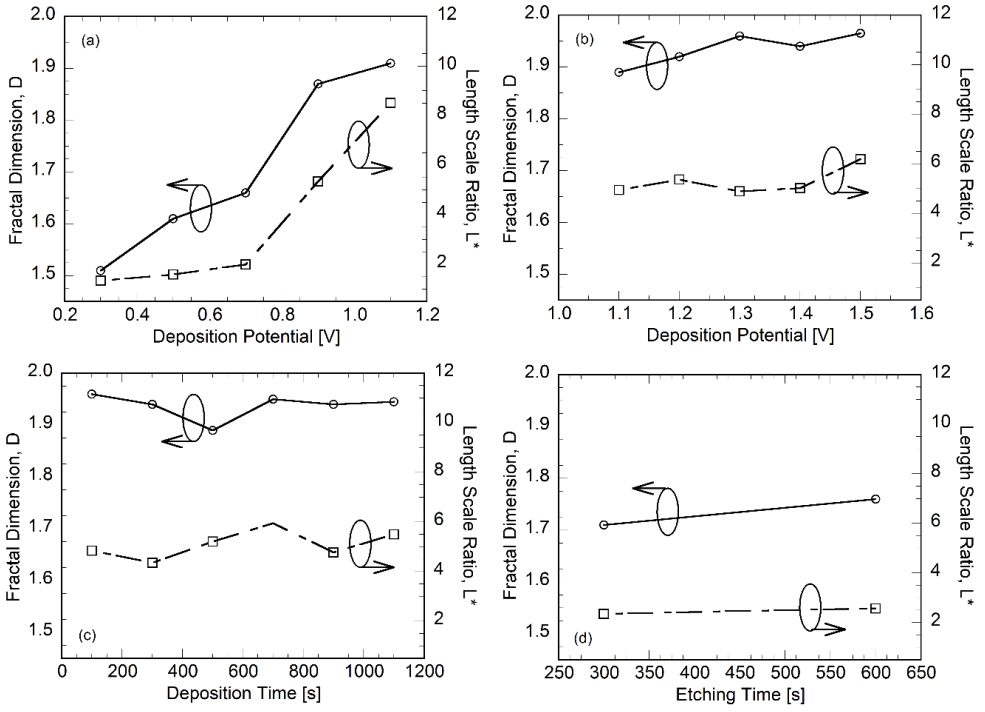

Figure 5. Variation of fractal dimension and length scale range for the prepared surfaces with the processing conditions: (a) Copper deposition at different potentials; (b) Zn/ZnO deposition at different potentials; (c) Zn/ZnO deposition at different deposition times; and (d) Aluminum-based surfaces for different etching times.

A similar increase with overpotential is also seen for the evaluated fractal dimension and asperity length scale for the copper-based coatings, as shown in Figure 5a. Note that all the fractal dimensions are greater than 1 signifying the multiscale fractal nature of the deposited coatings.

Fractal dimensions close to the maximum value of 2 for the coatings prepared at overpotentials above 0.9V demonstrate the highly fractal nature of the surfaces prepared at the high overpotentials, which leads to their inherent superhydrophobic characteristic. During electrodeposition, a high degree of morphological instability is formed in the deposits at the higher overpotentials, due to the smaller growth time constant associated with these processing conditions.[42] This leads to the aggressive fractal nature of the deposits at the high overpotentials.

Zinc-based superhydrophobic surfaces were prepared through electrodeposition at various potentials against a Ag/AgCl reference electrode, at various deposition times. These deposits demonstrated contact angles ranging from 155°–165°, which signifies the extreme wettability of zinc-based coatings. Moreover, the fractal dimensions and length scales of asperities are observed to be nearly independent of the deposition potential and deposition time, as shown in Figures 5b, c. Fractal dimensions of the prepared coatings range from 1.85–1.95 for the several considered deposition parameters, suggesting highly fractal nature of the prepared surfaces irrespective of the processing parameters. The high concentration of KCl in the electrolyte solution leads to a higher conductivity of the solution, which enables the aggressive random growth of Zn/ZnO micro- and nano-structures even at lower deposition potentials and times. For this reason, the evaluated fractal dimensions for the deposits generated at various deposition conditions are nearly independent of the deposition potential and time, and a highly fractal structure is seen for all the deposits.

Aluminum-based coatings, as prepared by etching followed by low energy treatment, show hydrophobic nature with contact angles of 128° and 132° for etching times of 5 and 10 min, respectively. Etching creates roughness on the surface with asperities at multiple scales as observed from their SEM morphology (Figure 4c). Moreover, power spectrum measurements on these surfaces also suggest the presence of fractal behavior and yield fractal dimensions in the range of 1.6–1.7, as shown in Figure 5d.

3.3.3 Model Validation

The asperity network model based on W-M function to depict the multiscale fractal surfaces of the coatings and the model to estimate the static contact angle of these surfaces were validated

for several hydrophobic/superhydrophobic surfaces. As the model only describes the estimation of equilibrium contact angles, dynamic contact angles are not described in this chapter. Dynamic contact angles and contact angle hysteresis will be described in next chapters for both copper and zinc based superhydrophobic surfaces. The validation considered coatings prepared using the different materials, Cu, Zn and Al, and the processes of electrodeposition and etching, as described in Chapter 2. Experimentally measured contact angle may vary from advancing contact angle to receding contact angle. However, with low contact angle hysteresis of $3\text{-}5^0$ on fabricated superhydrophobic coatings, experimentally measured contact angles will practically be same as equilibrium contact angles on these surfaces and may be compared with model equilibrium contact angles for validation.

3.3.3.1 Copper-based coatings

Contact angles for the Copper samples deposited at different overpotentials followed by stearic acid treatment were evaluated using the fractal model presented in Section 3, and compared with experimentally-measured contact angles. The Young's contact angle (θ_o) of the surfaces was measured following organic treatment of the base substrate. The base copper substrate was immersed in 0.02 M methanolic stearic acid solution for 1 hour, similar to the treatment of the as-deposited samples, as described in Section 2.3. This treatment leads to a contact angle of 118 ± 1° on the base Copper substrate, which was used as the value of θ_o in the model. An image of the captured droplet shape on this sample is shown in Figure 6a. Furthermore, the low surface energy treatment of the as-prepared randomly rough samples ensures the stability of Cassie state and, an accurate match to within 3% error is obtained between the experimental and predicted contact angles as shown in Figure 7. The slight over-prediction of contact angles by up to 5% for copper deposition at potentials above 0.7 V may be attributed to the growth of globular shaped asperities at higher overpotentials. Since the mathematical model presented in this paper describes asperities as being square in cross section, the solid surface area in contact with water is estimated to be smaller in comparison to the actual contact area in the case of spherical asperities. The resulting smaller contact of water with the surface leads to a larger contact angle value, as per the Cassie Baxter equation.

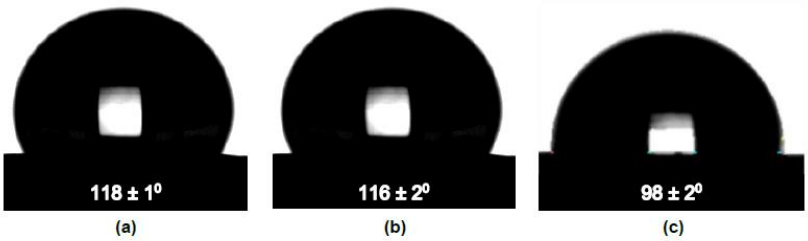

Figure 6. Measured Young's contact angles on flat base substrates with low surface energy treatment: (a) Copper, (b) Zinc and (c) Aluminum.

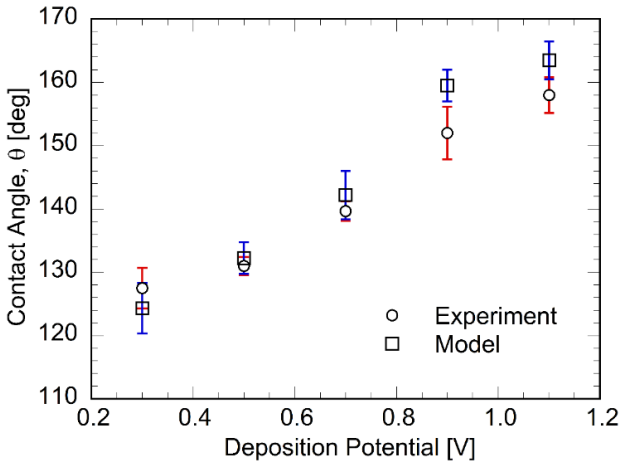

Figure 7. Validation of fractal model with experimental data on as-prepared hydrophobic and superhydrophobic copper based surfaces at different deposition potentials in Cassie state.

3.3.3.2 Zinc-based coatings

The validation studies were conducted on zinc samples made by Zn/ZnO deposition followed by organic treatment. The low surface energy treatment with stearic acid ensures thermodynamic stability of Cassie state on the considered samples[10], as confirmed by the measured low roll off angles in the range of 4–8°. Static contact angle values measured using an FTA-32 contact angle measurement system were compared with the contact angles estimated using the fractal model for various deposition potential and times. The Young's contact angle (θ_o), measured on a flat base substrate treated with stearic acid, was found to be 116 ± 2°, as shown in Figure 6b.

A comparison of the measured and estimated contact angles for zinc-based superhydrophobic coatings are shown in Figure 8. The validation considers different deposition times at 1.3 V (Figure

8a) and different deposition potentials (Figure 8b). It is seen that the measured and the predicted contact angles increase with deposition time as well as with the applied voltage. An error of less than 5% between the measured and estimated contact angle values at various deposition parameters further validates the presented fractal model. No appreciable change in contact angles for various process parameters can be attributed to the presence of multiscale features for coatings deposited irrespective of process parameters.

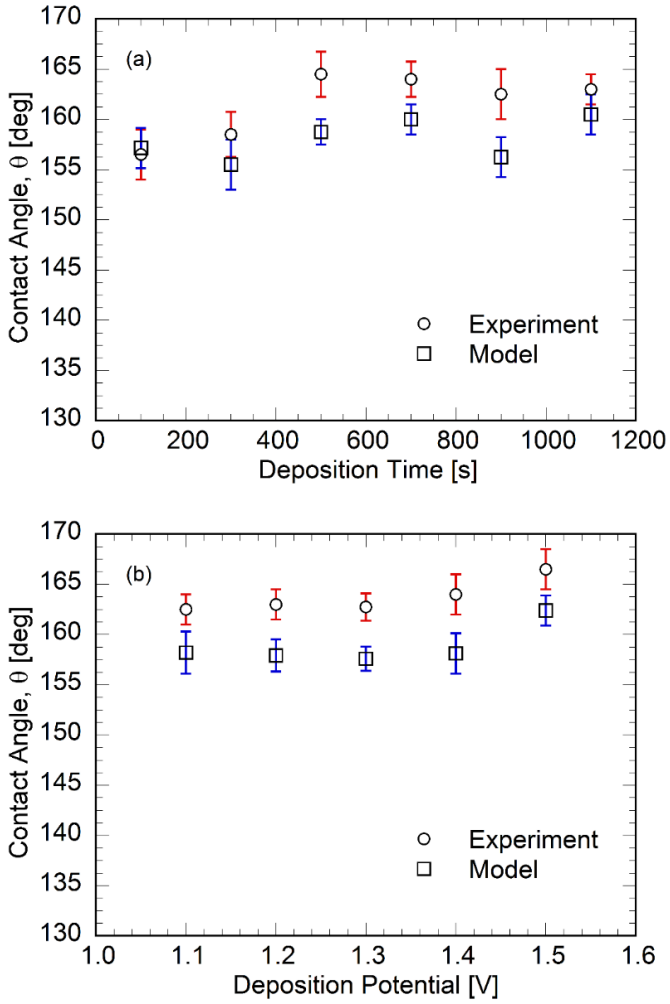

Figure 8. Validation of fractal model with experimental data on as-prepared superhydrophobic zinc based surfaces in Cassie state at: (a) different deposition times and (b) different deposition potentials.

It is seen from Figures 8a and 8b that for the case of Zn/ZnO deposition, the model consistently underpredicts the contact angle values, albeit within a 5% accuracy, unlike the results for Cu

deposition in Figure 7. The underprediction can be explained by the needle-shaped re-entrant morphology with overhangs, observed in the SEM images of the Zn coatings, whereas the present model considers three-dimensional asperities with square cross section. The three-dimensional rectangular asperities correspond to a larger average asperity area at the top in contact with water compared to the actual contact area in the case of the re-entrant structures. This would lead to an under-prediction of contact angle, based on the Cassie-Baxter equation. Contact angle prediction for such re-entrant morphologies can be further improved with incorporation of a surface factor in wetted surface area calculation in Equation 11, based on the shape and size of overhangs.

3.3.3.3 Aluminum-based coatings

Superhydrophobic aluminum (*Al*) samples were prepared by the process as described in section 2. As with the copper and zinc substrates, a flat *Al* substrate was treated with the stearic acid solution to measure θ_o, which was found to be 98° as seen in Figure 6c. Figure 9 compares the measured and predicted contact angles for the Aluminum coatings, fabricated at two different etching times. In each case, the predicted and measured contact angles are close to each other.

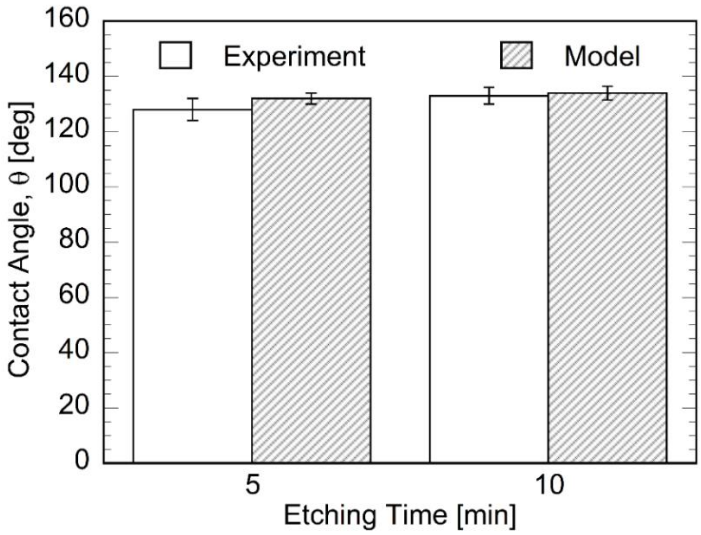

Figure 9. Validation of fractal model with experimental data on as-prepared hydrophobic aluminum-based surfaces in Cassie state at different etching times.

Overall, Figures 7–9 validate the developed fractal model and shows that the model is applicable to superhydrophobic surfaces prepared on various materials using different fabrication techniques. Even though contact angles do not vary appreciably with processing conditions for zinc and

aluminum samples, close match between measured and predicted equilibrium contact angles show the ability of model to predict contact angles independently, based on the surface profile scans.

3.3.4 Effect of fractal dimension and asperity length scale

With the validated model as basis, a study was conducted to assess the influence of the two fractal parameters — fractal dimension and asperity length scale — on the wetting characteristics of a rough superhydrophobic surface. Figure 10 shows the variation of apparent contact angle with the non-dimensional asperity length scale, $L^* = L_{max}/L_{min}$, for fractal dimensions, D, ranging from nearly 1 to nearly 2 and a Young's contact angle of $\theta_o = 115°$ on a surface with stable Cassie state.

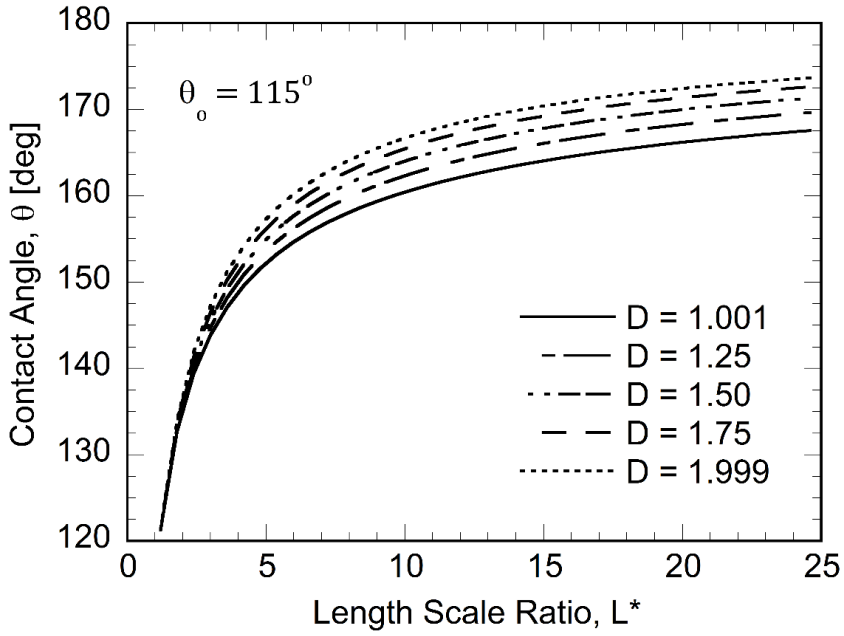

Figure 10. Effects of fractal surface parameters on the apparent contact angle (θ) of the surface with Young's contact angle, θ_0, of 115°.

It can be observed that the presence of asperities over a larger range of length scale (i.e., increasing L^*), leads to a larger contact angle that asymptotically reaches the value of 180^0. This is in agreement with the numerical study of Bottiglione, et al.[56], where it was estimated that the presence of an infinite range of asperities on a surface in Cassie state leads to a contact angle of 180^0. Furthermore, it is observed that for a surface with stable Cassie state, the effect of fractal

dimension on contact angle is relatively less significant. This is consistent with the results of Yang, et al.[58] who reported molecular dynamics simulation of liquid droplets in contact with self-affine surfaces, and showed that the contact angle depends on the root-mean-squared (RMS) roughness of the surface and is nearly independent of fractal dimension. Furthermore, equilibrium contact angles were also found to be practically independent of the scaling parameter, G. The model can be used to design engineered surfaces with the required range of asperity length scale and fractal parameters to generate desired superhydrophobic characteristics. For a surface with Young's contact angle of $\theta_o = 115°$, with stable Cassie state, superhydrophobicity can be obtained with creating a multiscale nature with largest to smallest asperity length scale ratio of nearly 5.

The results presented in this section demonstrate detailed validation of the fractal model in accurately predicting contact angles of rough surfaces. The model is unique in that it uses no empirical tuning factors and is shown to be applicable across different materials and fabrication processes. The model can be used to design engineered surfaces with the required range of asperity length scale and fractal parameters to generate desired superhydrophobic characteristics. This, in turn, can be used to design processing conditions to achieve the desired surface properties on various substrate materials. Since the superhydrophobic coatings are generated inherently on the substrate material, unlike current practice of using a coating material that differs from the substrate material, the durability and longevity of the coatings are dramatically improved. These aspects will be considered in detail in a separate study. Additionally, described fractal concepts will be extended to the estimation of dynamic behavior of droplet and contact angle hysteresis on such surfaces, in a future study. The model can also be employed towards the wettability estimation of a deforming solid, following the work of Marchand, et al.[67] Moreover, as suggested in the recent studies by Mitra, et al.[68,69], surrounding viscous media may significantly affect the wetting behavior of any surface, governing equations as derived in the present study may be modified to accommodate such factors and will be considered as a future study.

3.4. Conclusions

The study considered analysis of wettability on randomly rough surfaces that were shown to exhibit self-affine fractal characteristics. The surfaces were described by an asperity network fractal model based on Weierstrass-Mandelbrot (W-M) function, where fractal parameters are uniquely determined by power spectrum of the surface. A model for predicting the apparent contact

angle was developed based on the different wetting regimes. Experimental measurements on various hydrophobic and superhydrophobic surfaces fabricated using several materials and processing conditions were used to demonstrate the accuracy of the model predictions. In all the cases, the predictions were shown to be well within 5% of experimental measurements for different materials and fabricating processes. Furthermore, the contact angle is found be positively dependent on the range of asperity length scale and nearly independent of the fractal dimension for a surface in a stable Cassie state. Hence, creation of multiscale nature and increasing length scale ratio, on a surface in Cassie state, are required parameters to generate superhydrophobicity. The model provides a truly predictive approach to estimating the contact angles on rough surfaces, without the use of any empirical fitting or tuning parameters. Using the model, the fractal parameters required to generate superhydrophobicity on a particular substrate can be derived for any material and coating process.

Chapter 4. Facile Fabrication of Durable Copper Based Superhydrophobic Surfaces via Electrodeposition

Superhydrophobic surfaces have myriad industrial applications, yet their practical utilization has been limited by their poor mechanical durability and longevity. We present a low cost, facile process to develop superhydrophobic copper based coatings via electrodeposition route, that addresses this limitation. Through electrodeposition, a stable, multiscale, cauliflower shaped fractal morphology was obtained and upon modification by stearic acid, the prepared coatings show extreme water repellency with contact angle of 162 ± 2^0 and roll-off angle of about 3^0. Systematic studies are presented on coatings fabricated under different processing conditions to demonstrate good durability, mechanical and underwater stability, corrosion resistance and self-cleaning effect. The study also presents an approach for rejuvenation of slippery superhydrophobic nature (contact angle hysteresis $< 10^0$) on the surfaces after long term water immersion. The presented process can be scaled to larger, durable coatings with controllable wettability for diverse applications.

4.1. Introduction

Many naturally occurring surfaces such as lotus leaves[45] and water striders[46,47] are known to exhibit superhydrophobic and self-cleaning properties and have inspired research to understand and mimic these properties artificially. Superhydrophobic surfaces exhibit high water contact angles, greater than 150^o, and small contact angle hysteresis of less than 10^o. [1,5] Through studies based on naturally occurring superhydrophobic surfaces, researchers have observed that hierarchical or multiscale morphology, such as a combination of micro- and nano-structures, together with the low energy of the surface, leads to the superhydrophobic nature of a surface.[6,7] In general, two types of wetting states are observed on such surfaces namely, Wenzel state[8] and Cassie state[9]. In the Wenzel state, a water droplet fills the roughness grooves present on the surface, leading to the pinning of droplet to the surface and does not allow the surface to self-clean. On the other hand, in Cassie state the droplet does not penetrate into the surface due to the entrapment of air within the surface roughness and cavities as shown in Figure 1, leading to high contact angles and very low sliding angles.[7,10]

Superhydrophobic surfaces are known for their vast range of applications and properties such as self-cleaning[17,18], drag reduction[19,20], improved phase change heat transfer[21,22], anti-icing[23,7], anti-corrosion[7,24]. Although significant developments have been made in the processes and materials to fabricate superhydrophobic surfaces, very few of them have shown their viability in industrial applications. This is due to their poor mechanical strength, abrasion resistance, transition from slippery Cassie to sticky Wenzel state, and durability of the superhydrophobicity and plastron layer under water immersion. Mechanical strength and durability of superhydrophobic coatings are, therefore, of considerable focus in recent studies. Many researchers have employed sandpaper based shear abrasion test to evaluate the mechanical durability of the superhydrophobic surfaces.[25-29] However, only a few have reported satisfactory mechanical durability. For instance, superhydrophobic surface prepared by Mg-Mn-Ce deposition on a magnesium substrate was reported to lose its superhydrophobicity after abrasion for 400 mm with an applied pressure of 1.3 kPa.[26] Another superhydrophobic surface on copper substrate by nickel deposition maintained the superhydrophobic nature till 1000 mm abrasion under a load of 4.8 kPa on 800 grit sandpaper.[25] However, practical application of such surfaces would require them to sustain their properties to a significantly larger duration.

Furthermore, it is known that when the superhydrophobic surfaces are immersed in water, the exchange of air between entrapped air cavities and bulk water gradually leads to the wetting transition from Cassie state to pinned Wenzel state and a resulting loss of the superhydrophobic nature.[70,71] Furthermore, under flowing water conditions, this phenomenon is enhanced and the durability of superhydrophobic surface is further reduced.[70,72] Recently, a few authors have reported durability studies on submerged superhydrophobic coatings by correlating superhydrophobic nature with submersion time.[30,31,73] Fan et al[73] showed that superhydrophobicity of steel based coating was maintained under water immersion for 6 days, whereas superhydrophobicity was lost after only 80 hours of water immersion for magnesium alloy based superhydrophobic surfaces developed by Chu et al.[30] Lv et al[31] showed that superhydrophobicity was maintained after 12 days of water immersion for the as-prepared coating on a copper mesh. In all these studies a steady loss in superhydrophobic nature of coatings with immersion time was observed. Though practical applications of superhydrophobic surfaces would require them to be in contact with steady as well as flowing water for significantly longer durations, studies are rather limited in performing extensive durability studies in such environments. This suggests the need

for a consistent testing methodology to study the durability of superhydrophobic coatings submerged in steady and flowing water conditions for longer durations and the development of durable coatings which can maintain superhydrophobicity for practical durations in such conditions.

Among the superhydrophobic coatings on metallic substrates, copper has attracted significant interest. Copper has wide industrial applicability and is used in heat exchangers, pipelines, and electrical appliances due to its good thermal and electrical conductivity in addition to mechanical stability. It has been shown by many researchers that the application of superhydrophobic coating improves the corrosion resistance of copper.[74] Several techniques such as chemical vapor deposition[75], solution-immersion[76], spray coating[77], etching[78], magnetron sputtering[79], and electrodeposition[80-84] have been used to develop copper based superhydrophobic surfaces. However, industrial scalability of some of the reported techniques is rather limited, due to the associated manufacturing and time costs. Due to low cost, uniform deposition irrespective of size and shape, and industrial scalability, electrodeposition is considered as one of the most effective technique for large scale generation of superhydrophobic surfaces[85,36]. Wang et al.[82] electrochemically fabricated hierarchical cupreous microstructures from copper nitrate solution, followed by treatment in n-dodecanethiol for lowering the surface energy. Haghdoost and Pitchumani[35] presented a two-step process without any low energy treatment to fabricate superhydrophobic copper coatings that exhibited cauliflower shaped morphology at high overpotentials through an acidic electrolyte. Shirtcliff et al.[81] used high current density followed by fluorocarbon treatment to obtain superhydrophobicity on a copper substrate. Wang et al.[84] deposited copper using a copper sulfate electrolyte and modified it by lauric acid to achieve superhydrophobicity, and showed the improved corrosion resistance due to the superhydrophobic coating. However, none of these studies reported the mechanical strength, abrasion resistance and under-water durability of the copper based superhydrophobic coatings.

It is evident from the foregoing discussion that most of the superhydrophobic coatings developed to date have rather limited mechanical strength and durability. To overcome these limitations, the present work presents a facile and cost-effective process based on electrodeposition to fabricate superhydrophobic copper coatings integral on copper substrates, and reports extensive mechanical and water immersion characterization of the coatings. Through electrodeposition at a large overpotential, followed by second-step deposition at low potential for a short duration, stable

deposits with multiscale fractal, cauliflower-shaped morphology are obtained on copper substrates[35]. The electrodeposited samples are then modified by treatment with inexpensive stearic acid to achieve superhydrophobicity. Contact angles (θ) of 162 ± 3^0 and roll-off or sliding angles (θ_s) of about 3^0 are obtained on the as-fabricated superhydrophobic surfaces. A comprehensive study of the effect of applied overpotential on the morphology and wettability is presented and discussed. Furthermore, systematic studies are described to evaluate the chemical composition, growth mechanism, mechanical abrasion stability, corrosion resistance, self-cleaning effect, air-exposure durability, durability under steady water, and durability under flowing water conditions of the optimal superhydrophobic surfaces. Mechanical abrasion tests are conducted on the coatings and the results are presented in terms of a combined energy parameter that encapsulates the effects of load, abrasion distance, and coefficient of friction. Using this representation, various recently prepared superhydrophobic surfaces have been compared with the as-prepared copper coatings. This study also discusses rejuvenation of slippery superhydrophobic nature ($\theta_s < 10^0$) on the as prepared surfaces.

Various results such as morphology, wettability, corrosion resistance, durability, and rejuvenation of superhydrophobic surfaces are discussed in following sections.

4.2. Results and Discussion

4.2.1 SEM morphology and wetting characterization

The effects of applied overpotential on morphology and wettability for as-fabricated copper coatings were comprehensively studied. Scanning electron micrographs, respective droplet shapes, and static contact angles are shown in Figure 11 for the samples deposited at overpotentials ranging from 0.5 to 1.1 V, with an increment of 0.2 V. A gradual transition from needle-shaped asperity structure at lower overpotentials (Figure 11a) to a globular morphology for coatings deposited at larger overpotentials is observed. Globular features start to appear for coatings deposited at overpotentials of 0.7 V (Figure 11b), transitioning to an aggressive cauliflower-shaped multiscale fractal morphology for coatings deposited at overpotentials exceeding 0.9 V (Figures 11c, d). The similarity of these morphologies to the morphologies of single layer copper deposits reported by Haghdoost and Pitchumani[36] suggests that the morphologies are not altered by the second layer deposit at low overpotential and stearic acid treatment.

A gradual increase in static contact angle (θ) from 125° to 162° is observed in Figure 11 with increase in overpotential, with superhydrophobic characteristics being evident for the deposits fabricated at overpotentials greater than 0.9 V. For reference, the contact angle measured on a flat copper substrate treated with stearic acid was found to be 116°. The creation of a multiscale fractal morphology on the substrate and treatment with stearic acid lead to a stable Cassie state for the as-prepared surfaces. At the high overpotentials, the larger globular asperities are seen to be covered with progressively smaller globular asperities (Figures 11c, d), leading to the presence of asperities at multiple scales.

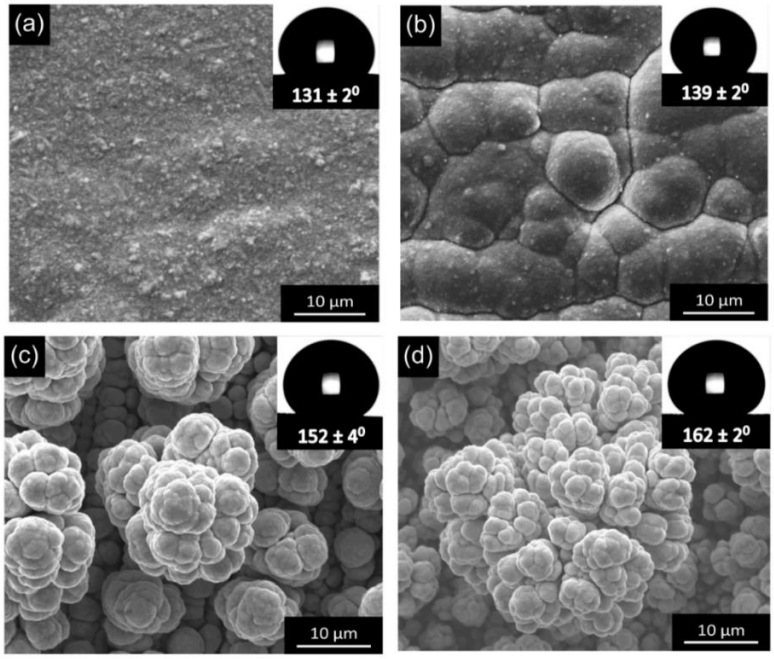

Figure 11. SEM morphologies and water contact angles of electrodeposited copper samples fabricated at overpotentials of (a) 0.5 V, (b) 0.7 V, (c) 0.9 V, and (d) 1.1 V, showing growth of globular shaped asperities beyond overpotential of 0.7 V; Respective representative water droplet and contact angle are displayed in the insets.

The gradual increase of multiscale features with overpotential leads to the observed increase in static contact angle with overpotential. An aggressive fractal texturing with globular asperities at multiple scales leads to the observed superhydrophobicity with equilibrium contact angles of 152 ± 4° and 162 ± 2°, for deposits prepared at 0.9 V and 1.1 V, respectively. Here contact angles are represented as averaged equilibrium contact angles and associated experimental uncertainty, estimated through contact angle measurements on three different locations on three different

samples deposited at specific overpotential. Haghdoost and Pitchumani[35] explained the presence of aggressive fractal texture at higher overpotentials by the model of unstable growth during electrodeposition and suggested that more morphological instabilities are formed on deposits fabricated at higher overpotentials due to a smaller growth time constant.

In order to test the durability and sustained performance of the superhydrophobic coatings, surfaces prepared with an overpotential of 1.1 V, exhibiting maximum static contact angle, were considered for further studies such as dynamic wettability, mechanical durability, water immersion, corrosion and other characterizations, as discussed in this and the following subsections.

Dynamic wettability of electrodeposited copper coatings at an overpotential of 1.1 V was examined under several dynamic conditions such as droplet sliding or roll-off angle (θ_s), dynamic behavior of a single water droplet impact, dynamic behavior of impinging water stream, and contact angle hysteresis on the coated surface. A 10µl water droplet placed on the sample rolled off the nearly horizontal surface and a roll off angle of about 3° was measured, demonstrating the excellent water repellent property of the considered sample. The dynamic behavior of impinging water droplets and impinging water stream on the considered superhydrophobic sample were captured using a high-speed camera. A 10µl water droplet, dropped from a height of 4 cm bounced off the coated surface several times, before sliding off as shown by successive snapshots in Figure 12a, where the time interval between two successive snapshots is 0.67 s. Moreover, an inclined water stream on the considered surface reflects without leaving any trace of water on the surface, as shown in Figure 12b, which shows the strong non-wettable nature of the as-prepared copper based superhydrophobic surface.

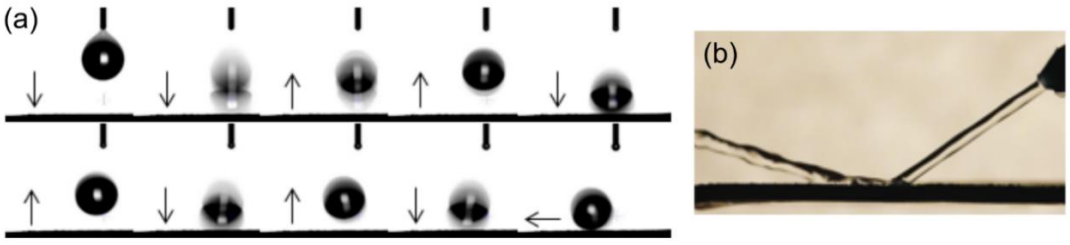

Figure 12. Strong superhydrophobic nature of the prepared surfaces: (a) successive snapshots of a water droplet dropped on a superhydrophobic sample; time interval between successive snapshots is 0.067 s; and (b) impinging water stream at an angle being reflected by the superhydrophobic samples.

Furthermore, as described in methods section, the dynamic wetting property of the developed superhydrophobic copper coating was characterized through the volume changing dynamic sessile drop technique. Representative advancing and receding droplet shapes are shown in Figures 13a and 13b, respectively. Based on the measured advancing and receding contact angles, a very small contact angle hysteresis ($\theta_a - \theta_r$) of about 4° is evaluated, which further demonstrates the extreme non-wettability of the as-prepared superhydrophobic coating.

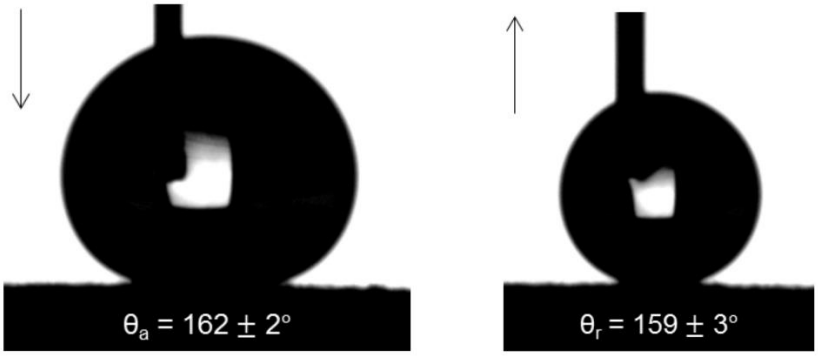

Figure 13. Dynamic contact angles with representative water droplet shapes on copper based superhydrophobic surface: (a) advancing contact angle and (b) receding contact angle.

4.2.2 Elemental analysis of the superhydrophobic samples

Energy dispersion spectroscopy (EDS) analysis of the superhydrophobic sample fabricated at an overpotential of 1.1 V was carried out through FEI Quanta 600 scanning electron microscope (SEM) to estimate the elemental composition of the prepared coatings and to study the effect of stearic acid treatment on the electrodeposited copper coating. Figure 14 shows the EDS spectra for (a) a copper sample without stearic acid treatment and (b) a treated superhydrophobic copper sample. Untreated electrodeposited copper sample is primarily composed of Cu and O elements (Figure 14a), where the presence of a small percentage of oxygen can be attributed to the oxidation of the deposited surfaces. For coatings treated with stearic acid, additional carbon element is observed in Figure 14b. Figure 14 also presents the normalized mass percent of respective elements on untreated and treated samples, based on the EDS spectra. With 99.01% and 93.66% by mass, copper remains the primary element in both untreated and stearic acid treated samples, respectively. Treatment of electrodeposited coatings with stearic acid solution leads to the

formation of copper stearate on the copper based substrate[74], as described by the equation: $Cu^{2+} + 2CH_3(CH_2)_{16}COOH \rightarrow Cu[CH_3(CH_2)_{16}COO]_2 + 2H^+$.

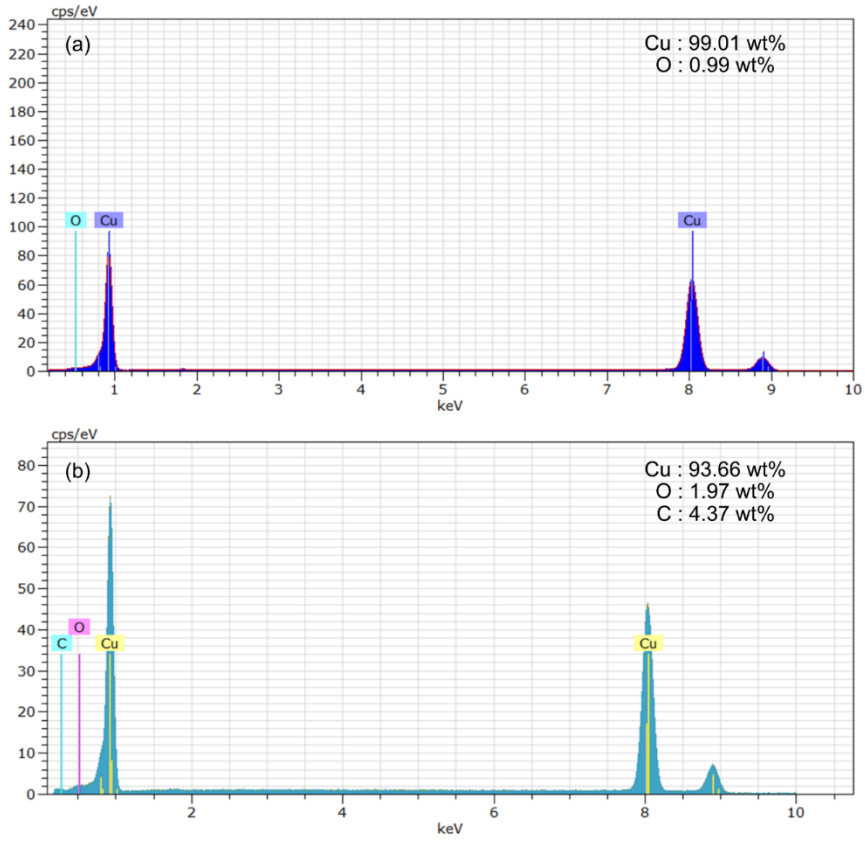

Figure 14. EDS spectra for (a) unmodified deposited copper sample and (b) superhydrophobic copper sample.

4.2.3 Self-cleaning property

Self-cleaning characteristics of the as-prepared superhydrophobic surfaces were evaluated in comparison to a bare substrate by placing a layer of SiC particles on each of the surfaces initially, and examining the cleaning of the surfaces with gradually increasing number of water droplets. Both superhydrophobic and bare copper samples were kept inclined at nearly 10^o. Each droplet consisted of 10 µl of deinonized water, and was gently dropped on the top portion of the sample surfaces using a micropipette. The water droplets rolled or moved down the surfaces, collecting the contaminant sand grains.

The results are shown in Figure 15, where the sample to the left in each frame is the superhydrophobic copper surface and the sample to the right is the bare copper substrate. and

covered with a layer of silicon carbide sand particles. Figure 15a shows the initial layer of SiC on the two samples, and Figures 15b–15f depict the extent of cleaning on the two samples for progressively increasing number of water droplets. It is seen that in the superhydrophobic samples, the water droplets rolled off easily collecting the SiC particles with them. However, sand particles adhered to the bare copper substrate, when water was dropped on it. Furthermore, as seen in Figure 15d, the superhydrophobic copper sample was completely cleaned with less than 10 water droplets (< 100 µl total volume). In contrast, the bare copper substrate required at least 55 water droplets (> 550 µl total volume) to clean the same amount of sand particles (Figure 15f). This demonstrates the excellent self-cleaning property of the as-prepared superhydrophobic copper coatings.

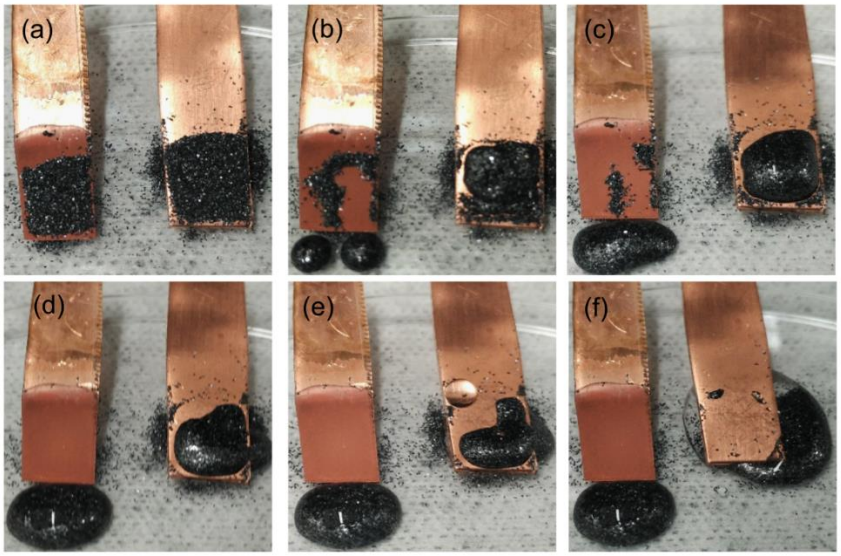

Figure 15. Self-cleaning property of superhydrophobic copper surface (sample to the left in each frame) in comparison to bare copper substrate (sample to the right in each frame) based upon cleaning with water droplets of 10µl each: (a) initial accumulation of SiC particles on both samples and after cleaning with (b) 2 water droplets; (c) 5 water droplets; (d) 10 water droplets; (e) 30 water droplets; and (f) 55 water droplets.

4.2.4 Anti-corrosion property of the superhydrophobic surfaces

Corrosion properties of the fractal superhydrophobic coating prepared at the overpotential of 1.1 V, were examined by evaluating their potentiodynamic polarization plots in 3.5 wt% NaCl solution. Based on measured data, Tafel extrapolation was used to estimate the quantitative corrosion parameters. The measured potentiodynamic polarization curves for the

superhydrophobic and base copper samples are shown in Figure 16, which are used to derive the corrosion potential (E_{corr}), corrosion current density (I_{corr}) and polarization resistance (R) as summarized in Table 1.

Table 1. Corrosion parameters for base copper and superhydrophobic copper in 3.5 wt% NaCl solution

Material	E_{corr} [V]	I_{corr} [$\mu A/cm^2$]	Corrosion resistance [kΩ]	Corrosion rate [mm/year]
Base Copper	–0.142	4.700	3.29	0.109
Superhydrophobic Copper	–0.228	0.394	32.13	0.009

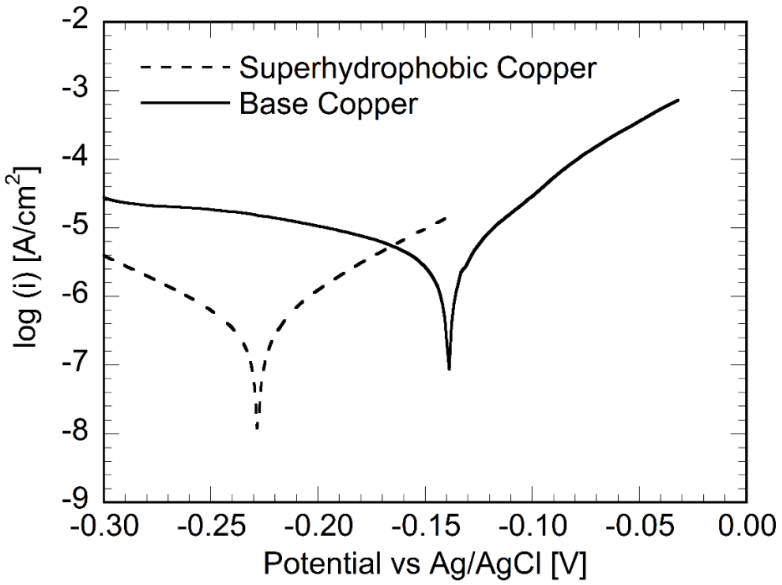

Figure 16. Potentiodynamic polarization curves for superhydrophobic and base copper in 3.5 wt% NaCl solution.

In general, a higher corrosion potential and a lower current density correspond to a better corrosion resistance[74,40]. For the as-prepared superhydrophobic coating, a slight reduction in E_{corr} and a significant reduction in I_{corr} by more than one order of magnitude are observed in comparison to a bare copper substrate. This leads to a significantly higher polarization resistance of the

superhydrophobic coating relative to the bare copper substrate, as listed in Table 1, and demonstrates the significantly improved anti-corrosion properties of the superhydrophobic copper surface. The improved anti-corrosive nature of the superhydrophobic coatings can be explained by the presence of a stable Cassie state, which ensures the trapping of air within the roughness features of the surface. The presence of trapped air presents a cushion effect that avoids the contact of the surface region with NaCl solution.[40] As corrosion is a surface phenomenon, reduced contact of the surface with the salt solution leads to a reduced corrosion rate.

4.2.5 Mechanical durability of the superhydrophobic surfaces

One of the factors limiting the use of superhydrophobic surfaces in practical applications is the lack of mechanical robustness.[41] The limitation is particularly severe because of delamination at the interface between the dissimilar coating and substrate materials in conventional coatings. The method presented in this paper generates superhydrophobic surfaces inherently on the substrate material using electrodeposition, thereby eliminating the interface that's often the weak link in the mechanical durability. The mechanical durability of the as-prepared superhydrophobic surfaces in this study was evaluated using shear abrasion[25-29] and falling sand abrasion tests[86,87].

Figure 17a shows a schematic of the shear abrasion test derived from ASTM D4060[88], in which the superhydrophobic surfaces were dragged on 1000 grit and 800 grit sandpapers under a load of 3 kPa, for a distance of 200 cm, at a speed of 1 cm/s. Mechanical abrasion leads to a gradual loss of non-wetting nature through decrease in contact angle and increase in contact angle hysteresis. In order to analyze the combined effects of abrasion surface roughness (sand paper grit size), pressure load, and abrasion distance in a unified manner, a parameter based on the frictional energy dissipation was used. The frictional energy parameter was defined as the product of three terms—the ratio of coefficient of friction of considered sandpaper and that of a 1000 grit sandpaper for a particular sample [$\mu/\mu(1000)$], the applied pressure, and the abrasion distance—and signifies the frictional energy per unit area with respect to abrasion on a 1000 grit sandpaper. The static coefficient of friction used in calculating the friction energy parameter was estimated as the tangent of the angle at which the substrate slips off a sandpaper surface. Using this method, the ratio of the coefficient of friction for 800 grit sandpaper to a 1000 grit sandpaper [$\mu(800)/\mu(1000)$] for a pure copper substrate as well as superhydrophobic copper substrate were estimated to be nearly constant at about 1.17. The use of the frictional energy parameter also serves to compare the obtained results

with those reported in the literature[25-29] for the different grit sizes, pressure and abrasion distance in a common manner.

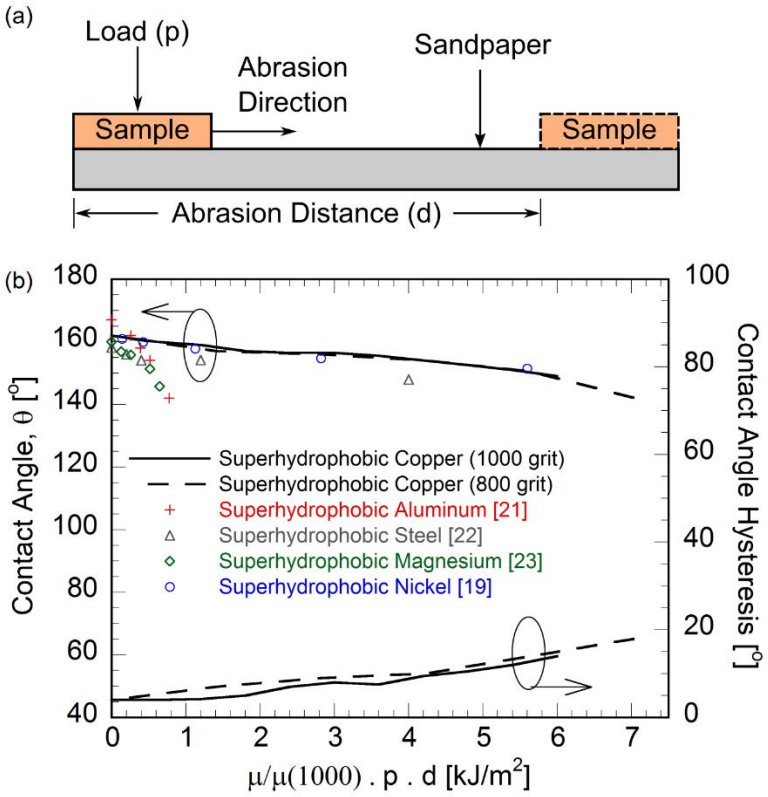

Figure 17. (a) Schematic of the shear abrasion test setup and (b) variation of the contact angle and contact angle hysteresis for superhydrophobic copper surface with relative frictional energy per unit area, in comparison to several recently reported superhydrophobic coatings on different metallic substrates.

The degradation in superhydrophobicity of the samples was assessed by measuring the contact angle and hysteresis as a function of abrasion length. Figure 17b presents the measured contact angle on the superhydrophobic copper samples in this study as function of the friction energy parameter for the two grit sizes used. The solid lines and the dashed lines, respectively, denote the variation of the contact angle (left axis) and the contact angle hysteresis (right axis) for the 1000 and 800 grit sizes. It is seen that the contact angle decreases and the contact angle hysteresis increases slightly with the parameters contributing to an increased frictional energy dissipation. After a 200-cm abrasion distance (corresponding to a frictional energy parameter of about 7 in Figure 17b), some loss in superhydrophobicity was observed resulting in a reduced contact angle

of 149.5 ± 2^0 and increased hysteresis of about 14^0. However, the sample remained superhydrophobic and was not wetted by water. Also presented in the same figure are the shear abrasion test data from the literature on different materials, at different abrasion conditions.[25-29] Note that there is insignificant variation between the results of shear abrasion on 800 and 1000 grit sandpaper for all abrasion distances, which confirms that the data from shear abrasion for various sandpapers, load and abrasion distance can be combined elegantly in terms of the friction energy parameter, for a consistent and uniform representation (Figure 17b).

In addition, shear abrasion data from several superhydrophobic coatings recently reported in the literature[25-29] were expressed in terms of the abrasion energy parameter, and are compared against the superhydrophobic copper coating in the present work, as shown in Figure 17b. The coatings on Magnesium[26] and Aluminum[27] are seen to lose their superhydrophobicity within about 1 kJ/m^2 and the coatings on steel are reported to withstand up to 4 kJ/m^2. Though the nickel-based superhydrophobic coating developed by Su and Yao[25] is seen to maintain its contact angle to 6 kJ/m^2, the coating was reported to have an increased roll-off angle of about 30^0 after the shear abrasion test, indicating that the superhydrophobicity was lost quickly. In contrast, it is seen that the superhydrophobic copper coatings in the present work exhibit better mechanical abrasion resistance and maintain excellent superhydrophobicity over much higher levels of abrasion energy, up to 7 kJ/m^2, than the other superhydrophobic surfaces.

To further evaluate the mechanical durability of the prepared coatings, falling sand abrasion tests based on ASTM D968[39], were performed, as shown schematically in the inset of Figure 18. Silicon carbide grains (100–250 μm in diameter) were impinged on the samples inclined at an angle of 45^0, from a height of 20 cm, at a rate of 0.25 kg/min. Previous studies in the literature on falling sand abrasion tests were rather limited in the abrasive mass, allowing only up to 10–50 gm of the abrasives to fall on the superhydrophobic samples.[86,87] In the present study, the durability of the superhydrophobic surfaces were demonstrated with more aggressive conditions with up to 1000 gm of falling abrasive silicon carbide grains on the samples. For better physical understanding, the combined effects of drop height and considered mass of grains are presented in terms of potential energy of silicon carbide particles per unit impact area. Variation of contact angle and contact angle hysteresis were measured after every 200 gm of grain flow, and are presented in Figure 18 as function of energy per unit impact area for the prepared copper superhydrophobic surfaces. The experiments were repeated three times, and the data are presented

in Figure 18 in terms of the mean and the error bars. It is seen that the contact angle decreases and the contact angle hysteresis increases slightly with abrasion, signifying some loss in superhydrophobicity, as expected. However, at the end of the aggressive falling sand abrasion test, the considered samples remained superhydrophobic, as evident from a contact angle of about 153^0 and hysteresis of about 12^0. Note that these tests were conducted with 20–100 times the amount of abrasives compared to those used in the tests in the literature. In the conventional range of testing, therefore, which correspond to energy per unit impact area of less than 0.04 J/cm^2, there is insignificant change in the contact angle and hysteresis seen in Figure 18. The falling abrasive tests under the aggressive conditions, therefore, demonstrate a significantly enhanced durability of the superhydrophobic copper coatings fabricated in the present study.

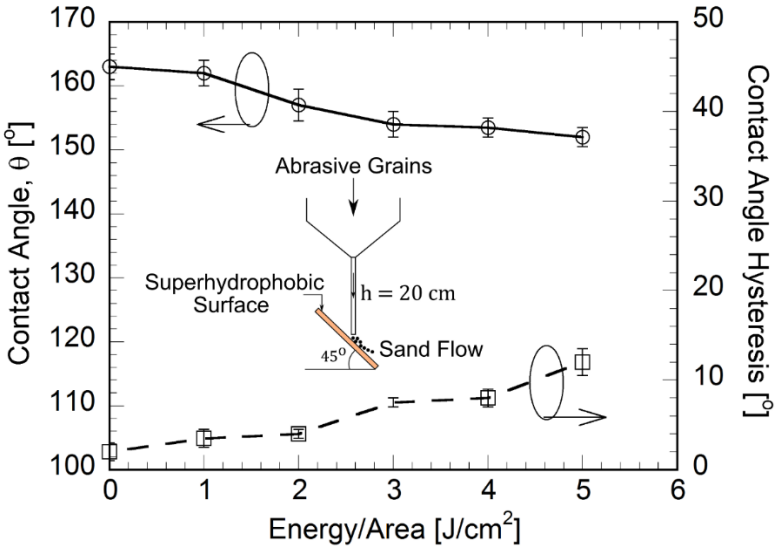

Figure 18. Variation of contact angle and contact angle hysteresis with impact energy per impact area for copper based superhydrophobic surfaces subject to falling sand abrasion test. Inset figure shows a schematic of the falling sand abrasion test setup.

4.2.6 Durability of Superhydrophobic surfaces under air exposure, water immersion and flow conditions

Changes in the wetting properties of the copper based superhydrophobic surfaces in this study were observed during air exposure for up to 6 months. No practical changes in the static contact angle (161^o), contact angle hysteresis (3.0^o), and roll-off angle (4.0^o) were observed during the

exposure period demonstrating the excellent superhydrophobic properties of the coatings under long duration air exposure.

Furthermore, practical applications of superhydrophobic surfaces for drag reduction, self-cleaning, phase change heat transfer enhancement etc. require them to be in contact with aqueous media for long term. However, transfer of trapped air under the cavities to the bulk surrounding water can lead to the transition from the stable Cassie state to the Wenzel state for the superhydrophobic surface, leading to the loss of superhydrophobicity. Moreover, longevity of a submerged superhydrophobic surface mainly depends on the amount of time air can stay trapped within the cavities present on the surface.[70] This phenomenon limits the practical applicability of the superhydrophobic surfaces.

Water immersion tests were conducted on the copper based superhydrophobic surfaces prepared in this study, under static and dynamic conditions. Immersion tests were conducted following the practices outlined by ASTM D870, standard practice for testing water resistance of coatings using water immersion.[89] In the static immersion tests, the samples were immersed in deionized water for about 60 days, and the static and dynamic contact angles were measured at various time instants during the exposure. Figure 19a presents the contact angle and contact angle hysteresis measurements on the different samples during the 60-day static immersion test. The variations in the measurements among the different samples are plotted in terms of the mean value and the error bar for each data point. It is seen that the contact angle decreases and the contact angle hysteresis increases with immersion time. After 60 days of water immersion, contact angle of copper based surface was reduced to 149^{o} (from the initial value of 162^{0}) and contact angle hysteresis was increased to 23^{o}, which suggests the loss of some of the entrapped air to the bulk water. Furthermore, even after 60 days of immersion, with periodic removal for contact angle measurements, the copper sample was completely dry when removed from the water and no change in morphology was observed (as shown by the inset in Figure 19a), suggesting the durability of the superhydrophobic copper surfaces even after prolonged aqueous exposure under static conditions.

As flowing water is known to enhance the rate of the loss of entrapped air from a superhydrophobic surface[70], durability of the copper-based superhydrophobic surfaces was also studied under flow conditions, as described in methods section. The samples were immersed in flowing water for 60 days, with periodic removal during the testing for measurement of contact

angles and contact angle hysteresis. Figure 19b shows the variation of the measured angles with time during the dynamic water immersion testing.

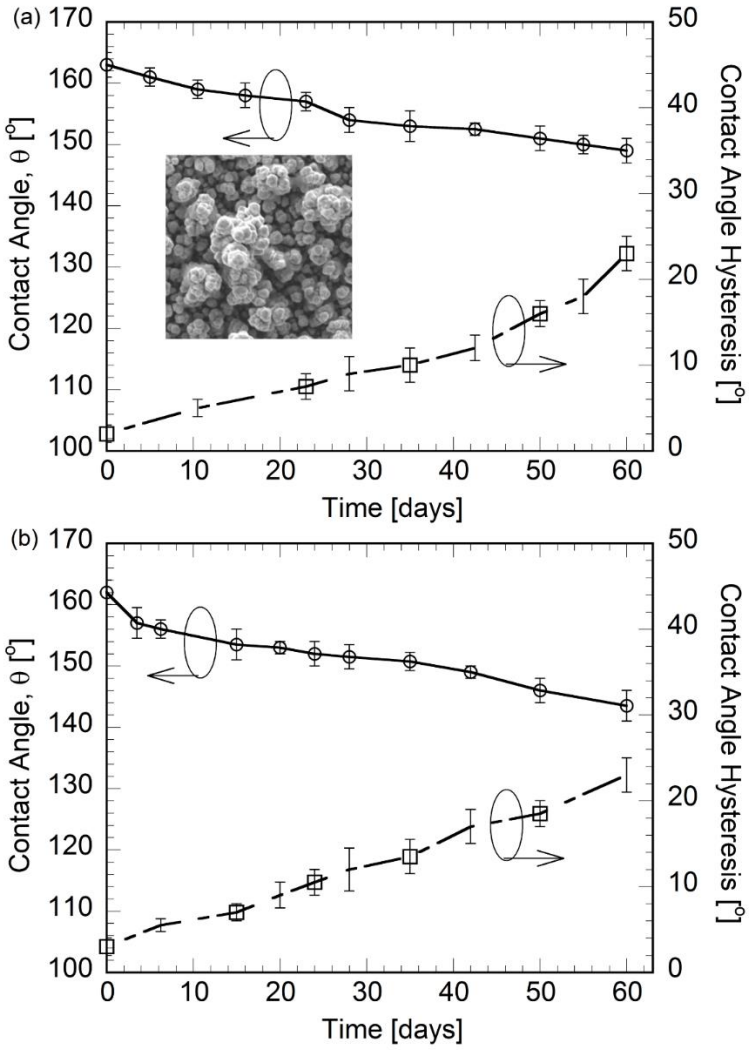

Figure 19. Contact angle and contact angle hysteresis for superhydrophobic copper surfaces immersed in (a) static deionized water and (b) simulated deionized water flow equivalent to 11 kmph. The inset in (a) is the SEM micrograph of the surface after 60 days of static immersion, confirming the durability of the coating morphology.

It can be observed that the rate of loss of slippery Cassie nature and reduction of contact angle is higher when sample is submerged in flowing water conditions in comparison to the static water. It implies that the flow affects the entrapped air in the cavities on a superhydrophobic surface and it is lost to the surrounding bulk water at a higher rate. At the end of the 60-day testing, the contact angle reduced to 143 ± 2^{o} and the hysteresis increased to 24^{0} (Figure 19b). However, the sample

was completely dry when removed from water, and the morphology was largely unchanged similar to the micrograph in the inset in Figure 19a. In addition, a plastron layer could also be observed for the developed superhydrophobic sample after being submerged for 60 days under flow conditions. This suggests that even though the contact angle degradation is slightly more (by about 6^0 at the end of 60 days) compared to immersion in static water (Figure 19a), hydrophobicity is preserved even after sustained flow conditions for 60 days.

4.2.7 Rejuvenation of slippery superhydrophobic nature

As seen in Figure 19, the superhydrophobicity of the copper samples degraded slightly upon prolonged exposure to water for 60 days; however, the morphology of the coating was largely unaffected by the water exposure. This suggests that the superhydrophobic characteristics may be restored to the original level with appropriate chemical treatment. To rejuvenate the superhydrophobic properties, the coating samples were re-immersed in a stearic acid solution, as used previously for generation of the original coatings, for 24 hours. The contact angle and roll-off angle were measured on the samples following the rejuvenation treatment. After retreatment, surface behaved similar to a newly prepared superhydrophobic surface and demonstrated similar wetting properties. Figure 20 shows the contact angle and roll-off angle measurements on a sample prior to (Figure 20a) and after (Figure 20b) treatment. It was found that re-treatment of the coating restored the contact angle, from 143±2° to 160±3°, as shown in Figure 20a.

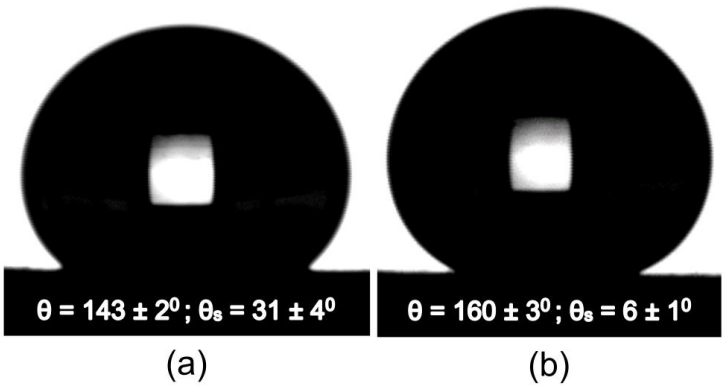

Figure 20. Equivalent droplet shape and contact angle for (a) superhydrophobic copper surface after immersion in flowing water for 60 days, and (b) after coating rejuvenation in stearic acid solution.

Water droplet rolled off the almost horizontal surface and roll-off angle was measured to be about 6^0 on this rejuvenated superhydrophobic surface. This easy regeneration of superhydrophobic nature on the prepared coatings makes the prepared surfaces suitable for the application in practical flow systems such as heat exchangers, ships and microfluidic devices etc.

This work describes the fabrication and testing of electrodeposition based, inherent copper superhydrophobic coatings. Effects of processing parameters such as deposition overpotential on wetting and morphology of coating surface was presented and discussed. Growth of multiscale fractal morphology lead to the superhydrophobic nature of coatings at high overpotentials. Mechanical and immersion durability of the prepared coatings was demonstrated through various tests based on ASTM standards. Furthermore, results of mechanical tests were represented based on unified energy parameters, combining the effects of relevant test parameters. Presented unified representation would also enable a consistent durability comparison for coatings fabricated through different techniques and processing conditions. In addition, excellent mechanical and immersion durability of the developed coatings would inspire the application of similar fabrication technique into the development of durable superhydrophobic coatings on other materials and will be considered in future studies.

4.3. Conclusions

An electrodeposition based process was used to generate superhydrophobic coating inherently on a copper substrate. The coatings exhibited stable, multiscale fractal, cauliflower shaped morphology, which were further modified by an inexpensive stearic acid treatment to achieve superhydrophobicity. The effect of processing parameters on the morphology and wettability were described, and the coatings were shown to have a contact angle of 162 ± 3^0 and roll-off angle of about 3^0 for an overpotential of 1.1V. Systematic studies were performed to evaluate the chemical composition, growth mechanism, mechanical abrasion stability, corrosion resistance, self-cleaning effect, air-exposure durability, under-water durability, and durability under flow conditions of the optimal superhydrophobic surfaces. Results for shear abrasion and falling sand abrasion tests were described based on frictional energy and sand impact energy per unit area, respectively. These representations combine the effects of the pertinent test parameters such as sandpaper grit size,

abrasion distance, load, height of falling sand etc. and provide a unified way to compare the mechanical durability of superhydrophobic coatings measured under different conditions.

The superhydrophobic copper coatings showed excellent durability, mechanical and underwater stability, corrosion resistance and self-cleaning effect. When submerged in static or flowing water, it was observed that beyond a certain time, the contact angle decreases and the roll-off angle increases, due to loss of entrapped air to the surrounding water. The rate of loss of entrapped air was observed to be higher for a sample submerged in flowing water. This study also describes a facile and cost-effective technique for the re-generation of slippery superhydrophobic nature on the surfaces after prolonged water exposure. This low-cost, facile process can be used to develop large scale, durable superhydrophobic coatings with controllable wettability for a range of practical applications.

Chapter 5. Fabrication and Characterization of Durable Zinc Based Superhydrophobic Coatings

Zinc coatings are widely used in the galvanization industry to improve the corrosion resistance of steel structures. Generally, an additional decorative hexavalent chrome layer is deposited for corrosion protection, which leads to carcinogenic chrome emissions. In this work, we present an electrodeposition based approach to fabricate superhydrophobic zinc coatings, that eliminate the need for the additional chrome layer while enhancing the corrosion resistance of the zinc coating by about one order of magnitude. Through electrodeposition in a highly conductive electrolyte, a multiscale needle and branch-shaped fractal morphology was obtained in the coatings, which were treated with stearic acid to obtain extreme water repellency in the prepared coatings, with contact angle of more than 160° and roll off angle of about 4–7°. Detailed microstructural and mechanical characterization studies are presented on the fabricated coatings under different processing conditions to demonstrate their durability, stability, longevity, and corrosion resistance. The presented process can be scaled to larger durable non-wetting coatings for diverse applications.

5.1. Introduction

Zinc has its primary application in the galvanization industry to protect steel structures from corrosion and about 80% of the total reported zinc consumed was used in galvanizing in 2015.[32] However, industrial application of zinc coating generally requires an additional hexavalent chrome coating for strength, decoration and to further prevent corrosion. However, chrome electroplating and anodizing is one of the largest source of carcinogenic chromium pollution in the U.S. and environmental protection agency (EPA) regulations have aimed at eliminating the use of hexavalent chromium in electrodeposition.[33] It has been reported by several researchers that the application of superhydrophobic coating enhances the anti-corrosion properties of a particular substrate.[34,7] Inspired by the lotus leaf in nature, superhydrophobic surfaces exhibit high water contact angles of more than 150°, a small roll-off angle and contact angle hysteresis, generally less than 10°, and demonstrate extremely low affinity towards water.[47] Owing to the improved corrosion resistance and non-wetting properties, application of a durable superhydrophobic zinc coating offers significant opportunities for eliminating the need for hexavalent chrome coating.

Other major potential applications of superhydrophobic surfaces as described in previous chapters, have inspired significant research into superhydrophobic surfaces over the last decade. Although several developments have been made in the processes and materials to fabricate superhydrophobic surfaces, industrial viability of these surfaces remain limited. This can primarily be attributed to the poor mechanical strength, abrasion resistance, and durability of the coatings under submerged conditions. Mechanical abrasion damages the multiscale structure of coatings, leading to the loss of their superhydrophobic nature. Moreover, under submerged conditions, the loss of entrapped air within the multiscale asperities to the surrounding water gradually leads to the wetting transition from Cassie state[9] to pinned Wenzel state[8] with apparent loss of superhydrophobic properties of the coatings.[70-72] This phenomenon is particularly severe and the rate of loss of entrapped air is increased for a superhydrophobic surface submerged in flowing water, leading to significantly reduced durability of such coatings. Even though practical applications of superhydrophobic surfaces in marine environment, heat exchangers and other thermal-fluid applications, would require them to be in contact with steady as well as flowing water for significantly longer durations, studies are rather limited in performing extensive durability studies in such environments, and only a few studies report the durability of superhydrophobic coatings in submerged conditions.[30,73] This suggests the need for a consistent and extensive testing methodology to study the mechanical stability and under-water durability of superhydrophobic coatings in steady and flowing water conditions for longer durations and the development of mechanically stable and durable coatings which can sustain superhydrophobicity for practical durations in such conditions.

Several techniques such as chemical vapor deposition[90], solution-immersion[91], etching[92], magnetron sputtering[93], and electrodeposition[94-96] have been used to develop zinc based superhydrophobic surfaces. However, the associated special processing conditions, cost, and time, limit the industrial scalability of some of the reported processes. Due to low cost, uniform deposition capability, and scalability, electrodeposition is considered as one of the most effective technique for large scale generation of superhydrophobic surfaces.[35,85] Zhang et al.[95] prepared superhydrophobic zinc coatings via electrodeposition followed by annealing and showed improved anti-corrosion property for superhydrophobic coating. Ying et al.[94] deposited superhydrophobic ZnO coatings on ITO-glass substrate. Zhang et al.[96] fabricated zinc superhydrophobic coatings through ionic liquid followed by polypropylene treatment. However, none of these studies reported

the mechanical strength, abrasion resistance, and under-water durability of the zinc based superhydrophobic coatings.

It is evident from the foregoing discussion that most of the zinc based superhydrophobic coatings developed to date have limited practical viability due to poor mechanical strength and durability. To overcome these limitations, the present work presents a cost-effective and scalable process based on electrodeposition to fabricate robust and durable zinc/zinc oxide superhydrophobic coatings on zinc substrates. Electrodeposition through a zinc acetate electrolyte leads to formation of needle-shaped multiscale deposits on a zinc substrate. The electrodeposited samples are then treated with stearic acid to reduce the surface energy and achieve superhydrophobicity. Contact angles (θ) and roll-off or sliding angles (θ_s) on as-prepared zinc coatings range from 156–166° and 4–7°, respectively. A comprehensive study of the effect of deposition potential and deposition time on the morphology and wettability is presented and discussed. Furthermore, systematic studies to evaluate the chemical composition, growth mechanism, mechanical abrasion stability, corrosion resistance, air-exposure durability, under water durability, and durability under flow conditions of the prepared superhydrophobic surfaces, are described and performed. Results of mechanical tests are presented in terms of combined energy parameter encapsulating the effects of various operating conditions such as load, abrasion distance and abrading surface. This representation enables the comparison of mechanical durability of superhydrophobic coatings on various materials reported in the literature with the as-prepared zinc-based superhydrophobic coatings in this study.

The chapter presents the analysis and discussion of various results such as morphology, wettability, corrosion resistance, and durability of zinc-based superhydrophobic surfaces fabricated as described in Section 2.4.

5.2. Results and Discussion

5.2.1. SEM morphology and wetting characterization

5.2.1.1 Influence of deposition time

The effects of deposition time on morphology and wetting properties of zinc/zinc oxide deposits were comprehensively studied. Scanning electron micrographs, respective equivalent droplet shapes, and static contact angle values are shown in Figure 21 for the samples deposited at a deposition potential of 1.3 V against a Ag/AgCl reference electrode, for deposition times ranging

from 100 s to 1100 s, with an increment of 200 s between successive deposits. As observed from deposit morphologies (Figures 21a–f), randomly distributed, branch and needle-shaped structures at multiple length scales are obtained for the considered deposition times. The inherent presence of progressively smaller needle-shaped asperity elements on top of larger base branch-shaped asperity structures as seen in the SEM micrographs in Figure 21, implies the fractal nature of the coatings prepared at various deposition times. With similar asperity features at various length scales, it is evident that the multiscale nature of deposit is nearly independent of deposition time for the fabricated zinc based coatings. However, size of branch and needle-shaped features tends to increase with the deposition time. The presence of multiscale asperity structure and fractal nature of coatings at all the considered deposition times can be attributed to the high conductivity of the electrolyte solution due to the presence of high KCl concentration.

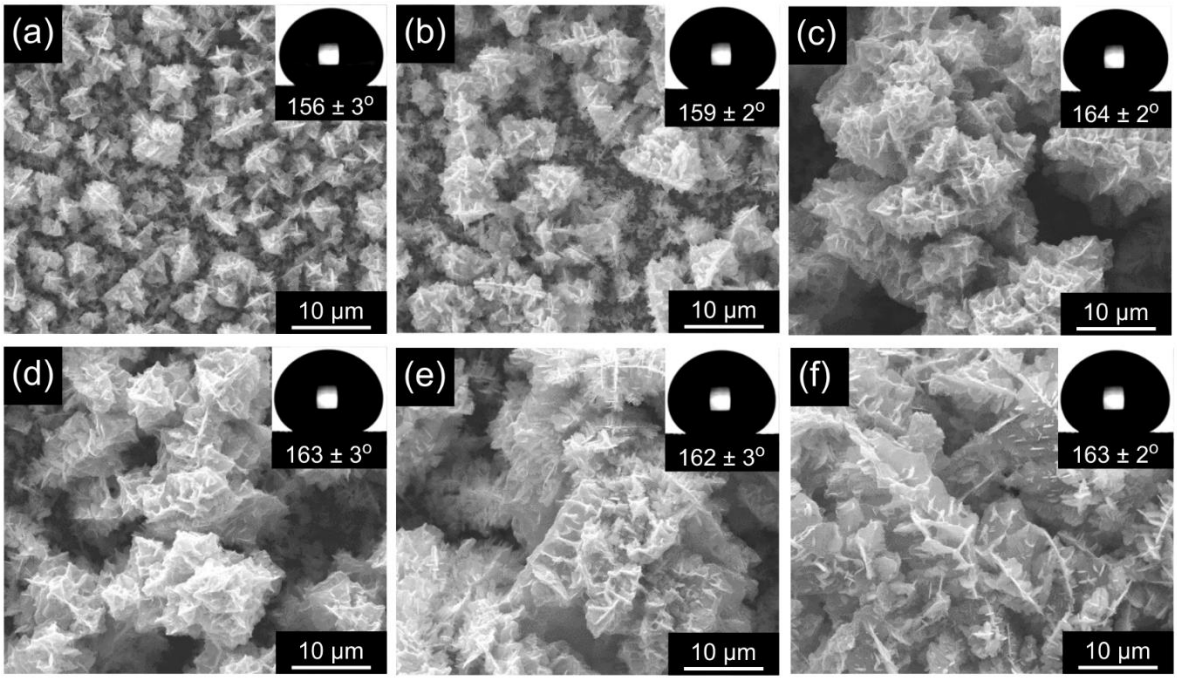

Figure 21. SEM Morphologies and water contact angles for the zinc based samples deposited at 1.3 V vs Ag/AgCl reference electrode for (a) 100 s, (b) 300 s, (c) 500 s, (d) 700 s, (e) 900 s, (f) 1100 s; Branch and needle-shaped asperities at multiple scales; Respective representative water droplet and contact angles are displayed in the insets.

Static contact angles (θ) of 156–164° are observed for the as-prepared zinc based coatings (Figure 21), with superhydrophobic properties being evident for these deposits, deposited for

various deposition times. Presence of asperities at multiple scales and low surface energy due to stearic acid treatment ensures the superhydrophobicity for the fabricated samples. Additionally, wetting properties are observed to be weakly dependent on the deposition time, which can be attributed to the presence and growth of multiscale fractal morphologies throughout the considered deposition time range.

5.2.1.2 Influence of the deposition potential

Effects of deposition potential on morphology and wetting properties of zinc/zinc oxide deposits were also studied by carrying out electrodeposition at potentials ranging from 1.1 V to 1.5 V against Ag/AgCl reference electrode. Deposition times were optimized to obtain coating thickness of about 25 μm for deposition at various considered potentials. Scanning electron micrographs, respective equivalent droplet shapes, and static contact angles for the fabricated samples are shown in Figure 22. Similar to the morphologies for the samples fabricated at 1.3 V, a combination of branch and needle shaped morphology is obtained for samples deposited at different potentials (Figures 22a-d). As evident from the presence of progressively smaller needle-shaped asperities on top of larger base branched asperity structures, multiscale fractal deposit morphologies were obtained for various considered deposition potentials. High ionic concentration of the electrolyte solution ensures these multiscale morphologies for the considered range of deposition potentials. Moreover, multiscale morphologies combined with low surface energies due to stearic acid treatment leads to stable Cassie state and superhydrophobicity, as evident from high static water contact angles (θ) ranging from 162–166° for as-prepared coatings deposited at the considered range of deposition potentials. Growth of fractal deposit structures at all the considered deposition potentials leads to the superhydrophobic nature of the as-prepared surfaces irrespective of the deposition potential.

In order to study the durability and sustained performance of the superhydrophobic coatings, surfaces prepared with a potential of 1.3 V against Ag/AgCl reference electrode for 500 s, were considered for further studies on dynamic wettability, mechanical durability, water immersion, corrosion and other characterizations, as discussed in this and the following subsections.

The dynamic wetting nature of the superhydrophobic zinc coatings fabricated at a potential of 1.3 V for 500 s was further evaluated under various dynamic conditions in terms of droplet sliding

or roll-off angle (θ_s), contact angle hysteresis on the coated surface, and dynamic behavior of a single water droplet impact.

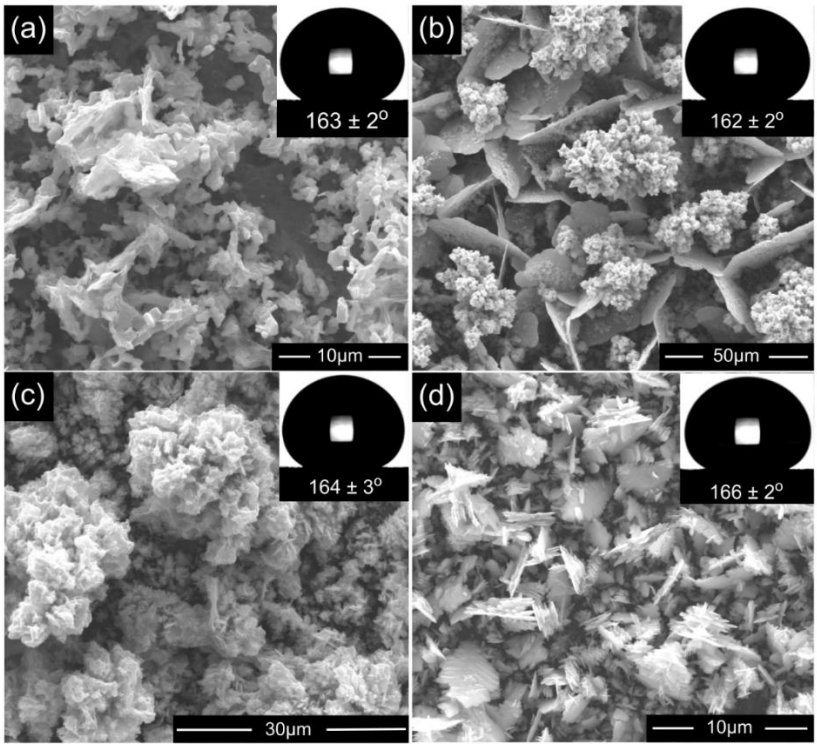

Figure 22. SEM Morphologies and water contact angles for the zinc based samples prepared at potentials of (a) 1.1 V, (b) 1.2 V, (c) 1.4 V, and (d) 1.5 V against Ag/AgCl reference electrode; Branched and needle-shaped asperities at multiple scales; Respective representative water droplet and contact angles are displayed in the insets.

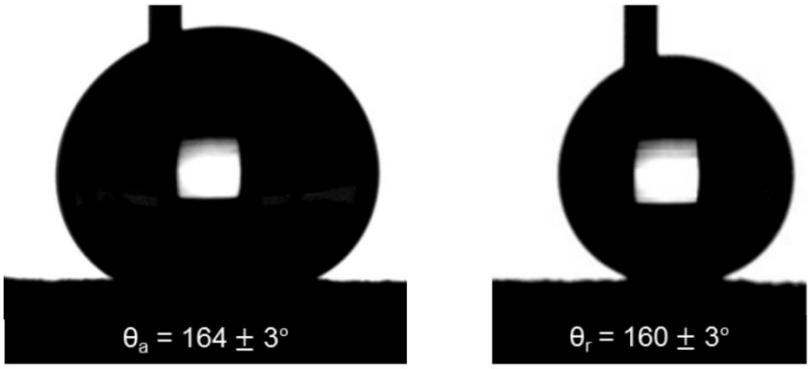

Figure 23. Dynamic contact angles with representative water droplet shapes on zinc based superhydrophobic surface: (a) Advancing contact angle (θ_a) and (b) Receding contact angle (θ_r).

A 10µl water droplet placed on the sample rolled off a nearly horizontal surface with a roll off angle of about 5°, demonstrating the excellent water-repellency of the surface. The dynamic wetting property of the prepared superhydrophobic zinc samples was further characterized in terms of the contact angle hysteresis through the volume changing sessile droplet method, as described in Section 2.6.

Advancing and receding contact angles were measured by progressively increasing and reducing the volume of water of a droplet placed on the coated surface, respectively, and analyzing the observed droplet shapes. Representative advancing and receding droplet shapes and contact angles from the experiments are shown in Figures 23a and 23b, respectively. Based on the measured advancing and receding contact angles, a very small contact angle hysteresis $(\theta_a - \theta_r)$ of about 4° is evaluated. Moreover, the dynamic behavior of impinging water droplets on the considered superhydrophobic sample was captured using a high-speed camera. A 10µl water droplet, dropped from a height of 4 cm bounced off the coated surface several times, before sliding off as shown by successive snapshots in Figure 24, where the time interval between two successive snapshots is 0.67 s. This small roll-off angle combined with a contact angle hysteresis of less than 10° demonstrate the strong non-wetting nature of the fabricated superhydrophobic zinc coatings under dynamic conditions.

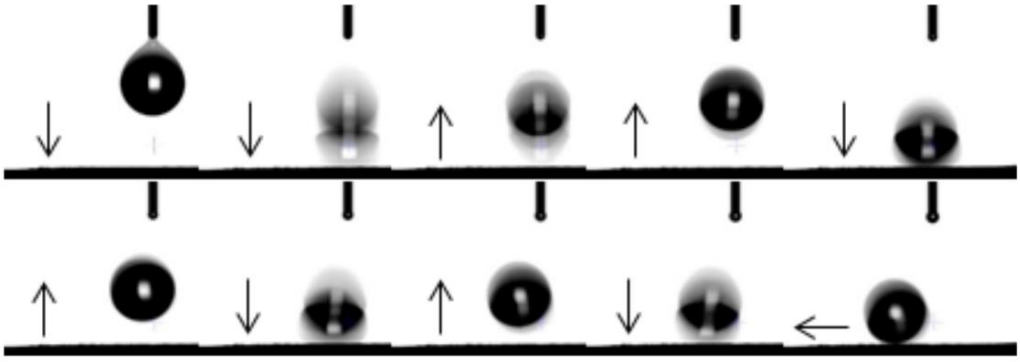

Figure 24. Successive snapshots of a water droplet dropped on a superhydrophobic sample with arrows indicating the direction of its instantaneous movement; time gap between each snapshot is 0.067 s.

5.2.2. Elemental analysis of superhydrophobic samples

Energy dispersion spectroscopy (EDS) analysis of the zinc based superhydrophobic samples fabricated at 1.3 V was carried out through FEI Quanta 600 scanning electron microscope (SEM)

to estimate the elemental composition of the prepared coatings and to study the effect of stearic acid treatment on the electrodeposited surfaces. Figure 25 shows the EDS spectra for (a) a zinc sample without stearic acid treatment and (b) a treated superhydrophobic zinc sample. Untreated electrodeposited zinc sample is primarily composed of Zn and O elements (Figure 5a), where the presence of oxygen elements can be attributed to the oxidation of coated surface. For coatings treated with stearic acid, presence of additional carbon element is observed on the surface in Figure 25b. Figure 25 also presents the normalized mass percent of respective elements on untreated and treated samples, based on the EDS spectra. Treatment of electrodeposited coatings with stearic acid solution leads to the formation of zinc stearate on considered zinc based substrates[74], as described by the equation: $Zn^{2+} + 2CH_3(CH_2)_{16}COOH \rightarrow Zn[CH_3(CH_2)_{16}COO]_2 + 2H^+$.

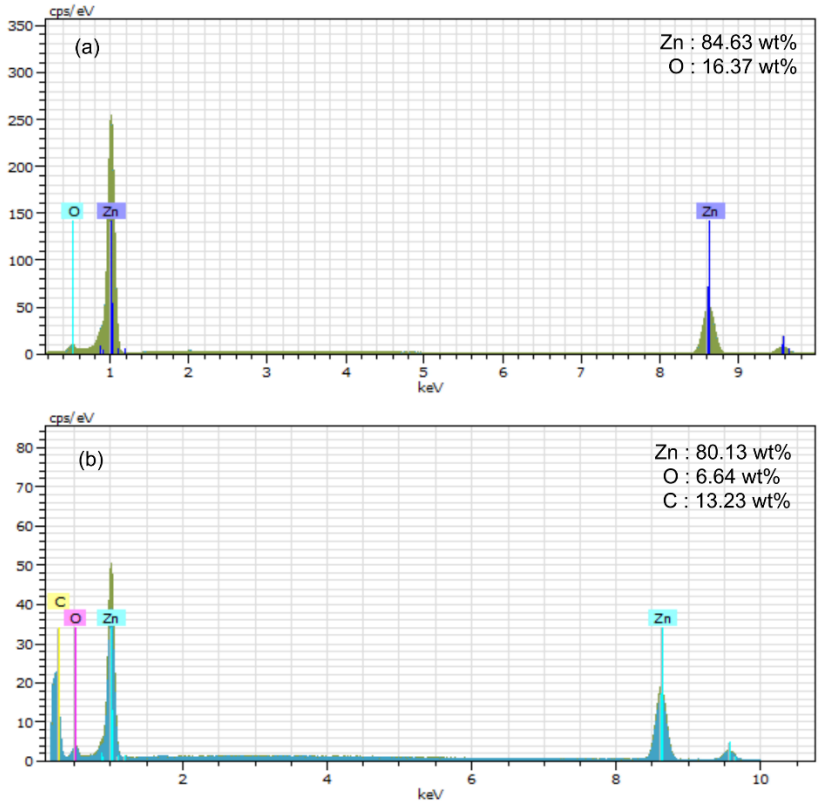

Figure 25. EDS spectra for (a) unmodified deposited zinc sample, (b) stearic acid modified superhydrophobic zinc sample.

5.2.3 Anti-corrosion property of superhydrophobic surfaces

Corrosion properties of the multiscale superhydrophobic coatings fabricated at 1.3 V against a Ag/AgCl reference electrode for 500 s, were studied by evaluating their potentiodynamic

polarization plots in 3.5 wt% NaCl solution, as described in Section 2.8. Based on the measured data, Tafel extrapolation was used to estimate the quantitative corrosion parameters. The measured potentiodynamic polarization curves for base and superhydrophobic zinc samples are shown in Figure 26, which are utilized to derive the corrosion potential (E_{corr}), corrosion current density (I_{corr}), and polarization resistance (R) as summarized in Table 2.

Table 2. Corrosion parameters for base zinc and superhydrophobic zinc in 3.5 wt% NaCl solution

Material	E_{corr} [V]	I_{corr} [$\mu A/cm^2$]	Corrosion resistance [kΩ]	Corrosion rate [mm/year]
Base Zinc	–0.938	520	0.055	15.584
Superhydrophobic Zinc	–0.965	17.6	1.31	0.52

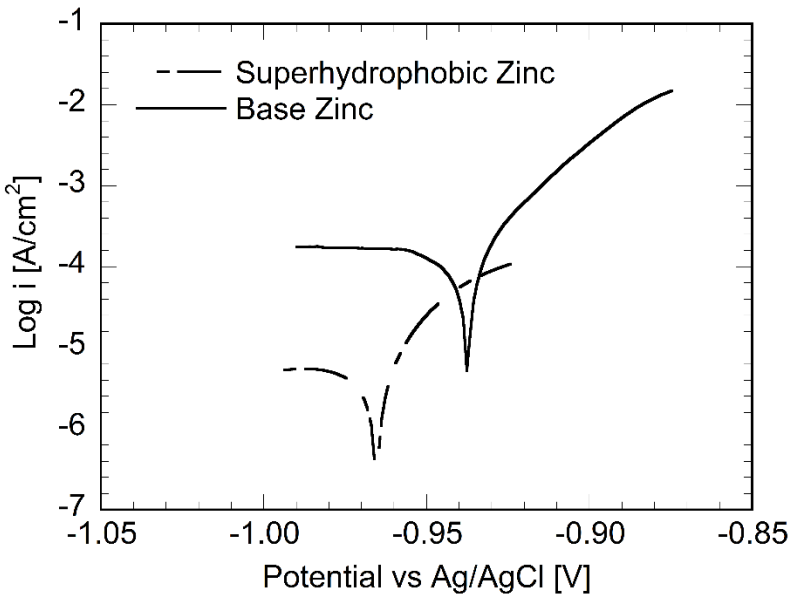

Figure 26. Potentiodynamic polarization curves for superhydrophobic and base zinc samples in 3.5 wt% NaCl solution.

In general, a higher corrosion potential and a lower current density correspond to a better corrosion resistance.[74,40] For the prepared superhydrophobic zinc coatings, a slight reduction in

E_{corr}, but a significant reduction in I_{corr} by more than one order of magnitude are observed, in comparison to an uncoated zinc substrate. This leads to a considerably higher polarization resistance of the superhydrophobic zinc coating relative to the bare zinc substrate, as listed in Table 2, and demonstrates the significantly improved anti-corrosion properties of the superhydrophobic zinc coating.

The improved anti-corrosive nature of the superhydrophobic surfaces can be explained by the presence of a stable Cassie state, which ensures the trapping of air within the roughness features of the multiscale coating surface. The presence of trapped air presents a cushion effect which avoids the contact of the surface region with NaCl solution.[40] As corrosion is a surface phenomenon, reduced contact of the surface with the salt solution leads to reduced corrosion rate.

5.2.4 Mechanical durability of the superhydrophobic surfaces

A primary factor limiting the use of superhydrophobic surfaces in practical applications is the lack of mechanical strength and robustness.[41] In conventional coatings, this limitation is particularly severe due to delamination at the interface between the dissimilar coating and substrate materials, which leads to the loss of superhydrophobicity of the surface. The method presented in this paper generates similar material based superhydrophobic surfaces inherently on the zinc substrate using electrodeposition, thereby eliminating the interface that's often the weak link in mechanical durability. Mechanical durability of the as-prepared superhydrophobic coatings in this study was extensively characterized using shear abrasion[25-29] and falling sand abrasion tests[86,87].

Figure 27a shows a schematic of the shear abrasion test derived from ASTM D4060[88], in which the superhydrophobic surfaces were dragged on a 1000 grit sandpaper, under a load of 3 kPa, for a distance of 200 cm, at a speed of 1 cm/s. The changes in wettability of samples were assessed by measuring the static and dynamic contact angles as a function of abrasion length. Mechanical abrasion leads to a gradual loss of non-wetting nature through a decrease in the contact angle and increase in contact angle hysteresis. In order to analyze the combined effects of abrasion surface roughness (sand paper grit size), pressure load, and abrasion distance in a unified manner, a parameter based on the frictional energy dissipation was used. The frictional energy parameter was defined as the product of three terms — the ratio of coefficient of friction of considered sandpaper and that of a 1000 grit sandpaper for a particular sample [μ/μ(1000)], the applied pressure, and the abrasion distance—and signifies the frictional energy per unit area with respect to abrasion on a

1000 grit sandpaper. The static coefficient of friction used in calculating the friction energy parameter was estimated as the tangent of the angle at which the substrate slips off a sandpaper surface. The use of the frictional energy parameter also serves to compare the obtained results with those reported in the literature[25-29] for the different grit sizes, pressure and abrasion distance in a common manner.

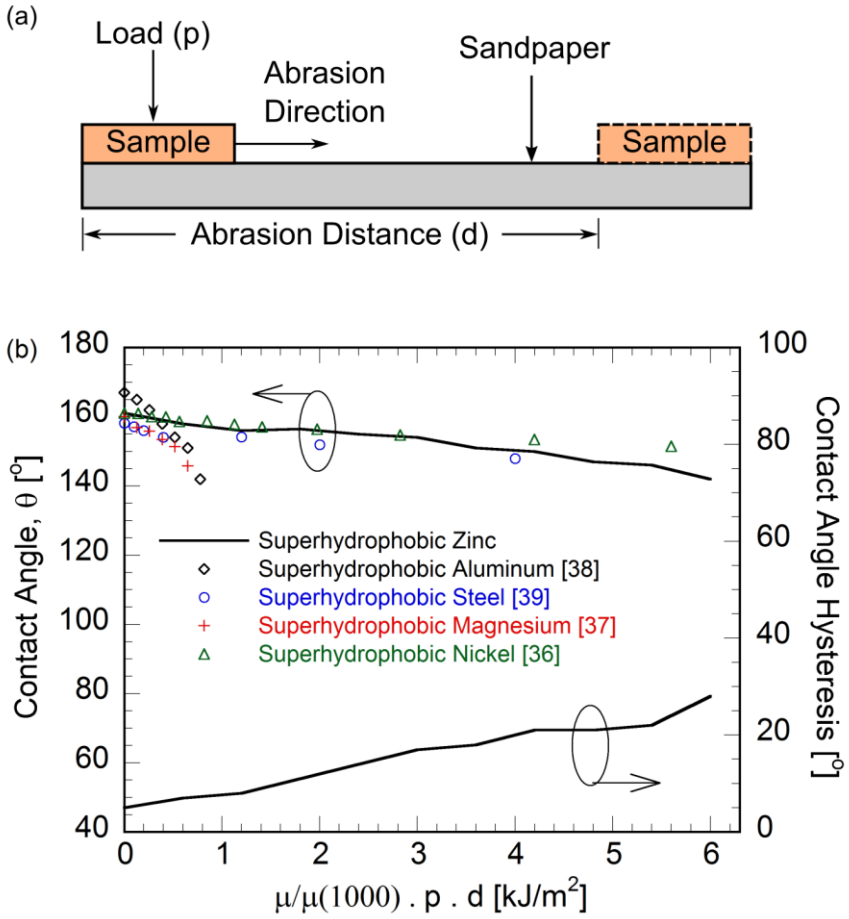

Figure 27. (a) Schematic of shear abrasion test setup and (b) variation of the contact angle and contact angle hysteresis for superhydrophobic zinc surface with relative frictional energy per unit area, in comparison to several recently reported superhydrophobic coatings on different metallic substrates.

Figure 27b presents the measured contact angle on the superhydrophobic zinc samples in this study as function of the friction energy parameter. It is seen that the contact angle decreases and the contact angle hysteresis increases slightly with the parameters contributing to an increased frictional energy dissipation. After a 200-cm abrasion distance (corresponding to a frictional

energy parameter of about 6 in Figure 27b), some loss in superhydrophobicity was observed resulting in a reduced contact angle of 142 ± 3° and increased hysteresis of about 28°. However, the sample remained superhydrophobic and was not wetted by water. Also presented in the same figure are the shear abrasion test data on several superhydrophobic coatings recently reported in the literature at different abrasion conditions, expressed in terms of the friction energy parameter.[25-29] These data are compared against the superhydrophobic zinc coating in the present work. The coatings on Aluminum[27] and Magnesium[26] are seen to lose their superhydrophobicity within about 1 kJ/m^2 and the coatings on steel[28] are reported to withstand up to 4 kJ/m^2. Though the nickel-based superhydrophobic coating developed by Su and Yao[25] is seen to maintain its contact angle to 5.5 kJ/m^2, the coating was reported to have an increased roll-off angle of about 30° during the shear abrasion test, indicating that the superhydrophobicity was lost quickly. In contrast, it is seen that the superhydrophobic zinc coatings in the present work exhibit mechanical abrasion resistance similar to some of the recently developed, robust superhydrophobic surfaces on other materials and maintain good superhydrophobicity over much higher levels of abrasion energy, up to 6 kJ/m^2, than the other superhydrophobic surfaces. The presented facile and cost-effective fabrication process of zinc based superhydrophobic surface fabrication, leading to a mechanically durable coating, presents a better alternative to the conventional zinc coatings.

Mechanical durability of the prepared zinc based superhydrophobic surfaces was further evaluated by using the falling sand abrasion tests, based on ASTM D968[39], as shown schematically in the inset of Figure 28. Silicon carbide grains (100–250 μm in diameter) were impinged on the samples inclined at an angle of 45°, from a height of 20 cm at a rate of 0.25 kg/min. Up to 1000 gm of falling abrasive silicon carbide grains were on the samples were used to demonstrate the durability of the superhydrophobic zinc surfaces against impacting silicon carbide grains. Falling silicon carbide abrasive grains damage the coatings microstructures leading to a gradual loss of superhydrophobic nature of coating through decrease in contact angle and increase in contact angle hysteresis. Similar to shear abrasion tests, changes in the wetting properties of samples were assessed by measuring the static and dynamic contact angles with amount of abrasive grains.

For better physical understanding, the combined effects of drop height and considered mass of grains are presented in terms of potential energy of silicon carbide particles per unit impact area. Variation of contact angle and contact angle hysteresis are presented in Figure 28 as a function of

energy per unit impact area, for the fabricated zinc based superhydrophobic surfaces. The experiments were repeated 3 times and the data are presented in Figure 28 in terms of the mean and the error bars. It is seen that the contact angle decreases and the contact angle hysteresis increases slightly with abrasion, signifying some loss in superhydrophobicity, as expected. However, at the end of the aggressive falling sand abrasion test, the considered samples remained superhydrophobic, as evident from a contact angle of about 153.5° and hysteresis of about 13°. Note that these tests were conducted with 20–100 times the amount of abrasives compared to those used in the tests in the literature. In the conventional range of testing, therefore, which correspond to energy per unit impact area of less than 0.04 J/cm^2, there is insignificant change in the contact angle and hysteresis seen in Figure 28. The falling abrasive tests under the aggressive conditions, therefore, demonstrate a significantly enhanced durability of the superhydrophobic zinc coatings fabricated in the present study.

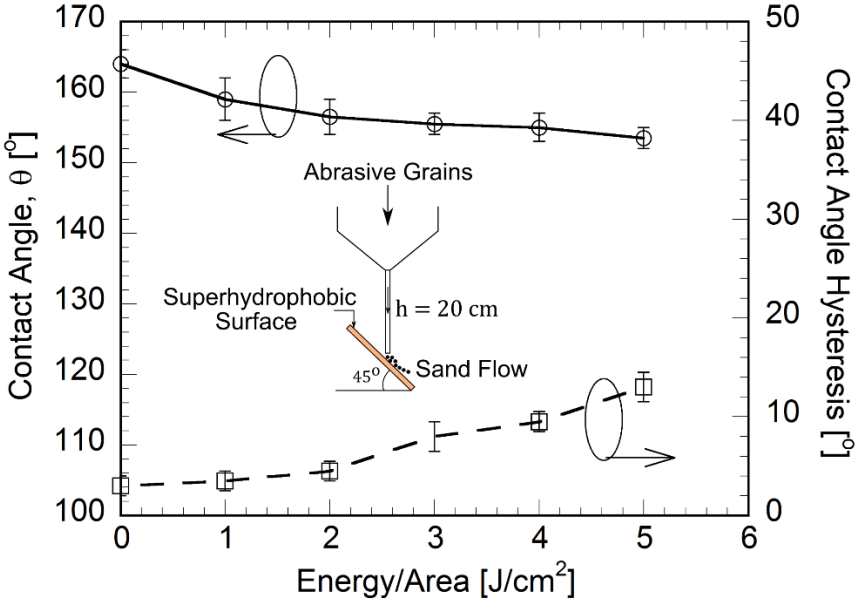

Figure 28. Variation of contact angle and contact angle hysteresis with impact energy per impact area for zinc based superhydrophobic surfaces subject to falling sand abrasion test. Inset figure shows a schematic of the falling sand abrasion test setup.

5.2.5 Durability of superhydrophobic surfaces under air exposure, water immersion and flow conditions

Wetting properties of the zinc based superhydrophobic coatings in this study were observed during air exposure for up to 6 months. No practical changes in the static contact angle (161°) and

contact angle hysteresis (5°) were observed during the exposure period, demonstrating the excellent superhydrophobic properties of the coatings under long duration air exposure.

Furthermore, practical applications of superhydrophobic surfaces in marine environment, rainy season, heat exchangers etc. require them to be in contact with water for long durations. However, trapped air within the multiscale roughness features of the superhydrophobic surface is known to dissolve into the surrounding water with time, leading to a transition from slippery Cassie state to pinned Wenzel state.[70] This phenomenon leads to the loss of superhydrophobic nature of the prepared coatings at a fast rate and limits the practical applicability of the superhydrophobic coatings.

Water immersion tests were conducted on the superhydrophobic zinc surfaces prepared in this study, under static and dynamic conditions. Immersion tests were conducted following the practices outlined by ASTM D870, standard practice for testing water resistance of coatings using water immersion.[89] In the static immersion tests, the superhydrophobic samples were immersed in deionized water for about 60 days, and changes in their wetting properties were measured at various time instants during the exposure. Figure 29a presents the contact angle and contact angle hysteresis measurements on the superhydrophobic samples during the 60-day static immersion test.

The variations in the measurements among the different samples are plotted in terms of the mean value and the error bar for each data point. It is seen that the contact angle decreases and the contact angle hysteresis increases with immersion time. After 60 days of water immersion, the contact angle of zinc based surface was reduced to 151° (from the initial value of 164°) and contact angle hysteresis was increased to 15°, which suggests the loss of some of the entrapped air to the bulk water. Furthermore, even after 60 days of immersion the zinc samples were able to maintain their superhydrophobic nature, demonstrating the excellent durability of the prepared superhydrophobic zinc surfaces even after prolonged water exposure in statically submerged conditions.

As flowing water is known to enhance the rate of loss of entrapped air from a superhydrophobic surface, durability of the zinc based superhydrophobic surface was also evaluated under flowing water conditions, as described in Section 2.9. The samples were immersed in flowing water for 60 days, with periodic removal during the testing for measurement of contact angles and contact angle hysteresis. Figure 29b shows the variation of the measured contact angles and contact angle

hysteresis with time during the dynamic water immersion testing. It can be observed that the rate of loss of superhydrophobic nature is higher when the sample is submerged in flowing water conditions, in comparison to a static water, as evident from higher rate of contact angle reduction for sample in flowing water condition. It implies that the flow affects the entrapped air in the cavities on a superhydrophobic surface and it is lost to the surrounding bulk water at a higher rate. At the end of the 60-day testing, the contact angle reduced to 143° and the hysteresis increased to 29° (Figure 29b). However, the sample was completely dry when removed from water suggesting that a high level of hydrophobicity is preserved even after sustained flow conditions for 60 days.

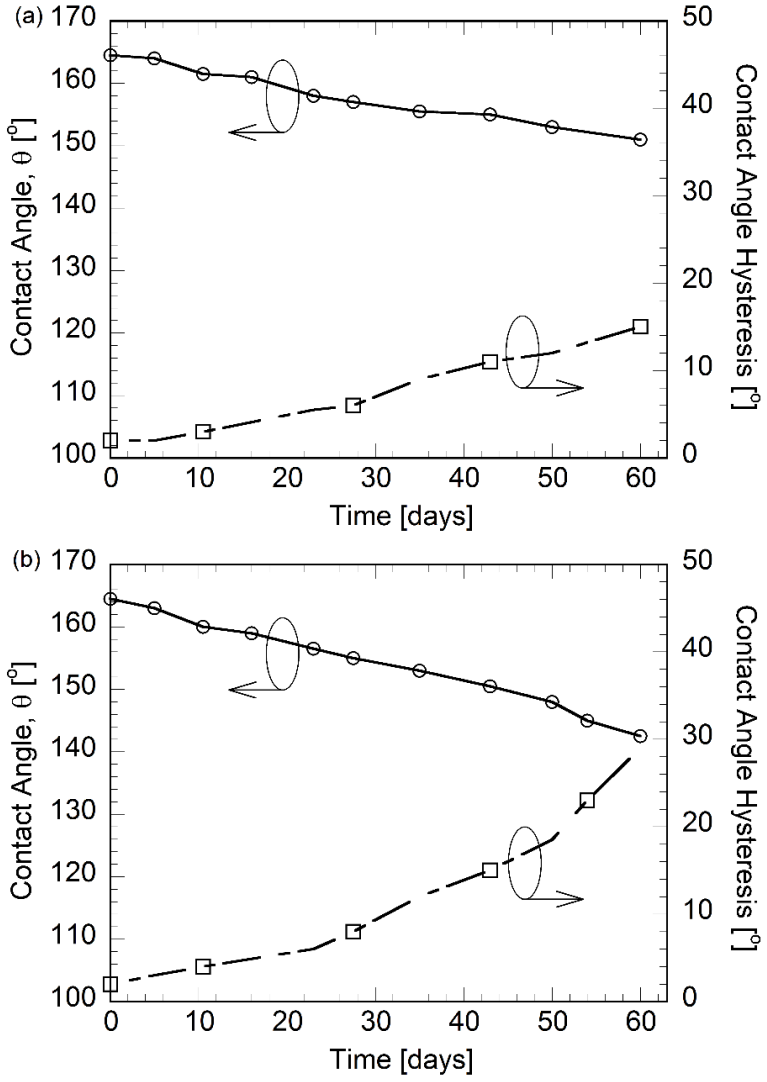

Figure 29. Contact angle and contact angle hysteresis for zinc based superhydrophobic surfaces immersed in (a) static deionized water and (b) simulated deionized water flow equivalent to 11 kmph.

This work reported in this chapter describes the fabrication and extensive characterization of superhydrophobic zinc coatings deposited inherently on zinc substrates. The excellent mechanical and immersion durability of the developed coatings inspires further development of the presented superhydrophobic coatings on different materials, which will be considered in future studies.

5.3. Conclusions

An electrodeposition based process was described to fabricate superhydrophobic coatings inherently on a zinc substrate. Through electrodeposition from zinc acetate electrolyte, stable zinc based deposits with multiscale needle and branch-shaped morphologies are obtained on zinc substrate. Deposited samples are modified by an inexpensive stearic acid to achieve superhydrophobicity. Effects of deposition potential and time on the morphology and wettability of coatings were studied and presented. As-prepared coatings demonstrated excellent superhydrophobicity with contact angles ranging from 156–166° and roll-off angles in the range of 4–7° for fabricated superhydrophobic coatings at various processing conditions. Systematic studies were performed to evaluate the chemical composition, growth mechanism, mechanical abrasion stability, corrosion resistance, air-exposure durability, under water durability, and durability under flow conditions of the prepared superhydrophobic surfaces. Results for shear abrasion and falling sand abrasion tests were described based on frictional energy and sand impact energy per unit area, respectively. These representations combine the effects of the pertinent test parameters such as sandpaper grit size, abrasion distance, load, height of falling sand etc. and provide a unified way to compare the mechanical durability of superhydrophobic coatings measured under different conditions.

The superhydrophobic zinc coatings showed excellent durability, mechanical and underwater stability, and corrosion resistance. When submerged in static or flowing water, it was observed that beyond a certain time, the contact angle decreases and the roll-off angle increases, due to loss of entrapped air to the surrounding water. The rate of loss of entrapped air was observed to be higher for a sample submerged in flowing water. This low-cost, facile process can be used to develop large scale, durable zinc based superhydrophobic coatings for practical applications.

Chapter 6. Fabrication and Fractal Description of Multiscale Copper Based Solar Selective Coatings

Photothermal conversion efficiency depends significantly on the selectivity of the surface carrying the heat transfer fluid in a concentrated solar power system. Base metal substrate is generally coated with a solar selective coating, which provides high solar absorptivity and low thermal emissivity. Material and microstructure of the coatings are the primary parameters for a solar selective coating, which define their optical properties. Present work describes the fabrication of inherent multiscale copper based solar selective coatings through electrodeposition and presents the effects of scale independent fractal parameters of coating surfaces on their optical properties, such as absorptance, emittance, and figure of merit (FOM). Coatings are characterized with fractal description based on Weierstrass-Mandelbrot (W-M) function, where the fractal parameters are uniquely determined from a power spectrum of the surface. Moreover, effects of heat treatment on optical properties were also quantified at various fractal levels for such coatings.

6.1. Introduction

The recent years have witnessed a significant ramping up of efforts towards efficient energy generation using renewable resources such as solar, wind etc. Concentrating solar power (CSP) generation is of significant interest amongst the various approaches used to harness solar energy.[97] One of the major advantages of CSP is the possibility of inexpensive and highly efficient energy storage in thermal form, which can provide electricity generation in the periods with no sunlight as well.[97,98] Power generation with CSP involves five major steps: (i) concentration: tracking and concentrating sunlight onto a solar receiver, (ii) absorption: incident solar energy on the receiver is converted to heat by an absorber, (iii) transfer: heat carried away from the absorber by a heat transfer fluid (HTF), (iv) generation: utilization of thermal energy for power generation in a heat engine, and (v) storage: excess heat stored in an efficient and cost-effective thermal energy storage (TES).

The goal of a thermal receiver in a CSP plant is to effectively absorb sunlight with minimal thermal loss. Therefore, improving the photothermal conversion efficiency of CSP systems is of considerable focus in recent studies.[2-4, 99-101] Photothermal conversion efficiency depends primarily on the selectivity of the surface carrying the HTF. An ideal absorber must exhibit high spectral

absorptivity (> 0.95) in the visible and near-infrared (IR) wavelengths (0.28 to 2.5 μm), where the bulk of the energy from the solar spectrum is concentrated, and low emittance (< 0.1) in the IR wavelengths (~2 – 20 μm), where the black body emission peaks. To achieve the desired optical properties, solar selective coatings are applied on the base metal substrates. Several solar selective coatings with different properties, materials and deposition techniques are reported in the literature. [2-4, 99-101] Material and microstructure are the primary parameters defining the optical properties of coatings and microstructures of the coatings are largely dependent upon the deposition process and parameters.[102] Hence, an extensive characterization of microstructure of solar selective coatings may provide an understanding of the effect of morphology on their optical properties, which would be of significant use in developing more efficient solar selective coatings.

In general, coatings developed through industrially scalable techniques such as electrodeposition, spray coating, dip coating etc., have random multiscale morphology.[102-104] Several researchers have characterized the optical properties of such coatings based on their roughness.[103-106] Through experimental studies, it is shown that the roughness of coatings is positively correlated with their effective solar absorptivity and thermal emissivity.[103-106] Additionally, coating surface roughness has also been modeled with Gaussian disorder by Kowaczeski et al, who estimated the optimum roughness parameters yielding the highest absorption enhancement.[107] However, it was indicated by Majumdar and Bhushan[51,16], that conventional roughness parameters are not unique to a surface and depend on the scan length and resolution of the measuring instrument. In addition, Kang et al also described that the standard surface parameters such as, roughness and slope are not sufficient descriptive of surface characteristics, as surface topography is non-stationary and multiscale, based on the analysis of machined surfaces depending on coated tool wear. As fractal parameters are suggested to be better surface descriptive parameters due to their invariance with length scale[108], the need of a scale independent fractal representation and estimation of optical properties based on the fractal parameters for the considered solar selective coatings, was realized.

Characterization of coatings based on fractal theories is extensively used by several researchers in the description of elastic-plastic contact[16,65], tribology[65], tool wear[108] etc., in the recent past. However, application of scale independent fractal theories in understanding the optical properties of solar selective coatings remain rather limited in literature. Recently, Barrera, et al. applied detrended fluctuation analysis (DFA) to SEM images of black Mo coatings on copper

substrate to study their fractal properties. Furthermore, correlation of fractal parameters with the optical properties demonstrated the increase of absorptivity and emissivity of coatings with growth of fractal nature of surface.[102] However, the EDS analysis reveals the presence of multiple elements such as Mo, Cu, O, on the coating surface and a variation in coating material composition is expected for coatings with different fractal dimensions, generated at different processing conditions. Hence due to this expected change in material composition between coatings, the results do not provide a stand-alone effect of fractal parameters on the optical properties of coatings. In addition, considered dip coating process to fabricate the black Mo coatings leads to the fractal dimensions only in a short range of 1.02-1.2.

It is evident from the foregoing discussion that the studies so far on understanding the effect of optical properties of coatings are based on the scale-dependent roughness parameters. Moreover, studies considering scale independent fractal parameters to study such properties are limited with coatings of multicomponent nature within a very small range of fractal dimensions. As with scalable processes such as electrodeposition, single material based solar selective coatings with a broader range of fractal dimensions can be generated, hence, to overcome the above limitations, the present work considers the fabrication of inherent copper based solar selective coatings through electrodeposition and presents the effects of scale independent fractal parameters on their optical properties, such as absorptance, emittance, and figure of merit (FOM). A 2-step electrodeposition technique, deposition at larger potential, followed by at a small potential for a short duration, as employed by Haghdoost and Pitchumani[35] into the development of superhydrophobic coatings, was considered in this study to fabricate stable multiscale coatings. Coatings were mathematically characterized based on the Weierstrass-Mandelbrot (W-M) function. Fractal parameters of coating surface are uniquely determined through the power spectrum of surface based on surface profile scan. Effects of applied deposition potential and heat treatment on the coating morphology, fractal parameters, and optical properties are studied and described in detail.

Various results such as optical characterizations, figure of merit, and effects of heat treatment on coating selectivity are described in this chapter, for copper based solar selective coatings fabricated, as described in Section 2.3.

6.2. Results and Discussion

6.2.1 Optical Characterization

The effects of applied overpotential on the optical properties of copper based solar selective coatings were comprehensively studied. Optical properties of the coatings fabricated at different overpotentials were measured as described in Section 2.10. Reflectance measurements on various coatings were performed through UV-vis-NIR spectrometer for wavelengths ranging from 280 to 2500 nm. Percentage reflectance variation with incident wavelength on base copper, copper sample deposited at 1.1 V, and copper sample deposited at 1.1 V followed by heat treatment at 260^{o} C for 1 hour, are shown in Figure 30. Overall reflectance percentage for deposited and heat treated samples is nearly zero in the visible region of spectrum. Furthermore, reflectance of deposited samples is significantly lower than the reflectance of base copper sample, implying high absorptivity of the deposited samples. Moreover, beyond the wavelength of about 550 nm, reflectance of heat treated sample is about 25-30% lower than non-heat treated deposited copper sample. The lower reflectance on heat treated electrodeposited copper sample can be attributed to the oxidation of copper coating to copper oxide.

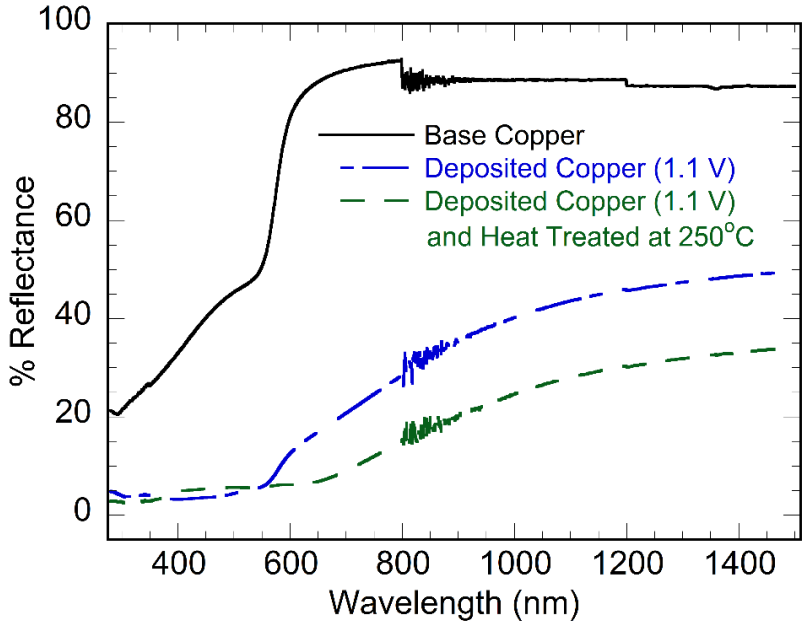

Figure 30. Reflectance spectra of copper samples deposited at 1.1 V and heat treated in comparison with bare copper substrate.

Effective solar absorptivity (α_{solar}) of the prepared coating surface is defined as the weighted fraction (by total power density) of the absorbed radiation to that incident on the surface and is given as[43]:

$$\alpha_{solar} = \frac{\int_{280\,nm}^{2500\,nm}\left(1 - R(\lambda)\right) E_{solar}(\lambda)\, d\lambda}{\int_{280\,nm}^{2500\,nm} E_{solar}(\lambda)\, d\lambda} \tag{3}$$

where, λ is the wavelength of the incident radiation, $R(\lambda)$ is the measured reflectance of the surface at a particular wavelength λ, and $E_{solar}(\lambda)$ is the normal spectral irradiance as a function of the wavelength, defined by the ISO standard 9845-1 (1992) for air mass (AM) 1.5. Effective solar absorptivity of fabricated samples was estimated based on measured reflectance and AM 1.5 solar spectra.

Effective solar absorptivity of prepared coatings with deposition overpotential is shown in Figure 31. Solar absorptivity of coatings does not follow a gradual increasing trend as that of fractal dimension with increasing overpotential. The solar absorptivity of coatings deposited at smaller overpotentials ranging from 0.3-0.7 V remains nearly the same. However, a significant enhancement in effective solar absorptivity is observed for coatings deposited beyond the overpotential of 0.9 V. Aggressive growth of morphological instabilities at high overpotentials leads to an improved light trapping within the coating. Highly aggressive fractal nature of coatings with cauliflower-shaped morphologies and fractal dimensions close to the physical maxima of 2, deposited beyond 0.9 V can be attributed to a significant increase in effective solar absorptivity. Aggressive multiscale features with smaller inter-asperity distance allows better light trapping within coating morphologies, leading to an increase solar absorptivity. However, larger inter-asperity distance for the coatings deposited at smaller overpotentials does not enable an effective light trapping within the asperity features, leading to lower solar absorptivity.

In addition, thermal emissivity of the coatings was measured at a temperature of 80℃, aimed at the estimation of figure of merit (FOM) as described by Ambrosini, et al.[42], and given as:

$$FOM\left(\frac{W}{cm^2}\right) = 60\alpha_{solar} - 5\left[\frac{\epsilon_{80^oC} + \epsilon_{2400\,nm}}{2}\right] \tag{4}$$

where, ϵ_{80^oC} is emittance at 80°C, $\epsilon_{2400\,nm}$ is emittance at 2400 nm. Constant 60 and 5 represent the energy flux incident on a central receiver and the energy flux emitted by a blackbody at 700℃,

respectively. Thus, FOM parameter helps in understanding the comparative performance of coatings at the temperature of 700°C.

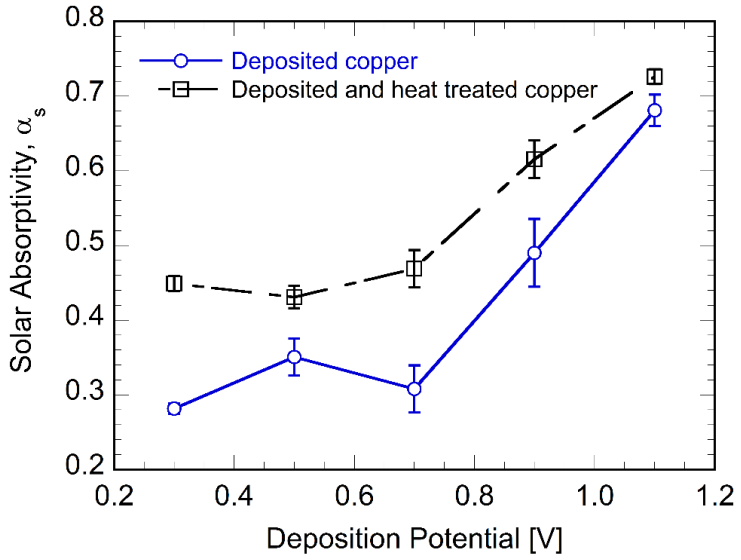

Figure 31. Variation of effective solar absorptivity for copper based deposited and heat treated samples at various deposition overpotentials ranging from 0.3 V to 1.1 V, showing the significant increase of solar absorptivity of coatings deposited at high overpotentials.

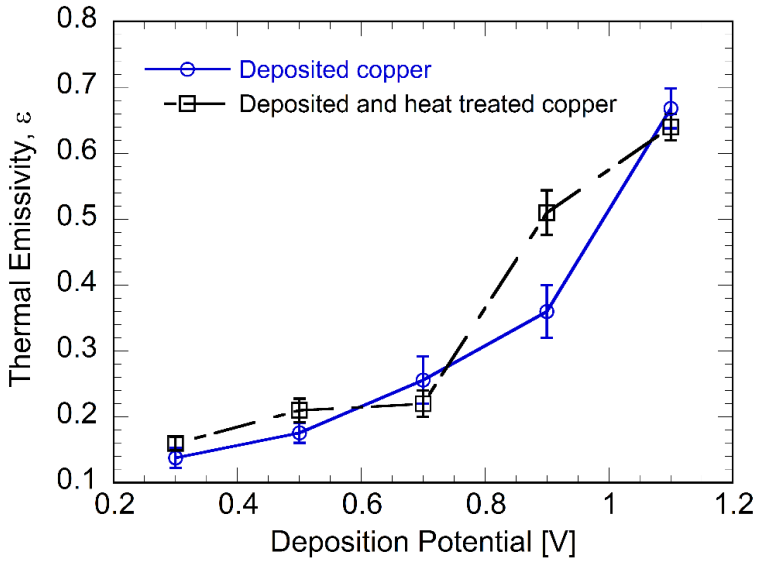

Figure 32. Thermal emissivity at 80° C for copper based deposited and heat treated samples at various deposition overpotentials ranging from 0.3 V to 1.1 V.

Variation of thermal emissivity at the temperature of 80°C, ϵ_{80^oC}, is plotted against deposition overpotential for the fabricated coatings in Figure 32. Thermal emissivity is observed to increase

gradually with deposition potential and fractal dimensions. This nature can be attributed to the increase of coating surface area due to an increase in morphological instabilities and multiscale nature of coatings with deposition overpotential. Higher available coating surface area allows higher amount of energy to emit in the infrared region, leading to a larger energy loss from the surface and increased thermal emittance of the fabricated copper coatings.

Variation of the figure of merit parameter for copper coatings against deposition overpotential is presented in Figure 33. FOM parameter is primarily governed by effective solar absorptivity, due to a large multiplier to solar absorptivity term as seen in Equation 4. Hence, coating figure of merit follows a trend very similar to the solar absorptivity as observed in Figure 31. Figure of merit of coatings deposited at overpotential of 0.7 V or lower, remains nearly the same. For coatings deposited at potentials beyond 0.9 V, a significant increase in solar absorptivity leads to the enhanced figure of merit. This high figure of merit may again be attributed to the aggressive fractal texturing at high overpotentials beyond 0.9 V leading to a significant light trapping within their morphological features.

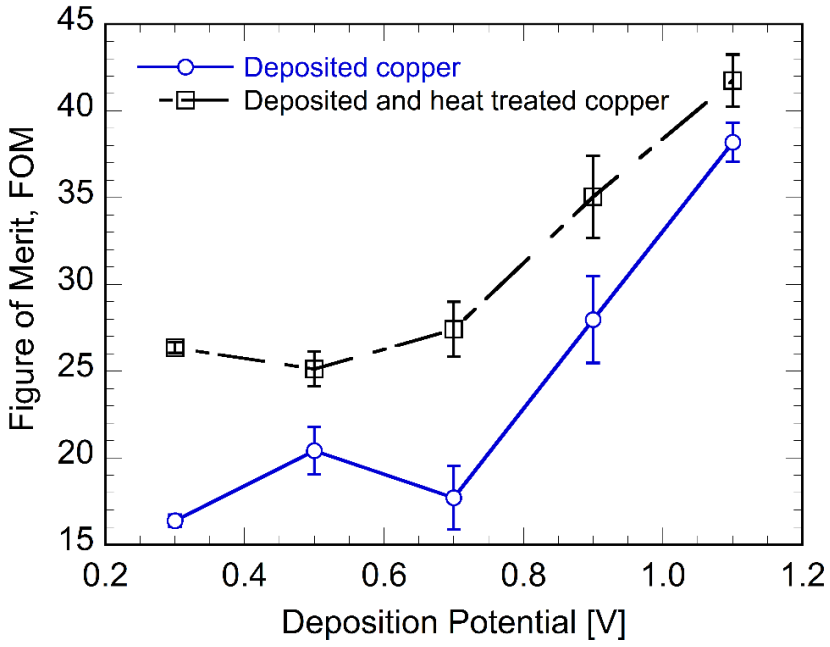

Figure 33. Figure of merit (FOM) for copper based deposited and heat treated samples at various deposition overpotentials ranging from 0.3 V to 1.1 V.

6.2.2 Effects of Heat Treatment

As-prepared copper based solar selective coatings were heat treated for 1 hour at 260ºC in air to study the coating stability the effects of heat treatment on various optical parameters as described in this study. Coating was observed to be physically stable at the end of heat treatment. Figures 31-33 also show the variation of effective solar absorptivity, thermal emissivity, and figure of merit of the coatings with respect to the deposition overpotential, respectively. For various fractal texturing levels of coatings, no significant variation between thermal emissivity values for heat treated deposits in comparison to the untreated deposits was observed. However, nearly 10-20% increase in effective solar absorptivity and figure of merit was observed for the coatings deposited at various deposition overpotentials and fractal texturing levels, with respect to the as-prepared without heat treated samples. As described by Ambrosini, et al., heat treatment leads to an increase in oxide layer thickness and reduction of surface roughness due to the minimization of surface energy, promoting diffusion.[42] Increase of oxide layer thickness leads positively affects effective solar absorptivity and reduction of surface roughness has negative effect on solar absorptivity. However, the observed increase in figure of merit due to heat treatment suggests that the oxide layer thickness increase is the most influential effect of the heat treatment. Based on these results, it can be suggested that the aggressive fractal texturing in combination with the heat treatment can lead to a significant improvement of figure of merit of a solar selective coating.

To summarize, this study focuses on understanding the impact of multiscale fractal texturing and heat treatment on optical properties of a solar selective coating. Performance of the coatings was compared based on solar absorptivity, thermal emissivity and figure of merit. As described by Ambrosini, et al.[42], figure of merit is based on the idea that improving solar absorptivity of coating is more beneficial for coating efficiency than reducing emissivity. This study provides a proof of concept that highly fractal, multiscale coatings fabricated via electrodeposition can significantly improve the light trapping within the coatings, leading to improved solar absorptivity and figure of merit. For considered copper based coatings, significant improvement of figure of merit due to aggressive fractal texturing and heat treatment is observed. Maximum figure of merit value of nearly 42, for copper based coating deposited at 1.1 V and heat treated at 260° C for 1 hour in air is estimated. Measured thermal radiative properties for Pyromark Series 2500 are $\alpha_{solar} = 0.964$, $\varepsilon_{80°C} = 0.862$, and $\varepsilon_{2400nm} = 0.960$, which equates to a FOM of 53.3.[42] Chalhoub, et al. fabricated

cobalt oxide based solar selective coatings through chemical vapor deposition and demonstrated high absorptivity of coatings in the range of 250-1200 nm wavelength and coating fractal dimensions of 1.3-1.4.[109] This study indicates that significantly more fractal coatings can be prepared through scalable process such as electrodeposition and further improvement in solar absorptivity and figure of merit can be achieved. Presented results would inspire the application of similar inherent aggressive fractal solar selective coatings based on cobalt, cermets etc., which would be able to sustain the solar selectivity and figure of merit at operating temperatures in the range of 800-1000° C and will be considered in future studies. Additionally, the present work would also inspire further studies aimed at the estimation of required fractal parameters of a coating for specific surface optical properties.

6.3. Conclusions

An electrodeposition based process was employed to generate solar selective coatings inherently on a copper substrate. Prepared coatings exhibited stable, multiscale fractal morphologies and were described by a scale independent fractal description based on Weierstrass-Mandelbrot (W-M) function, where fractal parameters are uniquely determined by power spectrum of the surface. The effects of processing parameters on the coating fractal parameters and optical properties such as absorptance, emittance, and figure of merit were systematically studied and described. Furthermore, effects of heat treatment on optical properties were also quantified at various fractal levels and processing parameters. The coatings deposited at low overpotentials with fractal dimensions ranging from 1.5-1.65 did not demonstrate any significant variation in their optical properties. However, aggressive fractal texturing with fractal dimensions of nearly 1.8-1.9, for coatings deposited at high overpotentials beyond 0.9 V, showed significantly enhanced optical properties. The copper coatings with cauliflower-shaped multiscale fractal morphology, deposited at 1.1 V and heat treated at 260°C for 1 hour in air demonstrated the maximum figure of merit of 41.75. This study suggests that the fractal, multiscale coatings fabricated via electrodeposition significantly improve the light trapping within the coatings, leading to improved solar absorptivity and FOM.

Chapter 7. Conclusions and Future Work

This thesis described the generation and mathematical analysis of multiscale, randomly rough superhydrophobic and solar selective coatings through electrodeposition. Electrodeposition is one of the major technique to fabricate robust coatings in micro and nanoscale range. Deposition process, material and microstructure of coating are the primary factors affecting the functionality and durability of coatings. The thesis showed a representation of the multiscale coating morphology by a self-affine fractal model and description of wettability by use of this model. Furthermore, part of thesis work also described the electrodeposition based processes to generate robust superhydrophobic and solar selective coatings inherent on copper and zinc substrates.

The first part of thesis work considered analysis of wettability on randomly rough surfaces that were shown to exhibit self-affine fractal characteristics. The surfaces were described by an asperity network fractal model based on Weierstrass-Mandelbrot (W-M) function, where fractal parameters are uniquely determined by power spectrum of the surface. A model for predicting the apparent contact angle was developed based on the different wetting regimes. Experimental measurements on various hydrophobic and superhydrophobic surfaces fabricated using several materials and processing conditions were used to demonstrate the accuracy of the model predictions. In all the cases, the predictions were shown to be well within 5% of experimental measurements for different materials and fabricating processes. The model is unique in that it uses no empirical tuning factors and is shown to be applicable across different materials and fabrication processes. By use of the model, the fractal parameters required to generate superhydrophobicity on a particular substrate can be derived for any material and coating process. This, in turn, can be used to design processing conditions to achieve the desired surface properties on various substrate materials.

Next parts of thesis described the generation of superhydrophobic coatings inherent on copper and zinc substrates through electrodeposition. Copper and zinc based coatings exhibited stable, multiscale fractal, cauliflower shaped and branched-needle shaped morphology, respectively, which were further modified by an inexpensive stearic acid treatment to achieve superhydrophobicity. The effect of processing parameters on the morphology and wettability were described, and the coatings were shown to have a contact angles in the range of $156-164^{o}$ and roll-off angles of nearly 5^{o}. Systematic studies were performed to evaluate the chemical composition, growth mechanism, mechanical abrasion stability, corrosion resistance, self-cleaning effect, air-

exposure durability, under-water durability, and durability under flow conditions of the optimal superhydrophobic surfaces. Results for shear abrasion and falling sand abrasion tests were described based on frictional energy and sand impact energy per unit area, respectively. These representations combine the effects of the pertinent test parameters such as sandpaper grit size, abrasion distance, load, height of falling sand etc. and provide a unified way to compare the mechanical durability of superhydrophobic coatings measured under different conditions.

The superhydrophobic copper and zinc coatings showed excellent non-wetting characteristics under dynamic conditions, durability, mechanical and underwater stability, corrosion resistance and self-cleaning effect. Since the superhydrophobic coatings are generated inherently on the substrate material, unlike current practice of using a coating material that differs from the substrate material, the durability and longevity of the coatings are dramatically improved. When submerged in static or flowing water, it was observed that beyond a certain time, the contact angle decreases and the roll-off angle increases, due to loss of entrapped air to the surrounding water. The rate of loss of entrapped air was observed to be higher for a sample submerged in flowing water. These low-cost, facile processes can be used to develop large scale, durable superhydrophobic coatings with controllable wettability for a range of practical applications.

The last part of the thesis described the application of developed multiscale copper based coatings as solar selective coatings. Fractal parameters of coatings fabricated at a range of deposition potentials were correlated with their optical properties such as solar absorptivity, emissivity, and figure of merit. The coatings deposited at low overpotentials with fractal dimensions ranging from 1.5-1.65 did not demonstrate any significant variation in their optical properties. However, aggressive fractal texturing with fractal dimensions of nearly 1.8-1.9, for coatings deposited at high overpotentials beyond 0.9 V, showed significantly enhanced optical properties. The copper coatings with cauliflower-shaped multiscale fractal morphology, deposited at 1.1 V and heat treated at 260°C for 1 hour in air demonstrated the maximum figure of merit of 41.75. This study suggests and serves as a proof of study that the fractal, multiscale coatings fabricated via electrodeposition significantly improve the light trapping within the coatings, leading to improved solar absorptivity and figure of merit.

Future Work. The fractal description and model of surfaces presented in Chapter 3 can be extended to the estimation of dynamic behavior of droplet and contact angle hysteresis on such

surfaces, in a future study. The model can also be employed towards the wettability estimation of a deforming solid, following the work of Marchand, et al.[67] Moreover, as suggested in the recent studies by Mitra, et al.[68,69], surrounding viscous media may significantly affect the wetting behavior of any surface, governing equations as derived in the present study may be modified to accommodate such factors and will be considered as a future study. Moreover, excellent mechanical and immersion durability of the developed superhydrophobic coatings in Chapters 4,5 inspire the extension of similar fabrication technique into the development of durable superhydrophobic coatings on other materials and can be considered in future studies. Presented results in Chapter 6 would inspire the application of similar inherent aggressive fractal solar selective coatings based on cobalt, cermets etc., which would be able to sustain the solar selectivity and figure of merit at operating temperatures in the range of 800-1000° C and may be considered in future studies

Bibliograohy

1. Valipour M. N., Birjandi, F. C.; Sargolzaei, J. Super-Non-Wettable Surfaces: A Review. *Colloids Surfaces A Physicochem. Eng. Asp.* **2014**, *448* (1), 93–106.
2. Cuevas, A., Martínez, L., Romero, R., Dalchiele, E. A., Marotti, R., Leinen, D., Ramos-Barrado, J. R., Martin, F. Electrochemically Grown Cobalt-Alumina Composite Layer for Solar Thermal Selective Absorbers. *Sol. Energy Mater. Sol. Cells* **2014,** *130*, 380-386.
3. Kima, T. K., VanSaders, B., Moon, J., Kima, T., Liua, C. H., Khamwannaha, J., Chuna, D., Choia, D., Kargara, A., Chena, R., Liub, Z., Jin, S. Tandem Structured Spectrally Selective Coating Layer of Copper Oxide Nanowires Combined With Cobalt Oxide Nanoparticles. *Nano Energy* **2015**, *11*, 247-259.
4. Antonaia, A., Castaldo, A., Addonizio, M., Esposito, S. Stability of W-Al2O3 Cermet Based Solar Coating for Receiver Tube Operating at High Temperature. *Sol. Energy Mater. Sol. Cells* **2010,** *94*, 1604-1611.
5. Quéré, D. Non-Sticking Drops. *Reports Prog. Phys.* **2005**, *68*, 2495–2532.
6. Bhushan, B.; Jung, Y. C. Natural and Biomimetic Artificial Surfaces for Superhydrophobicity, Self-Cleaning, Low Adhesion, and Drag Reduction. *Prog. Mater. Sci.* **2011**, *56*, 1–108.
7. Wang, G.; Liu, S.; Wei, S.; Liu, Y.; Lian, J.; Jiang, Q.; Nishinaga, O.; Kikuchi, T.; Natsui, S.; Suzuki, R. O. Robust Superhydrophobic Surface on Al Substrate with Durability, Corrosion Resistance and Ice-Phobicity. *Nat. Publ. Gr.* **2016**, *3*, 4–5.
8. Wenzel, R. N. Resistance of solid surfaces to wetting by water. *Ind. Eng. Chem.* **1936**, *28*, 988–994.
9. Cassie, A. B. D.; Baxter, S. Wettability of porous surfaces. *Trans. Faraday Soc.* **1944**, *40*, 546–551.
10. Lafuma, A.; Quéré, D. Superhydrophobic States. *Nat. Mater.* **2003**, *2*, 457–460.
11. Liu, H. H.; Zhang, H. Y.; Li, W. Thermodynamic Analysis on Wetting Behavior of Hierarchical Structured Superhydrophobic Surfaces. *Langmuir* **2011**, *27* (10), 6260–6267.
12. Li, W.; Diao, Y. P.; Wang, S. Y.; Fang, G. P.; Wang, G. C.; Dong, X. J.; Long, S. C.; Qiao, G. J. New Roughness Parameter for the Characterization of Regularly Textured or Ordered Patterned Superhydrophobic Surfaces. *Langmuir* **2009**, *25* (11), 6076–6080.
13. Jeong, H. E.; Kwak, M. K.; Park, C. I.; Suh, K. Y. Wettability of Nanoengineered Dual-Roughness Surfaces Fabricated by UV-Assisted Capillary Force Lithography. *J. Colloid Interface Sci.* **2009**, *339* (1), 202–207.
14. Jin, M.; Feng, X.; Xi, J.; Zhai, J.; Cho, K.; Feng, L.; Jiang, L., Super-Hydrophobic PDMS Surface with Ultra-Low Adhesive Force. *Macromolecular Rapid Communications* **2005,** *26* (22), 1805-1809.
15. Huang, L.; Lau, S. P.; Yang, H. Y.; Leong, E. S. P.; Yu, S. F. Stable Superhydrophobic Surface via Carbon Nanotubes Coated with a ZnO Thin Film. *J. Phys. Chem. B* **2005**, *109*, 7746-7748.
16. Majumdar, A.; Bhushan, B. Fractal Model of Elastic-Plastic Contact between Rough Surfaces. *J. Tribol. ASME* **1991**, *113* (1), 1–11.
17. Fürstner, R.; Barthlott, W.; Neinhuis, C.; Walzel, P. Wetting and Self-Cleaning Properties of Artificial Superhydrophobic Surfaces. Langmuir 2005, 21, 956–961.
18. Wisdom, K. M.; Watson, J. a; Qu, X.; Liu, F.; Watson, G. S.; Chen, C.-H.; Wan, Y.; Lian, Z.; Liu, Z.; Yu, H.; et al. Self-Cleaning of Superhydrophobic Surfaces by Self-Propelled Jumping Condensate. Proc. Natl. Acad. Sci. U. S. A. 2013, 116, 7992–7997.
19. Ou, J.; Perot, B.; Rothstein, J. P. Laminar Drag Reduction in Microchannels Using Ultrahydrophobic Surfaces. Phys. Fluids 2004, 16, 4635–4643.

20. Choi, C. H.; Kim, C. J. Large Slip of Aqueous Liquid Flow over a Nanoengineered Superhydrophobic Surface. Phys. Rev. Lett. 2006, 96, 1–4.
21. Boreyko, J. B.; Chen, C. H. Self-Propelled Dropwise Condensate on Superhydrophobic Surfaces. Phys. Rev. Lett. 2009, 103, 2–5.
22. Miljkovic, N.; Preston, D. J.; Enright, R.; Wang, E. N. Electric-Field-Enhanced Condensation on Superhydrophobic Nanostructured Surfaces. ACS Nano 2013, 7, 11043–11054.
23. Cao, L.; Jones, A. K.; Sikka, V. K.; Wu, J.; Gao, D. Anti-Icing Superhydrophobic Coatings. Langmuir 2009, 25, 12444–12448.
24. Zhao, L.; Liu, Q.; Gao, R.; Wang, J.; Yang, W.; Liu, L. One-Step Method for the Fabrication of Superhydrophobic Surface on Magnesium Alloy and Its Corrosion Protection, Antifouling Performance. *Corros. Sci.* **2014**, *80*, 177–183.
25. Su, F.; Yao, K. Facile Fabrication of Superhydrophobic Surface with Excellent Mechanical Abrasion and Corrosion Resistance on Copper Substrate by a Novel Method. *ACS Appl. Mater. Interfaces* **2014**, *6*, 8762–8770.
26. Liu, Q.; Chen, D.; Kang, Z. One-Step Electrodeposition Process to Fabricate Corrosion-Resistant Superhydrophobic Surface on Magnesium Alloy. *ACS Appl. Mater. Interfaces* **2015**, *7*, 1859–1867.
27. Zhang, B.; Zhao, X.; Li, Y.; Hou, B. Fabrication of Durable Anticorrosion Superhydrophobic Surfaces on Aluminum Substrates via a Facile One-Step Electrodeposition Approach. *RSC Adv.* **2016**, *6*, 35455–35465.
28. Zhang, H.; Yang, J.; Chen, B.; Liu, C.; Zhang, M.; Li, C. Fabrication of Superhydrophobic Textured Steel Surface for Anti-Corrosion and Tribological Properties. *Appl. Surf. Sci.* **2015**, *359*, 905–910.
29. She, Z.; Li, Q.; Wang, Z.; Li, L.; Chen, F.; Zhou, J. Researching the Fabrication of Anticorrosion Superhydrophobic Surface on Magnesium Alloy and Its Mechanical Stability and Durability. *Chem. Eng. J.* **2013**, *228*, 415–424.
30. Chu, Q.; Liang, J.; Hao, J. Facile Fabrication of a Robust Super-Hydrophobic Surface on Magnesium Alloy. *Colloids Surfaces A Physicochem. Eng. Asp.* **2014**, *443*, 118–122.
31. Lv, D.; Ou, J.; Hu, W.; Luo, X.; Wang, F. Superhydrophobic Surface on Copper via a One-Step Solvent-Free Process and Its Application in Oil Spill Collection. *RSC Adv.* **2015**, *5*, 49459–49465.
32. A. C. Tolcin, U.S. Geological Survey, Mineral Commodity Summaries, 2016 (Accessed May 2017)
33. National Emission Standards for Hazardous Air Pollutant Emissions: Hard and Decorative Chromium Electroplating and Chromium Anodizing Tanks; and Steel Pickling—HCl Process Facilities and Hydrochloric Acid Regeneration Plants; Final Rules, Federal Register / Vol. 77, No. 182 / Wednesday, September 19, 2012 / Rules and Regulations, 58220-58253 (Accessed May 2017)
34. L. Feng, L. Zhao, X. Qiang, Y. Liu, Z. Sun, B. Wang, Fabrication of superhydrophobic copper surface with excellent corrosion resistance, Appl. Phys. A Mater. Sci. Process. 119 (2015) 75–83.
35. Haghdoost, A.; Pitchumani, R. Fabricating Superhydrophobic Surfaces via a Two-Step Electrodeposition Technique. *Langmuir* **2014**, *30* (14), 4183–4191.
36. Schneider, C.A.; Rasband, W.S.; Eliceiri, K.W. NIH Image to ImageJ: 25 years of image analysis. *Nature Methods* **2012,** *9*, 671-675.
37. Stalder, A. F.; Melchior, T.; Muller, M.; Sage, D.; Blu, T.; Unser, M. Low-bond axisymmetric drop shape analysis for surface tension and contact angle measurements of sessile drops. Colloids and Surfaces a-Physicochemical and Engineering Aspects 2010, 364, (1-3), 72-81.
38. Nečas, D.; Klapetek, P. Gwyddion: an Open-Source Software for SPM Data Analysis. *Cent. Eur. J. Phys.* **2012**, *10* (1), 181-188, *http://gwyddion.net*, Last accessed: April 2017.

39. ASTM. ASTM D968-15: Standard Test Methods for Abrasion Resistance of Organic Coatings by Falling Abrasive, *ASTM Int.* **2010**, 5 p.
40. Xu, W.; Song, J.; Sun, J.; Lu, Y.; Yu, Z. Rapid Fabrication of Large-Area, Corrosion-Resistant Superhydrophobic Mg Alloy Surfaces. *ACS Appl. Mater. Interfaces* **2011**, *3*, 4404–4414.
41. Verho, T.; Bower, C.; Andrew, P.; Franssila, S.; Ikkala, O.; Ras, R. H. A. Mechanically Durable Superhydrophobic Surfaces. *Adv. Mater.* **2011**, *23*, 673–678.
42. A. Ambrosini, C.K. Ho, A. Hall, Solar Selective Coatings for Concentrating Solar Power Central Receivers, Adv. Mater. Processes 170 (2012) 28-32.
43. G. Katumba, G. Makiwa, T.R. Baisitse, L. Olumekor, A. Forbes, E. Wäckelgård, Solar selective absorber functionality of carbon nanoparticles embedded in SiO2, ZnO and NiO matrices, Phys. Status Solidi Curr. Top. Solid State Phys. 5 (2008) 549–551.
44. G. Katumba, L. Olumekor, A. Forbes, G. Makiwa, B. Mwakikunga, J. Lu, E. Wackelgard, Optical, thermal and structural characteristics of carbon nanoparticles embedded in ZnO and NiO as selective solar absorbers, Sol. Energy Mater. Sol. Cells. 92 (2008) 1285–1292.
45. Barthlott, W.; Neinhuis, C. Purity of the Sacred Lotus, or Escape from Contamination in Biological Surfaces. *Planta* **1997**, *202* (1), 1–8.
46. Gao, X.; Jiang, L. Water-Repellent Legs of Water Striders. *Nature* **2004**, *432*, 36.
47. Hu, D. L.; Chan, B.; Bush, J. W. M. The Hydrodynamics of Water Strider Locomotion. *Nature* **2003**, *424*, 663–666.
48. Zhang J.; Seeger S. Silica/Silicone Nanofilament Hybrid Coatings with Almost Perfect Superhydrophobicity. *ChemPhysChem* **2013**, *14*, 1646-1651.
49. Awada, H.; Grignard, B.; Jerome, C.; Vaillant, A.; Coninck, J. D.; Nysten, B.; Jonas, A. M. Correlation between Superhydrophobicity and the Power Spectral Density of Randomly Rough Surfaces. *Langmuir* **2010**, *26* (23), 17798–17803.
50. Frankiewicz, C.; Attinger, D. Texture and Wettability of Metallic Lotus Leaves. *Nanoscale* **2015**, *8*, 3982–3990.
51. Majumdar, A.; Bhushan, B. Role of Fractal Geometry in Roughness Characterization and Contact Mechanics of Surfaces. *J. Tribol.* **1990**, *112*, 205.
52. Shibuichi, S.; Onda, T.; Satoh, N.; Tsujii, K. Super Water-Repellent Surfaces Resulting from Fractal Structure. *J. Phys. Chem.* **1996**, *100* (50), 19512–19517.
53. Onda, T.; Shibuichi, S.; Satoh, N.; Tsujii, K. Super-Water-Repellent Fractal Surfaces. *Langmuir* **1996**, *12* (9), 2125–2127.
54. Synytska, A.; Ionov, L.; Grundke, K.; Stamm, M. Wetting on Fractal Superhydrophobic Surfaces from "Core-Shell" Particles: A Comparison of Theory and Experiment. *Langmuir* **2009**, *22* (19), 3132–3136.
55. Palasantzas, G.; De Hosson, J. T. M. Wetting on Rough Surfaces. *Acta Mater.* **2001**, *49* (17), 3533–3538.
56. Bottiglione, F.; Carbone, G.; Persson, B. N. J. Fluid Contact Angle on Solid Surfaces: Role of Multiscale Surface Roughness. *J. Chem. Phys.* **2015**, *143* (13), 1–6.
57. Bottiglione, F.; Carbone, G. An Effective Medium Approach to Predict the Apparent Contact Angle of Drops on Super-Hydrophobic Randomly Rough Surfaces. *J. Phys. Condens. Matter* **2015**, *27* (1), 15009.
58. Yang, C.; Tartaglino, U.; Persson, B. N. J. Influence of Surface Roughness on Superhydrophobicity. *Phys. Rev. Lett.* **2006**, *97* (11), 1–4.

59. Sarkar, S.; Patra, S.; Gayathri, N.; Banerjee, S. Effect of Self-Affine Fractal Characteristics of Surfaces on Wetting. *Appl. Phys. Lett.* **2010**, *96* (6), 1–4.
60. David, R.; Neumann, A. W. Computation of the Wetting Properties of Randomly Structured Superhydrophobic Surfaces. *J. Phys. Chem. C* **2012**, *116* (31), 16601–16608.
61. Li, W.; Amirfazli, A. Hierarchical Structures for Natural Superhydrophobic Surfaces. **2008**, 462–466.
62. Li, W.; Amirfazli, A. Microtextured Superhydrophobic Surfaces: A Thermodynamic Analysis. **2007**, *132*, 51–68.
63. Li, W.; Amirfazli, A. A Thermodynamic Approach for Determining the Contact Angle Hysteresis for Superhydrophobic Surfaces. **2005**, *292*, 195–201.
64. Cortese, B.; D'Amone, S.; Manca, M.; Viola, I.; Cingolani, R.; Gigli, G. Superhydrophobicity due to the Hierarchical Scale Roughness of PDMS Surfaces. *Langmuir* **2008**, *24*, 2712–2718.
65. Yang, F.; Pitchumani, R. Interlaminar Contact Development during Thermoplastic Fusion Bonding. *Polym. Eng. Sci.* **2002**, *42* (2), 424–438.
66. Majumdar, A.; Tien, C. L. Fractal Characterization and Simulation of Rough Surfaces. *Wear* **1990**, *136*, 313–327.
67. Marchand, A.; Das, S.; Snoeijer, J. H.; Andreotti, B. Capillary Pressure and Contact Line Force on a Soft Solid. *Phys. Rev. Lett.* **2012**, *108*, 094301.
68. Mitra, S.; Mitra, S. K. Understanding the Early Regime of Drop Spreading. *Langmuir* **2016**, *32*, 8843-8848.
69. Mitra, S.; Gunda, N. S. K.; Mitra, S. K. Wetting Characteristics of Underwater Micro-patterned Surfaces. *RSC Adv.* **2017**, *7*, 9064-9072.
70. Xiang, Y.; Xue, Y.; Lv, P.; Li, D.; Duan, H. Influence of Fluid Flow on Stability and Wetting Transition of Submerged Superhydrophobic Surfaces. *Soft Matter* **2016**, *12*, 4241–4246.
71. Bobji, M. S.; Kumar, S. V.; Asthana, A.; Govardhan, R. N. Underwater Sustainability of the "Cassie" state of Wetting. *Langmuir* **2009**, *25*, 12120–12126.
72. Samaha, M. A.; Tafreshi, H. V.; Gad-El-Hak, M. Influence of Flow on Longevity of Superhydrophobic Coatings. *Langmuir* **2012**, *28*, 9759–9766.
73. Fan, Y.; He, Y.; Luo, P.; Chen, X.; Liu, B. A Facile Electrodeposition Process to Fabricate Corrosion-Resistant Superhydrophobic Surface on Carbon Steel. *Appl. Surf. Sci.* **2016**, *368*, 435–442.
74. Feng, L.; Zhao, L.; Qiang, X.; Liu, Y.; Sun, Z.; Wang, B. Fabrication of Superhydrophobic Copper Surface with Excellent Corrosion Resistance. *Appl. Phys. A Mater. Sci. Process.* **2015**, *119*, 75–83.
75. Ozkan, E.; Crick, C. C.; Taylor, A.; Allan, E.; Parkin, I. P. Copper-Based Water Repellent and Antibacterial Coatings by Aerosol Assisted Chemical Vapour Deposition. *Chem. Sci.* **2016**, *0*, 1–6.
76. Li, P.; Chen, X.; Yang, G.; Yu, L.; Zhang, P. Preparation of Silver-Cuprous Oxide/stearic Acid Composite Coating with Superhydrophobicity on Copper Substrate and Evaluation of Its Friction-Reducing and Anticorrosion Abilities. *Appl. Surf. Sci.* **2014**, *289*, 21–26.
77. Li, J.; Wan, H.; Ye, Y.; Zhou, H.; Chen, J. One-Step Process for the Fabrication of Superhydrophobic Surfaces with Easy Repairability. *Appl. Surf. Sci.* **2012**, *258*, 3115–3118.
78. Liu, T.; Yin, Y.; Chen, S.; Chang, X.; Cheng, S. Super-Hydrophobic Surfaces Improve Corrosion Resistance of Copper in Seawater. *Electrochim. Acta* **2007**, *52*, 3709–3713.
79. Li, G.; Wang, B.; Liu, Y.; Tan, T.; Song, X.; Li, E.; Yan, H. Stable Superhydrophobic Surface: Fabrication of Interstitial Cottonlike Structure of Copper Nanocrystals by Magnetron Sputtering. *Sci. Technol. Adv. Mater.* **2008**, *9*, 25006.

80. Huang, Y.; Sarkar, D. K.; Gallant, D.; Chen, X. G. Corrosion Resistance Properties of Superhydrophobic Copper Surfaces Fabricated by One-Step Electrochemical Modification Process. *Appl. Surf. Sci.* **2013**, *282*, 689–694.
81. Shirtcliffe, N. J.; McHale, G.; Newton, M. I.; Perry, C. C. Wetting and Wetting Transitions on Copper-Based Super-Hydrophobic Surfaces. *Langmuir* **2005**, *21*, 937–943.
82. Wang, L.; Guo, S.; Dong, S. Facile Electrochemical Route to Directly Fabricate Hierarchical Spherical Cupreous Microstructures: Toward Superhydrophobic Surface. *Electrochem. commun.* **2008**, *10*, 655–658.
83. Wang, P.; Zhang, D.; Qiu, R.; Wu, J. Super-Hydrophobic Metal-Complex Film Fabricated Electrochemically on Copper as a Barrier to Corrosive Medium. *Corros. Sci.* **2014**, *83*, 317–326.
84. Wang, Z.; Li, Q.; She, Z.; Chen, F.; Li, L. Low-Cost and Large-Scale Fabrication Method for an Environmentally-Friendly Superhydrophobic Coating on Magnesium Alloy. *J. Mater. Chem.* **2012**, *22*, 4097.
85. Darmanin, T.; De Givenchy, E. T.; Amigoni, S.; Guittard, F. Superhydrophobic Surfaces by Electrochemical Processes. *Adv. Mater.* **2013**, *25*, 1378–1394.
86. Zuo, Z.; Liao, R.; Guo, C.; Yuan, Y.; Zhao, X.; Zhuang, A.; Zhang, Y. Fabrication and Anti-Icing Property of Coral-like Superhydrophobic Aluminum Surface. *Appl. Surf. Sci.* **2015**, *331*, 132–139.
87. Xu, L.; Geng, Z.; He, J.; Zhou, G. Mechanically Robust, Thermally Stable, Broadband Antire Fl Ective, and Superhydrophobic Thin Films on Glass Substrates. *ACS Appl. Mater. Interfaces* **2014**, *6*, 9029–9035.
88. ASTM. ASTM D 4060-10: Standard Test Method for Abrasion Resistance of Organic Coatings by the Taber. *ASTM Int.* **2010**, 5 p.
89. ASTM. ASTM D870-15: Standard practice for testing water resistance of coatings using water immersion. *ASTM Int.* **2015**, 3 p.
90. H. Liu, L. Feng, J. Zhai, L. Jiang, D. Zhu, Reversible wettability of a chemical vapor deposition prepared ZnO film between superhydrophobicity and superhydrophilicity, Langmuir. 20 (2004) 5659–5661.
91. H. Liu, S. Szunerits, M. Pisarek, W. Xu, R. Boukherroub, Preparation of Superhydrophobic Coatings on Zinc, Silicon, and Steel by a Solution-Immersion Technique, ACS Appl. Mater. Interfaces. 1 (2009) 2086–2091.
92. B. Qian, Z. Shen, Fabrication of superhydrophobic surfaces by dislocation-selective chemical etching on aluminum, copper, and zinc substrates, Langmuir. 21 (2005) 9007–9009.
93. C.-W. Hsu, T.-C. Cheng, W.-H. Huang, J.-S. Wu, C.-C. Cheng, K.-W. Cheng, S.-C. Huang, Relation between the plasma characteristics and physical properties of functional zinc oxide thin film prepared by radio frequency magnetron sputtering process, Thin Solid Films. 518 (2010) 1953–1957.
94. K.Y. Kok, I.K. Ng, N.U. Saidin, F.K.A. Bustamam, Fabrication of ZnO Nanostructures with Self-Cleaning Functionality, Adv. Mater. Res. 364 (2011) 100–104.
95. B. Zhang, S. Lu, W. Xu, Y. Cheng, Controllable wettability and morphology of electrodeposited surfaces on zinc substrates, Appl. Surf. Sci. 360 (2016) 904–914.
96. X. Zhang, J. Liang, B. Liu, Z. Peng, Preparation of superhydrophobic zinc coating for corrosion protection, Colloids Surfaces A Physicochem. Eng. Asp. 454 (2014) 113–118.
97. SunShot, Energy Efficiency and Renewable Energy, U.S. Department of Energy, SunShot Vision Study: February 2012. NREL Report No. BK5200-47927, DOE/GO-102012-3037 (accessed May 2017).

98. R. Sioshansi, P. Denholm, The value of concentrating solar power and thermal energy storage, IEEE Trans. Sustain. Energy 1 (2010) 173–183.
99. Z. Y. Nuru, D. E. Motaung, K. Kaviyarasu, M. Maaza, Optimization and preparation of Pt-Al2O3 double cermet as selective solar absorber coatings, J. Alloys Compd. 664 (2016) 161-168.
100. A. Karoro, Z.Y. Nuru, L. Kotsedi, K. Bouziane, B.M. Mothudi, M. Maaza, Laser nanostructured Co nanocylinders-Al2O3 cermets for enhanced & flexible solar selective absorbers applications, Appl. Surf. Sci. 347 (2015) 679–684.
101. X. Wang, H. Li, X. Yu, X. Shi, J. Liu, High-performance solution-processed plasmonic Ni nanochain-Al 2O3 selective solar thermal absorbers, Appl. Phys. Lett. 101 (2012) 1–6.
102. E. Barrera, F. Gonzalez, E. Rodriguez, J. Alvarez-Ramirez, Correlation of optical properties with the fractal microstructure of black molybdenum coatings, Appl. Surf. Sci. 256 (2010) 1756–1763.
103. M. Lazarov, A. Brunotte, T. Eisenhamrner, R. Sizmann, F. Ise, D.- Freiburg, Effects of Roughness on TiNO- Cu Selective Absorbers 1 Introduction 2 Theoretical Model, 1727 (1992) 34–45.
104. M. Farooq, Z.H. Lee, Computations of the optical properties of metal/insulator-composites for solar selective absorbers, Renew. Energy. 28 (2003) 1421–1431.
105. S. Pratesi, M. De Lucia, M. Meucci, E. Sani, Structural and optical properties of copper-coated substrates for solar thermal absorbers, Superlattices Microstruct. 98 (2016) 342–350.
106. R. Axelbaum, H. Brandt, The effect of substrate surface preparation on the optical properties of a black chrome solar absorber coating, Solar Energy 39 (1987) 233-241.
107. P. Kowalczewski, M. Liscidini, L.C. Andreani, Engineering Gaussian disorder at rough interfaces for light trapping in thin-film solar cells., Opt. Lett. 37 (2012) 4868–70.
108. M.C. Kang, J.S. Kim, K.H. Kim, Fractal dimension analysis of machined surface depending on coated tool wear, Surf. Coatings Technol. 193 (2005) 259–265.
109. E. Amin-Chalhoub, T. Duguet, D. Samélor, O. Debieu, E. Ungureanu, C. Vahlas, Chemical vapor deposition of low reflective cobalt (II) oxide films, Appl. Surf. Sci. 360 (2016).